# Remotely Sensed Based Hydrological Model Calibration for Basin Scale Water Resources Planning

***Embedding case for Krishna Basin, India***

NIVR
Nederlands Instituut voor Vliegtuigontwikkeling en Ruimtevaart
Netherlands Agency for Aerospace Programmes

***Final project report***
***Project no. 53611FW***
***February 2007***

IWMI International Water Management

Future Water Science for Solutions

P.O. Box 35
2600 AA Delft
The Netherlands
Kluyverweg 1
2629 HS Delft
The Netherlands
Tel. +31 (0)15 278 80 25
Fax +31 (0)15 262 30 96
Email info@nivr.nl
www.nivr.nl

# NATIONAL USER SUPPORT PROGRAMME (NUSP) 2001-2005

**http://www.ao-go.nivr.nl**

The National User Support Programme 2001-2005 (NUSP) is executed by the Netherlands Agency for Aerospace Programmes (NIVR) and the Space Research Organization of the Netherlands (SRON). The NUSP is financed from the national space budget. The NUSP subsidy arrangement contributes to the development of new applications and policy-supporting research, institutional use and use by private companies.

The objectives of the NUSP are:

- To support those in the Netherlands, who are users of information from existing and future European and non-European earth observation systems in the development of new applications for scientific research, industrial and policy research and operational use;

- To stimulate the (inter)national service market based on space-based derived operational geo-information products by means of strengthening the position of the Dutch private service sector;

- To assist in the development of a national Geo-spatial data and information infrastructure, in association with European and non-European infrastructures, based on Dutch user needs;

- To supply information to the general public on national and international space-based geo-information applications, new developments and scientific research results.

**Lead agency:**

FutureWater
Costerweg 1G
6702 AA Wageningen
The Netherlands
Tel: +31 (0)317 460050
http://www.futurewater.nl
info@futurewater.nl

**Partner organization:**

International Water Management Institute (IWMI)
c/o ICRISAT Patancheru
AP 502 324
India
Tel: +91 (0)40 30713733
http://www.iwmi.org

**Project website:**

http://www.futurewater.nl/krishna

**Authors:** W.W. Immerzeel (FutureWater)
P. Droogers (FutureWater)
A. Gaur (IWMI)

# Table of Contents

# 1 Abstract

The challenge to manage our water resources in a sustainable and appropriate manner is growing. Water related disasters are not accepted anymore and societies expect more and more that water is always available at the right moment and at the desired quantity and quality. There is a great demand for objective information and tools that can assist water managers and the use of Remote Sensing in water management has increased over the years. The combination of remote sensing with a decision support system (DSS) provides the unique opportunity to evaluate future changes using objective spatial information. This project has embedded an innovative methodology that uses remotely sensed evapotranspiration in the calibration of a DSS. Traditionally these DSS are calibrated using measured stream flow data, whilst this project included time series of remotely sensed evapotranspiration in the calibration. This approach greatly enhanced the performance of the DSS and, more importantly, enabled the application in data scarce and drought prone areas. The project provided a rigorous evaluation of different DSS and remote sensing methods for evapotranspiration mapping, and the optimal combination was applied to the drought prone Krishna basin in India. It is expected that the methodology can be applied in similar areas across the globe.

# 2 Executive summary

The challenge to manage our water resources in a sustainable and appropriate manner is growing. Water related disasters are not accepted anymore and societies expect more and more that water is always available at the right moment and at the desired quantity and quality. However, the number of major water related disasters as droughts and floods is on the rise, as well as the number of people affected, total loss in lives, and economic damage.

Over the last decade, various tools based on Remote Sensing (RS) techniques from satellites to assist water managers have been developed. One of the key aspects in this is the development of methodologies to estimate actual evapotranspiration from land surfaces using a combination of sensors of different temporal and spatial scales. However, one of the characteristics of RS is that, despite the excellent opportunities for monitoring, it offers fewer opportunities in itself to perform the so much required tool for long-term strategic planning of water resources.

Strategic Decision Support Systems have a hydrological focus, describing the entire water cycle including natural as well as human induced processes. These S-DSS are extremely powerful in evaluating the impact of changes in water management such as reservoir building, changes in water allocation between and within sectors, and impact of climate change.

Despite substantial progress in the development of these S-DSS techniques, the weakest part is currently the lack of data to apply and calibrate these S-DSSs. Traditionally, these S-DSSs are fine-tuned by a calibration process where observed hydrographs are compared to simulated ones. By adjusting the most sensitive and most unreliable input parameters the S-DSSs can be calibrated and performs better in describing the current situation and is therefore also more reliable to explore water management options for the future. This is the standard practice for almost every hydrological modelling study. It is clear that in data scarce areas such an approach, which requires observed stream flow data, is impossible and analyses are therefore often based on non-calibrated models, resulting in erroneous output.

The linkage between the previous mentioned RS techniques and S-DSS models is that simulation models provide also spatial information on evapotranspiration. This opens the unique opportunity to calibrate models using the observed evapotranspiration from RS. The importance of this should not be underestimated. The application of an S-DSS in data scarce areas was so-far nearly impossible as proper calibration could not be performed. Without such an S-DSS water managers were not able to systematically quantify the impact of proposed changes in water management.

The objective of this project was defined as:

*Embedding a methodology to support water managers in making sound and long term strategic decisions regarding water resources management by using Remotely Sensed based evapotranspiration estimates for calibration of Strategic Decision Support Systems.*

First a rigorous literature overview was performed of both remote sensing methods to estimate evapotranspiration as well as different DSS. Based on this overview and the study area, the Krishna basin in India, it was decided to select the surface energy balance (SEBAL) method to derive a time series of evapotranspiration using MODIS satellite imagery. These data were then used to calibrate the Soil and Water Assessment Tool (SWAT). Besides in calibration remote sensing was used to perform a

land use classification and in precipitation mapping using data from the tropical rainfall monitoring mission. The approach proved successful and increased the applicability and quality of the DSS. This has important consequences; it is now possible to reliably develop and use models in areas where this was previously not possible due to data scarcity. It is concluded that this methodology can be further applied in our international projects. The projected resulted in two peer reviewed papers in scientific journals, a report, a calibrated DSS and a time series of remotely sensed evapotranspiration. For more information reference is made to the project website:

http://www.futurewater.nl/krishna

# 3 Introduction

## 3.1 Relevance

The challenge to manage our water resources in a sustainable and appropriate manner is growing. Water related disasters are not accepted anymore and societies expect more and more that water is always available at the right moment and at the desired quantity and quality. However, the number of major water related disasters as droughts and floods is on the rise, as well as the number of people affected, total loss in lives, and economic damage (Figure 1).

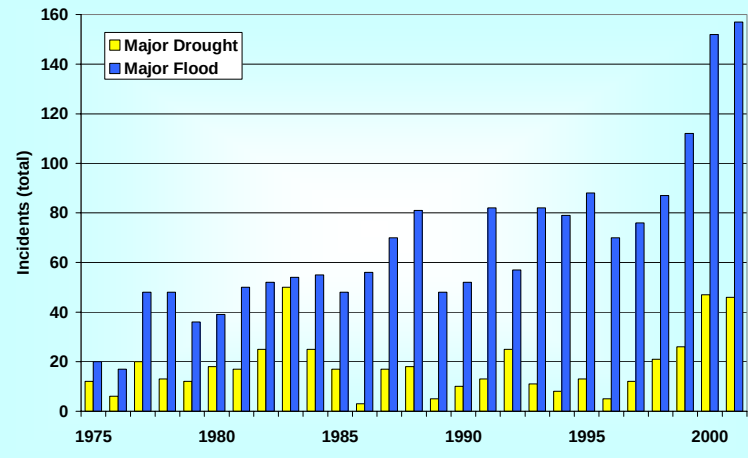


*Figure 1. Number of water related major disasters over the last 25 year. Source: Emergency Events Database: EM-DAT, 2002.*

Over the last decade, various tools based on Remote Sensing (RS) techniques from satellites to assist water managers have been developed. In the early days of RS, images were mainly used qualitative, but the increase in accuracy of sensors and especially a better understanding of processes, have evolved in the development of quantitative algorithms to convert raw data into useful information. One of the key aspects in this is the development of methodologies to estimate actual evapotranspiration from land surfaces using a combination of sensors of different temporal and spatial scales. However, one of the characteristics of RS is that, despite the excellent opportunities for monitoring, it offers fewer opportunities in itself to perform the so much required tool for long-term strategic planning of water resources.

From the RS tools available to water managers developed over the last years are the ones related to estimation of actual evapotranspiration the most relevant ones. A typical example is the Surface Energy Balance Algorithm of Land (SEBAL; Bastiaanssen et al., 1998). SEBAL has evolved into the world leading algorithm for estimating actual evapotranspiration by Remote Sensing and has been applied worldwide. However, its application is much more as a monitoring tool rather than a long-term planning tool.

It is becoming more and more evident that proper water management does not rely only on this day-to-day management, but more and more on strategic planning. A key issue in this strategic planning of water resources is the ability to have proper planning and management tools available. These tools can be divided in Operational and more Strategic Decision Support Systems: O-DSS and S-DSS, both relying on simulation models that can mimic reality. The O-DSS are mainly hydraulic oriented models able to predict on a time scale from hours to days in high detail how water will flow in river and canal systems, relying on accurate flow measurements upstream to predict timing and quantity of water downstream. These systems have been very effective in reducing the number of fatalities by so-called early-warning systems, but are not very helpful in a more strategic planning of water resources management.

The Strategic Decision Support Systems (S-DSS) have a much more hydrological focus, describing the entire water cycle including natural as well as human induced processes. The objective of these tools is not to predict as accurate as possible the time a flood or drought might occur, but the probability of exceedance of these events and what long-term options might be feasible to reduce these risks. Besides this capability to estimate these extremes, these S-DSS are extremely powerful in evaluating the impact of changes in water management such as reservoir building, changes in water allocation between and within sectors, and impact of climate change.

Despite substantial progress in the development of these S-DSS techniques, the weakest part is currently the lack of data to apply and calibrate these S-DSSs. Traditionally, these S-DSSs are fine-tuned by a calibration process where observed hydrographs are compared to simulated ones. By adjusting the most sensitive and most unreliable input parameters the S-DSSs can be calibrated and performs better in describing the current situation and is therefore also more reliable to explore water management options for the future. It must be emphasized here that this is the standard practice for almost every hydrological modelling study. It is clear that in data scarce areas such an approach, which requires observed stream flow data, is impossible and analyses are therefore often based on non-calibrated models, resulting in erroneous output.

The linkage between the previous mentioned RS techniques and S-DSS models is that simulation models provide also spatial information on evapotranspiration. This opens the unique opportunity to calibrate models using the observed evapotranspiration from RS. The importance of this should not be underestimated. The application of an S-DSS in data scarce areas was so-far nearly impossible as proper calibration could not be performed. Without such an S-DSS water managers were not able to systematically quantify the impact of proposed changes in water management.

The question arises why such an approach has not been applied earlier? One of the main reasons is that the techniques to estimate evapotranspiration from RS are relatively new. Developments started about 10 years back and only recently, methods are sufficiently tested and verified to be reliable enough for immediate application. A second reason is the communication gap between hydrologists applying simulation models and Remote Sensing scientists. Most importantly, however, is that reliable techniques related to linking models and Remote Sensing, calibration and algorithm development are lacking so far.

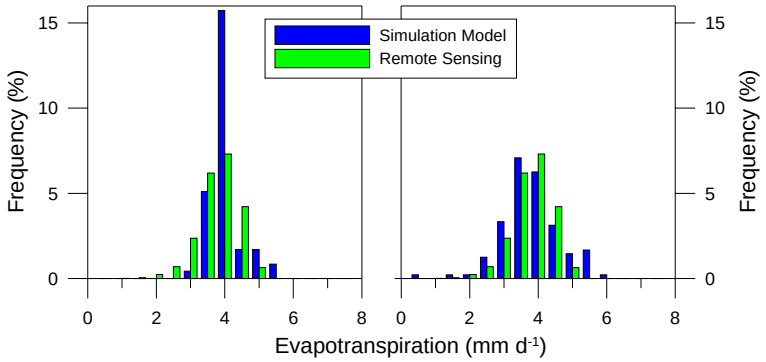


*Figure 2. Calibration of simulation model using evapotranspiration estimates. Example from an irrigated grape area in Turkey, with non-calibrated (left) and calibrated (right) (Droogers and Bastiaanssen, 2001).*

Some preliminary studies of this nature took place in Turkey (Droogers and Bastiaanssen, 2001) where no advanced calibration techniques were applied, but a simple manual adjustment was used. Some major aspects were ignored in that study. First of all, the focus was only on smaller areas, without including a full hydrological basin. Second, the selected areas were mainly in use by agriculture, ignoring important other land uses as forests, natural vegetations and urban areas. Third, analyses were performed using a one dimensional saturated-unsaturated model rather than a full hydrological one. A similar study in North-India showed that genetic algorithms can be used to estimate soil characteristics from RS evapotranspiration data (Ines and Droogers, 2002).

The following issues are addressed in this project:

- since the outflow out of a river basin is the net result of all hydrological processes and interactions the calibration of hydrological models on hydrographs provides a lot of freedom in the parameters to be calibrated. The calibration on evapotranspiration only is more restrictive because it focuses on a relatively secluded part of the hydrological cycle. It therefore requires a sophisticated calibration procedure;
- hydrograph calibration is based on only a few points, evapotranspiration calibration is based on thousands of pixels, which requires a completely different and more advanced calibration procedure;
- water stressed areas are likely to be calibrated easier than non-water stressed areas, but to what extent is unclear;
- the challenges new generations satellites/sensors such as Envisat/MERIS offer, are to be explored for this specific case to use RS information to calibrate S-DSS.

## 3.2 Objectives

Considering the points outlined in the previous sections the overall objective of the project was defined as:

*Embedding a methodology to support water managers in making sound and long term strategic decisions regarding water resources management by using Remotely Sensed based evapotranspiration estimates for calibration of Strategic Decision Support Systems.*

Such a methodology is of paramount importance to FutureWater to maintain and expand its applied research advisory services. The methodology was set up with the International Water Management Institute and applied in the Krishna basin in southern India.

## 3.3 Anticipated Results

The salient innovative aspect is that the approach to calibrate hydrological models is completely different from what has been done over the last 30 years. The approach to use measured streamflow (hydrographs) to calibrate these models have been applied since simulation models exist reasonable successfully. The weakest point has always been the lack of data, and especially reliable data, and has seriously hampered the application of these models for water management planning in data scarce areas such as India. The presented approach to use Remotely Sensed measured evapotranspiration is a completely different way of thinking.

The results of this research has generated:

- a methodological setup to calibrate S-DSS based on Remotely Sensed evapotranspiration estimated and an evaluation of the most suitable RS data;
- an advanced calibration procedure for the S-DSS to deal with RS evapotranspiration data;
- improved S-DSS based on RS evapotranspiration verification.

## 3.4 End product

The end product is an innovative use of RS evapotranspiration estimates to calibrate hydrological models used as S-DSS The defined criteria of the end product is to improve the accuracy of S-DSSs from 60-80% currently to at least 90%. This end product will be embedded in the Krishna Basin and expanded to other areas by project partners after successful completion of the project.

For FutureWater such an innovative product has enabled them to improve substantially their services in supporting clients in strategic decision making regarding water management. This enablesd FutureWater to enlarge its international advisory by integrating remotely sensed data with S-DSS. It is clear that such a product is in high demand by water managers all over the world, especially in regions where data are scarce.

For IWMI the product will directly be used to advice water managers in the basins where IWMI has activities in this field. Access to such a product will contribute to the fulfillment of its mission: improving water and land resources management for food livelihoods and nature.

## 3.5 Report outline

This final report starts with a theoretical overview of evapotranspiration and measurements techniques both with meteorological instruments and remote sensing in chapter 4. Chapter 5 provides an overview of hydrological modelling and the state of the art in calibration techniques and tools. In chapter 6 the application of the methodology in the Krishna basin will be described, while in chapter 7 a cost-benefit analysis is presented. The conclusion and outlook to the future is presented in the final chapter. The results of this project are reported as two scientific article, which are submitted to international peer reviewed journal: *hydrological processes* and *agricultural water management*. These papers are attached in the annex of the report.

The project results are also available at the project website:

http://www.futurewater.nl/krishna

# 4 Remote Sensing and evapotranspiration mapping

## 4.1 Introduction

Evapotranspiration is a collective term that includes water discharged to the atmosphere as a result of evaporation from the soil and surface-water bodies and as a result of plant transpiration. Evapotranspiration is an important component of the water cycle. Figure 3 shows an overview of the global water cycle. It shows that over land approximately 75% of the total precipitation is evapotranspired (70,000 $km^3$/year) by the plants and soil. Given a total land surface area of 148,940,000 $km^2$ this roughly equals 470 mm/year. Over the oceans this amount is even much higher (425,000 $km^3$). Evapotranspiration, also referred to as a latent heat flux when expressed as energy flux, is the most important mechanism of energy and mass exchange between the hydrosphere, biosphere and atmosphere. Evapotranspiration is a function of water and energy availability, near-surface atmospheric conditions (e.g. air temperature, relative humidity and wind-speed) and the control of transpiration by plants.

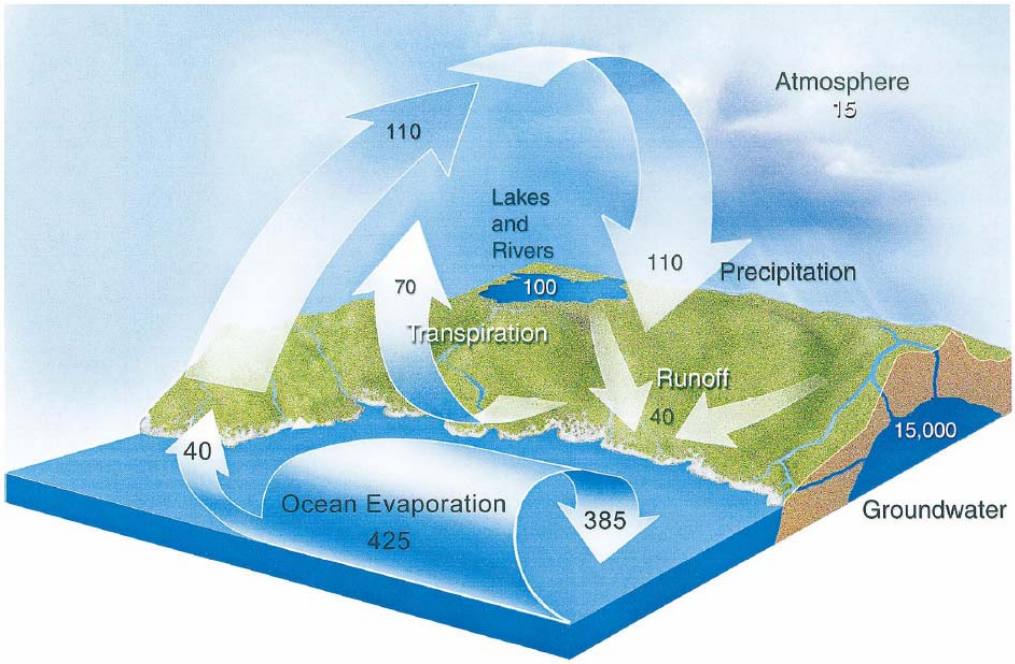


*Figure 3: Global hydrological cycle in 1000 $km^3$/year. Numbers in white are pools and numbers in black are fluxes (Jackson et al., 2001).*

Calculation of turbulent atmospheric fluxes is a complex task given the chaotic behaviour of turbulence and the many variables involved. Being able to accurately predict spatially explicit actual evapotranspiration across large heterogeneous landscapes is an even more daunting task for which Remote Sensing has proven to be the only appropriate instrument. In this report we first summarize the turbulence theory underlying most methods, and then we provide a brief overview of a number of

quantitative methods to measure evapotranspiration. First methods based on estimating evapotranspiration using field measurements are discussed followed by a more in-depth overview of Remote Sensing methods.

## 4.2 *Physical background of turbulent transport1*

### 4.2.1 Introduction

Atmospheric transport of water vapor close to the surface takes place mainly by diffusive processes, while further away the transport is dominated by turbulent transfer due to increasing wind speed and buoyancy effects. The theory of these physical transport processes was extensively described by, for example, Brutsaert (1982), Panofsky and Dutton (1984) and Garratt (1992). Although a complete account of the theoretical development is clearly beyond the scope of this chapter, a short outline is indispensable for an understanding of the parameterizations of current operational applications. Therefore a summary description is given of the atmospheric boundary layers and type of surfaces involved. This is followed by a discussion of the mean logarithmic wind profile, shear stress and friction velocity. The approach is then extended to include similar expressions for specific humidity and temperature: the so-called scalar quantities. The theory for $CO_2$ transport and radioactive deposition follows along the same lines, but is not further discussed here. It is necessary to discuss the roughness parameters for momentum, heat and water vapor transport in some detail because these appear in the Penman-Monteith formulation for reference crop evapotranspiration and because their determination forms a major bottleneck in the determination of land surface fluxes. Finally, the effects of stable and unstable atmospheric conditions are incorporated in the equations.

### 4.2.2 The Atmospheric Boundary Layer

In the atmosphere the largest changes in wind, temperature and humidity take place near the surface. For this reason the air near the surface may be regarded as a boundary layer for momentum, heat and mass transport. In this context one usually refers to the Atmospheric Boundary Layer, which is subdivided as follows (Figure 4)

[1] Text provided in this chapter is extracted from Gieske (2003)

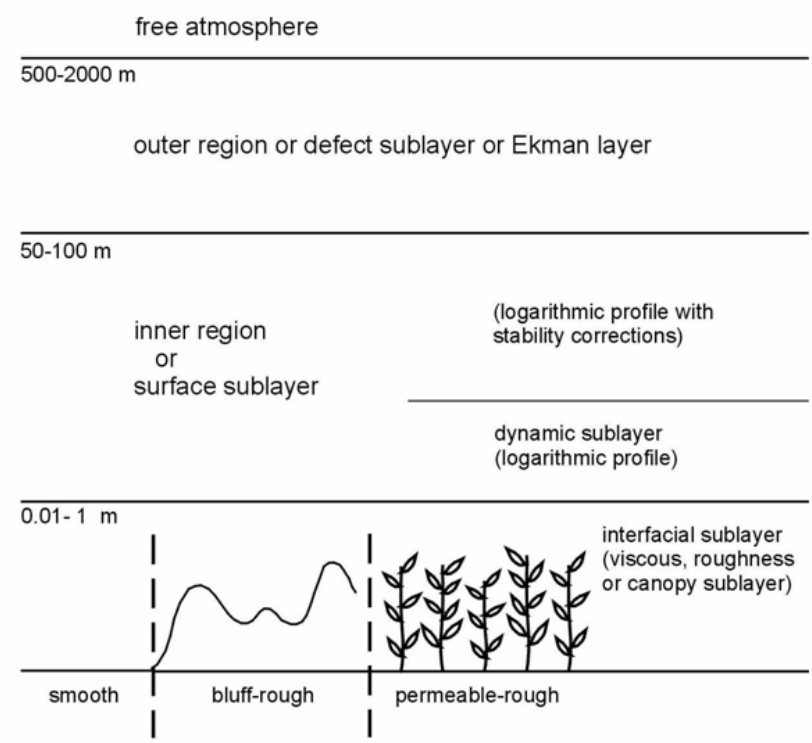


*Figure 4 Definition sketch showing simplified sublayers of the Atmospheric Boundary layer after Brutsaert (1982). The heights in m indicate the variable heights of the boundaries (not to scale)*

The flow in the "free" atmosphere above the boundary layer (ABL) is that of a free stream, affected mainly by the pressure field and Earth rotation, but very little by friction with the surface. The top of the Atmospheric Boundary Layer varies between 500 and 2000 m. However, this strongly depends on atmospheric conditions and on whether it is day or night. For example, over deserts under strong surface heating the thickness of the ABL may be 5km or more. Over open oceans the ABL thickness is usually less than over land. The top of the ABL is in convective conditions often well defined by a stable inversion layer.

The ABL is subdivided into an inner and outer region. The transition between inner and outer region is gradual rather than abrupt. The outer region is also called defect sublayer or Ekman layer while the flow in this region is nearly independent of the surface characteristics and largely determined by the free stream velocity. The flow in the inner region or surface sublayer is characterized by the nature of the Earth's surface. The lower part of the inner region is called the dynamic sublayer.

Finally below the dynamic sublayer and directly above the surface lies the interfacial sublayer, where the turbulence is strongly affected by the roughness of the surface elements. In this layer molecular diffusivities can no longer be neglected in the description of water vapour and heat transport mechanisms. In the case of smooth flow this layer is often called the viscous sublayer, while over a rough surface it may be referred to as roughness sublayer (Brutsaert, 1982). Finally over vegetation many complications arise depending on foliage density and canopy depth, and in this case the layer is often called canopy sublayer.

### 4.2.3 Logarithmic wind profile

When the wind blows across a surface, it is observed that the wind speed is a function of the height above the surface. The wind speed is zero at the surface because of frictional effects of the air with the surface and increases steadily with increasing height. Thus the air momentum becomes less with decreasing height. The downward transport of momentum is caused mainly by turbulent eddies, and the effectiveness of this transport mechanism is described by the friction velocity $u_*$ ($ms^{-1}$) which by definition (Brutsaert, 1982) is related to shear stress $\tau_0$ ($N\ m^{-2}$) as

$$u_* = \sqrt{\frac{\tau_0}{\rho}} \qquad \textit{Eq. 1}$$

Where $\rho$ is the average air density ($kg\ m^{-3}$). The shear stress $\tau_0$ is generally taken as constant for the inner region of the ABL. It appears that this is a sufficiently accurate assumption for heights of up to 100 m above the surface.

The nature of the wind speed change with elevation has been investigated extensively since the 1920s and was first introduced in meteorology by Prandtl (1932). The results are usually written as

$$\frac{u_*}{z\left(d\bar{u}/dz\right)} = k \qquad \textit{Eq. 2}$$

Where $\bar{u}$ is the average wind speed ($m\ s^{-1}$) and z is the elevation above the surface (m). Experimentally it was found that the left hand side Eq. 2 is constant k, which is referred to as von Kárman's constant and is usually taken as 0.41. The logarithmic wind profile equation follows immediately from integration of Eq. 2.

$$\bar{u}_2 - \bar{u}_1 = \frac{u_*}{k}\ln\left(\frac{z_2}{z_1}\right) \qquad \textit{Eq. 3}$$

where the subscripts refer to two levels in the dynamic sublayer. The level at which $u_1$ becomes zero is called the momentum roughness length $z_{om}$ (m) and Eq. 3 is then written as

$$\bar{u} = \frac{u_*}{k}\ln\left(\frac{z}{z_{om}}\right) \qquad \textit{Eq. 4}$$

The momentum roughness length may be visualized graphically as the zero velocity intercept of the straight line resulting from a semi-logarithmic plot of mean wind speed versus elevation (Figure 5).

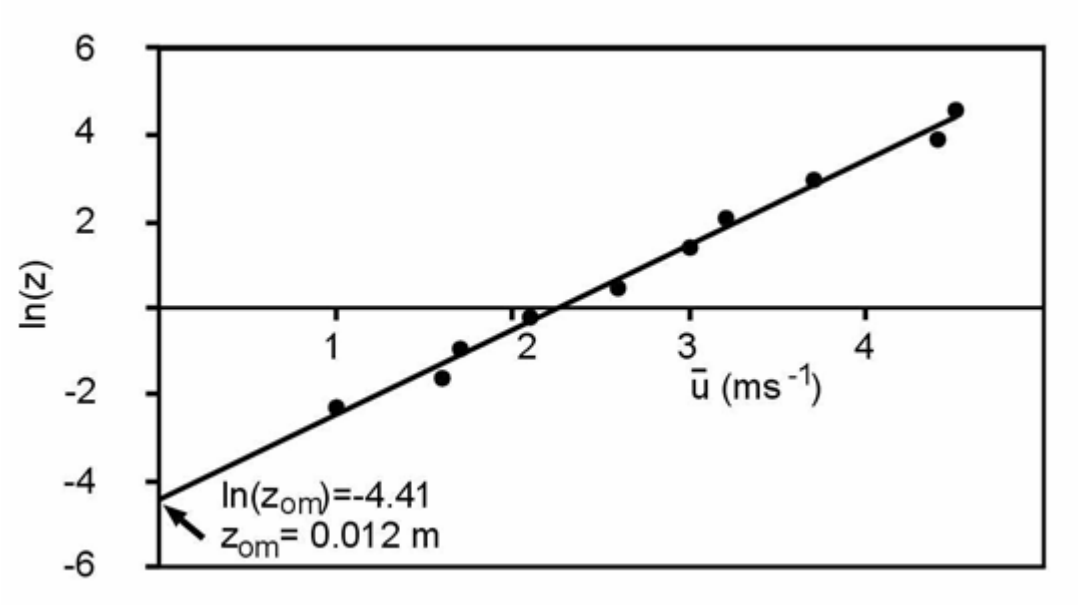


*Figure 5 Example plot of mean wind speed against ln(z). The intercept with the vertical axis leads to $z_{om}$ = 0.012 m.*

In the case of rough surfaces there is some ambiguity concerning the reference level z=0 as used in Eq. 2- Eq. 4. For very sparsely spaced roughness elements on a flat plane this level can be taken at the level of the plane. However, the denser these roughness elements become, the closer to the top the zero level has to be placed. In practice this difficulty is solved by introducing a displacement distance d (m). The reference level (z=0) is at the base of the roughness elements, and the wind speed is zero at $z=d+z_{om}$. The variable (z-d) is then used instead of z Eq. 2- Eq. 4. For example Eq. 4 becomes

$$\bar{u} = \frac{u_*}{k} \ln\left(\frac{z-d}{z_{om}}\right) \qquad \textit{Eq. 5}$$

Figure 6 illustrates the situation for a crop of height h (m). The displacement height d is then usually taken as 0.7 or 0.8 times h. The wind speed becomes zero at $d+z_{om}$.

### 4.2.4 Mean specific humidity and temperature profiles

The approach that led to Eq. 2- Eq. 5 can now be used to derive expressions for the mean specific humidity and temperature profile. In the dynamic sub-layer these are passive admixtures of the air and they do not affect the dynamics of the flow. As opposed to wind speed and momentum, which are vectors, humidity and temperature are scalar quantities. The same holds for $CO_2$ transport.

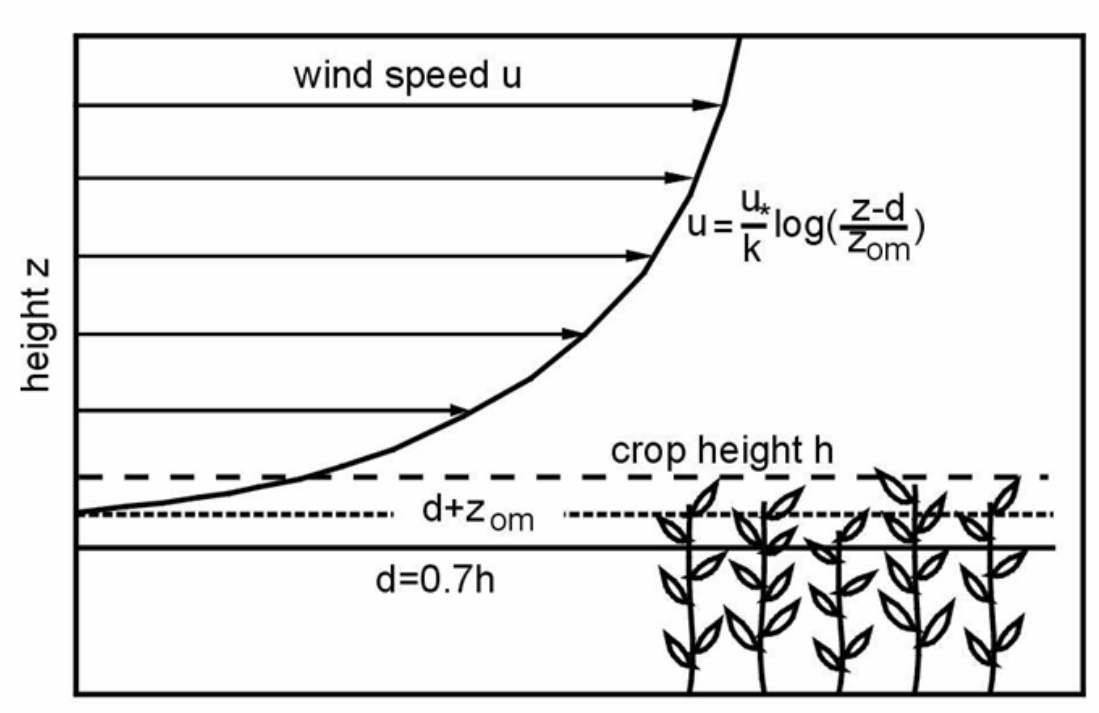


*Figure 6: Vertical distribution of wind speed over a vegetated surface of height h. The profile follows the logarithmic distribution of Eq. 4 . The zero plane displacement d is about 0.7h. The wind speed becomes zero at d+$z_{om}$*

Through application of the same principles as were used in establishing Eq. 2 (Reynolds analogy) the gradient of the specific humidity q(-) can be related to the water vapor flux E (kg $m^{-2}$ $s^{-1}$) by

$$\frac{E}{\rho u_* (z-d)(d\bar{q}/dz)} = -k_v \qquad \textit{Eq. 6}$$

where $k_v=a_vk$ is von Kármán's constant for water vapor. It has been found that $a_v$ is usually close to unity, and the difference between $k_v$ and k will therefore be ignored. Integrating (6) between two arbitrary levels $z_1$ and $z_2$ within the dynamic sublayer yields

$$\bar{q}_1 - \bar{q}_2 = \frac{E}{k\rho u_*} \ln\left(\frac{z_2 - d}{z_1 - d}\right) \qquad \textit{Eq. 7}$$

If $q_s$ is the value of q at the surface, the profile can also be written as (see Eq. 5)

$$\bar{q}_s - \bar{q} = \frac{E}{k\rho u_*} \ln\left(\frac{z - d}{z_{0v}}\right) \qquad \textit{Eq. 8}$$

where $z_{0v}$ (m) is the water vapor roughness length. The integration constant $z_{0v}$ can be visualized as the level above the displacement distance d where the mean specific humidity q would assume its surface value if the logarithmic profile were extrapolated downward. It should be noted that $z_{0v}$ has no real physical meaning because close to the surface diffusive processes prevail and the assumptions underlying Eq. 6-Eq. 8 with regard to turbulent transport are no longer valid.

Similar procedures for temperature profiles are followed, with the exception that potential temperature $\theta$ (K) is used rather than air temperature T (K)

$$\theta = T + \Gamma z \qquad \textit{Eq. 9}$$

where $\Gamma$ is the dry adiabatic lapse rate (0.01 K $m^{-1}$). Because of its low value the difference between $\Gamma$ and T can be ignored in many applications.

The expression for the temperature profile is similar to the relation for specific humidity (Eq. 7)

$$\bar{\theta}_1 - \bar{\theta}_2 = \frac{H}{k\rho c_p u_*} \ln\left(\frac{z_2 - d}{z_1 - d}\right) \qquad \textit{Eq. 10}$$

or

$$\bar{\theta}_s - \bar{\theta} = \frac{H}{k\rho c_p u_*} \ln\left(\frac{z - d}{z_{oh}}\right) \qquad \textit{Eq. 11}$$

where $C_p$ is the specific heat at constant pressure (J $kg^{-1}$ $K^{-1}$), H (W $m^{-2}$) is the sensible heat flux as a result of the temperature differences in the profile and where $z_{oh}$ (m) is the roughness length for sensible heat. The same comments hold for $z_{oh}$ as for $z_{ov}$. Close to the surface diffusive rather than turbulent processes prevail and care should be taken in attaching a physical meaning to $z_{oh}$. The determination of a representative surface temperature $\theta_s$ or $T_s$ is a difficult practical problem, especially with infrared sensor techniques.

### 4.2.5 Stability corrections in the surface sublayer

Above the dynamic sublayer the stability of the atmosphere needs to be considered, that is the effect from the buoyancy resulting from the effective vertical density gradient. The common way to include the stability corrections is through introduction of a variable L (m), the stability length, as was first proposed by Monin and Obukhov (1954). This variable was defined by similarity theory through dimensional analysis of the variables involved

$$L = \frac{-u_*^3 \rho c_p T_a}{kgH} \qquad \textit{Eq. 12}$$

Where g is the acceleration of gravity (9.8 m $s^{-2}$) and $T_a$ is the air temperature (K).

A more precise formulation is

$$L = \frac{-u_*^{\,3}\rho}{kg\left[\left(\frac{H}{c_p T_a}\right) + 0.61E\right]} \qquad \textit{Eq. 13}$$

However, Eq. 12 is often used instead of Eq. 13. After introducing the dimensionless variable $\zeta$ as

$$\zeta = \frac{z-d}{L} \qquad \textit{Eq. 14}$$

the expressions for wind speed, water vapor and temperature become

$$\frac{k(z-d)}{u_*}\frac{du}{dz} = \phi_{sm}(\zeta) \qquad \textit{Eq. 15}$$

$$-\frac{k\rho u_*(z-d)}{E}\frac{dq}{dz} = \phi_{sv}(\zeta) \qquad \textit{Eq. 16}$$

$$-\frac{k\rho c_p u_*(z-d)}{H}\frac{d\theta}{dz} = \phi_{sh}(\zeta) \qquad \textit{Eq. 17}$$

After integrating Eq. 15, Eq. 16 and Eq. 17 the following set of equations is obtained

$$u_2 - u_1 = \frac{u_*}{k}\left[\ln\left(\frac{\zeta_2}{\zeta_1}\right) - \psi_{sm}(\zeta_2) + \psi_{sm}(\zeta_1)\right] \qquad \textit{Eq. 18}$$

$$q_1 - q_2 = \frac{E}{k\rho u_*}\left[\ln\left(\frac{\zeta_2}{\zeta_1}\right) - \psi_{sv}(\zeta_2) + \psi_{sv}(\zeta_1)\right] \qquad \textit{Eq. 19}$$

$$\theta_1 - \theta_2 = \frac{H}{k\rho c_p u_*}\left[\ln\left(\frac{\zeta_2}{\zeta_1}\right) - \psi_{sh}(\zeta_2) + \psi_{sh}(\zeta_1)\right] \qquad \textit{Eq. 20}$$

Note that the overbars in these equations have been left out for convenience. Averaging is implied in the remainder of this chapter. The $\psi$ functions are defined as

$$\psi = \int\left(\frac{1-\phi(\zeta)}{\zeta}\right)d\zeta \qquad \textit{Eq. 21}$$

Much experimental work has been done to determine the proper $\phi$ and $\psi$ functions for different meteorological conditions and usually a distinction is made between stable conditions, prevailing at night, and unstable conditions, arising from the strongly convective conditions normally encountered during the day. Under unstable conditions heat flow is away from the surface while under stable circumstances heat flow is towards the surface. Under neutral conditions in the dynamic sublayer, the $\phi$ functions are equal to unity, and the equations reduce to those of the mean logarithmic profiles discussed above.

*Unstable conditions*

Several experimentally determined forms of the functions $\phi$ exist and one common choice is

$$\phi_{sv} = \phi_{sh} = \phi_{sm}^{\,2} = (1 - 16\zeta)^{-1/2} \qquad \textit{Eq. 22}$$

where the following $\psi$-functions are found when using Eq. 22 in the evaluation of Eq. 21.

$$\psi_{sm} = 2\ln\left[\frac{(1+x)}{2}\right] + \ln\left[\frac{(1+x^2)}{2}\right] - 2\arctan(x) + \pi/2 \qquad \textit{Eq. 23}$$

$$\psi_{sv}(\zeta) = \psi_{sh}(\zeta) = 2\ln\left[\frac{(1+x^2}{2}\right] \qquad \textit{Eq. 24}$$

and x is defined as

$$x = (1 - 16\zeta)^{1/4} \qquad \textit{Eq. 25}$$

*Stable conditions*

Some discrepancies exist between various experimental results, and many forms of $\phi$ are suggested in the literature. It appears, however, that fluxes are small under stable conditions and the exact form of these relations is not critical. For practical work it was suggested already by Brutsaert (1982) to use

$$\phi_{sv} = \phi_{sm} = \phi_{sh} = 1 + 5\zeta \qquad \textit{for } 0 < \zeta < 1$$

$$\phi_{sv} = \phi_{sm} = \phi_{sh} = 6 \qquad \textit{for } \zeta > 1 \qquad \textit{Eq. 26}$$

### 4.2.6 Applications

Suppose that measurements of wind are taken at a level $z_1$, and measurements of temperature at levels $z_1$ and at the surface (z-d=0). Suppose further that neutral conditions prevail and therefore stability corrections do not have to be made. Then Eq. 5 and Eq. 11 allow determination of $u_*$ and H. First $u_*$ is determined from Eq. 5

$$u_* = \frac{ku}{\ln\left(\frac{z_1 - d}{z_{om}}\right)} \qquad \textit{Eq. 27}$$

Then H is determined by substitution of Eq. 27 into Eq. 11 as

$$H = \frac{k^2 \rho\, c_p\, u\left(T_s - T_1\right)}{\ln\left(\frac{z_1 - d}{z_{om}}\right)\ln\left(\frac{z_1 - d}{z_{oh}}\right)} \qquad \textit{Eq. 28}$$

This can be done provided of course values for $z_{om}$, $z_{oh}$ and d have been determined beforehand. The surface roughness for ordinary farm and grassland is usually much smaller than 0.1 m. and may range up to 0.5 m. for dense forests. The values for $z_{oh}$ show much more variability (see e.g. Sugita and Brutsaert, 1990 and Verhoef et al., 1997). For reference crop evapotranspiration (Allen et al., 1994) $z_{oh}$ is normally taken as 0.1 $z_{om}$. The logarithmic ratio of the roughness lengths for momentum and heat is defined as $kB^{-1}$

$$kB^{-1} = \ln\left(\frac{z_{om}}{z_{oh}}\right) \qquad \textit{Eq. 29}$$

For a ratio of 10 this gives $kB^{-1}$=2.3. Especially in semi-arid areas much higher values may be found and, moreover, these show distinct diurnal and seasonal variability. The interpretation of $z_{oh}$ still appears unclear in many field situations.

Eq. 28 is used in the Penman-Monteith formulation (Allen et al., 1998) of reference crop evapotranspiration through the definition of sensible heat H as

$$H = \rho c_p \frac{T_s - T_z}{r_{ah}} \qquad \textit{Eq. 30}$$

where $T_z$ (K) is the air temperature at height z, and $r_{ah}$ (s $m^{-1}$) is defined as the aerodynamic resistance to heat transport. Comparing Eq. 28 with Eq. 30 this leads to

$$r_{ah} = \frac{1}{k^2 u}\left[\ln\left(\frac{z - d}{z_{om}}\right)\right]\left[\ln\left(\frac{z - d}{z_{oh}}\right)\right] \qquad \textit{Eq. 31}$$

If the stability corrections $\psi$ are used in the formulation of the profile equations, then Eq. 28 is changed to

$$H = \frac{k^2 \rho c_p u (T_s - T_z)}{\left[\ln\left(\frac{z-d}{z_{om}}\right) - \psi_{sm}\left(\frac{z-d}{L}\right)\right]\left[\ln\left(\frac{z-d}{z_{oh}}\right) - \psi_{sh}\left(\frac{z-d}{L}\right)\right]} \qquad \textit{Eq. 32}$$

Since L depends on H through Eq. 13, Eq. 32 is an implicit equation in H, which is usually solved by iteration.

Note that the water vapor flux E can in principle be solved in the same way as the sensible heat flux H, for example, by combining Eq. 8 and Eq. 5 for neutral atmospheric conditions.

## 4.3 Methods based on field measurements

There are many methods developed to measure actual evapotranspiration. The following methods can be distinguished: pan evaporation method, lysimeters, flux profile measurements, the FAO56 method, the Bowen ratio, eddy-correlation, and scintillometer measurements. The most important methods will be discussed in this chapter. For this project these methods are not suitable because they are all, with the exception of the scintillometer, point methods which do not provide spatial patterns of actual evapotranspiration. The discussion of the principles used is however very relevant.

Most methods used to estimate the latent heat flux are based on a combination of the energy balance approach, flux methods and the Monin-Obukhov similarity theory (Monin and Obukhov, 1954). The energy balance is given by:

$$Q^* = G_0 + H + L_v E \qquad \textit{Eq. 33}$$

Where $Q^*$ (W m$^{-2}$) is the net radiation, $H$ (W m$^{-2}$) is the sensible heat flux and $L_v E$ (W m$^{-2}$) is the latent heat flux ( $L_v$ (J kg$^{-1}$) is the latent heat of vaporization and $E$ (kg m$^{-2}$ s$^{-1}$) is the actual evapotranspiration) and $G_0$ is the soil heat flux (W m$^{-2}$). The net radiation produced by the sun is shared between the two atmospheric convective fluxes and the soil heat flux. Commonly used flux profile relations based on layer resistance schemes have been derived for $H$ and $L_v E$ :

$$H = \rho c_p \frac{T_0 - T}{r_a} \qquad \textit{Eq. 34}$$

and

$$L_v E = \frac{\rho c_p}{\gamma} \frac{e_0 - e}{r_a + r_s} \qquad \text{Eq. 35}$$

Where $\rho$ (kg m$^{-3}$) and $c_p$ (J kg$^{-1}$ K$^{-1}$) are the density and specific heat of air at constant pressure, $\gamma$ is the psychometric constant, $T_0$ (K) is the temperature at the earth surface, $T$ (K) is the air temperature at an height of 2 meter, $e_0$ (Pa) is the surface vapor pressure, $e$ (Pa) is the vapor pressure at a height of 2 meter, $r_a$ (s m$^{-1}$) is the aerodynamic resistance, $r_s$ (s m$^{-1}$) is the surface resistance. These flux profiles assume that vertical fluxes of momentum, heat and water can be quantified by gradients in wind, temperature and vapor pressure respectively. The aerodynamic resistance is derived using the Monin-Obukhov similarity theory as described above.

By assuming that over a water surface the saturated vapor pressure ($e_w$ (Pa)) is equal to the actual vapor pressure the solution of this set of equations leads to the famous Penman-Monteith equation (Penman (1948), Monteith (1965)).

$$L_v E = \frac{s(Q^* - G) + \frac{\rho c_p}{r_a}(e_w(T) - e)}{s + \gamma(1 + \frac{r_s}{r_a})} \qquad \text{Eq. 36}$$

with $s$ being the slope of the saturation vapor pressure temperature relationship and $e_w(T)$ the saturated . The determination of instantaneous aerodynamic and surface resistances is complex. The atmospheric resistance depends on the atmospheric stability, zero displacement heights and, roughness lengths for heat transfer and wind speed. The surface resistance describes the resistance of vapor flow through the transpiring crop and evaporating soil surface. The surface resistance is depending on the soil cover, the type of crop, air temperature, incident solar radiation, moisture deficit and available soil moisture.

### 4.3.1 FAO 56 methodology

An operational application of the above equations is the method described in FAO's Irrigation and Drainage paper no. 56 (Allen et al., 1998). The FAO 56 method is applied in numerous countries by water managers and irrigation engineers. The FAO 56 methodology calculates reference evaporation ($ET_0$) using the Penman-Monteith equation for a hypothetical reference surface defined as " a hypothetical reference crop with an assumed crop height of 0.12 m, a fixed surface resistance of 70 s m$^{-1}$ and an albedo of 0.23. The method uses measured meteorological data as inputs (air temperature, humidity, radiation and wind speed). The following equations and assumptions are used in deriving the variables of the Penman-Monteith equation.

- The net radiation is calculated by:

$$Q^* = (1 - \alpha_{surface})Q_{sw} + \varepsilon_{surface}Q_{lw} - \varepsilon_s \sigma T_{surface}^4 \qquad \text{Eq. 37}$$

Where $\alpha_{surface}$ is the surface albedo, $Q_{sw}$ (W m$^{-2}$) is the incident shortwave solar radiation, $\varepsilon_{surface}$ is the surface emissivity, $Q_{lw}$ (W m$^{-2}$) is the incident long wave radiation, $\sigma$ is the Stefan-Boltzmann constant (5.67 10$^{-8}$ W m$^{-2}$ K$^{-4}$) and $T_{surface}$ (K) is the surface temperature.

- The soil heat flux is calculated by

$$G = C\frac{T_i + T_{i-1}}{\Delta t}\Delta z \qquad \textit{Eq. 38}$$

Where $C$ is the soil heat capacity (J m$^{-3}$ K), $T_i$ (K) is the air temperature at time i, $T_{i-1}$ (K) is the air temperature at time i-1, $\Delta t$ (s) is the length of the time interval, $\Delta z$ (m) is the effective soil depth.

- The variables $e_w(T)$, $e$ and $s$ are calculated using air temperature and relative humidity measurements.
- The surface resistance is a function of the Leaf Area Index and for the reference crop equal to 70 m s$^{-1}$.
- The aerodynamic resistance, given by the Monin-Obhukov similarity theory (Monin, 1971, Obukhov, 1946) is given by:

$$r_a = \frac{\ln\left[\frac{z_m - d}{z_{0m}}\right]\ln\left[\frac{z_h - d}{z_{0h}}\right]}{k^2 u_z} \qquad \textit{Eq. 39}$$

Where $z_m$ (m) is the height of the wind measurement, $z_{0m}$ (m) is the roughness length for momentum transfer, $z_{oh}$ (m) is the roughness length for heat and vapor transfer, $z_h$ (m) is the height of the humidity measurement, $d$ (m) is the zero plane displacement height, $k$ is the Von Karman constant (0.4) and $u_z$ (m s$^{-1}$) is the wind speed at height $z_m$. For the reference crop the aerodynamic resistance can be reduced to:

$$r_a = \frac{208}{u_2} \qquad \textit{Eq. 40}$$

The reference evapotranspiration is only affected by climatic parameters and can be computed by weather variables only and is valid for the hypothetical reference crop under well watered conditions. The next step in the FAO procedure is to determine the crop evapotranspiration under standard

condition for a specific crop ($ET_c$); disease free, well fertilized, grown in large fields, under optimum soil water conditions. The only difference between the $ET_c$ and $ET_0$ is caused by differences between leaf anatomy, stomata characteristics, aerodynamic properties and albedo. $ET_c$ is given by

$$ET_c = K_c ET_0 \qquad \textit{Eq. 41}$$

Where $K_c$ is the crop coefficient. The crop coefficient varies in time and depends on the crop growth stage and the climatic conditions or management operations (e.g. irrigation) during the stage. If $ET_c$ Is required on a daily basis it is necessary to split the crop coefficient into a separate plant transpiration and soil evaporation coefficient. $ET_c$ is also referred to as potential evapotranspiration. In practice plants usually are under environmental stress (e.g. soil water stress) which causes the actual evapotranspiration to be lower than the potential evapotranspiration. The FAO56 methodology takes environmental stress into account by introducing an environmental stress factor. The actual evapotranspiration ($ET_{c\ adj}$) is given by:

$$ET_c = K_s K_c ET_0 \qquad \textit{Eq. 42}$$

Where $K_s$ is the environmental stress factor. An overview is given in Figure 3.

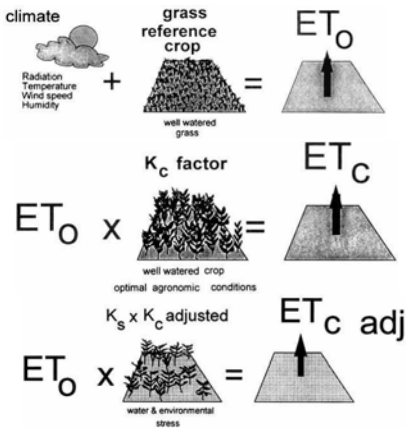


*Figure 7: Reference evepotranspiration ($ET_0$), crop evapotranspiration under standard conditions ($ET_c$) and non-standard condition ($ET_{c\ adj}$), (Allen et al., 1998)*

The FAO56 methodology is relatively straightforward and therefore applied in many countries across the world; however there is one disadvantage. The calculated reference evapotranspiration is based on meteorological information for a specific station and is therefore not known spatially distributed. Sensitive variables in the potential evapotranspiration calculation, such as the surface temperature,

radiation, wind speed and relative humidity are all highly variable in space. Surface and aerodynamic resistances are also varying in space and depend on land use and wind speed. The calculation of actual evapotranspiration depends on a crop factor, which depends on the development stage, type and variety of the crop and the soil cover, and on an environmental stress factor which is also location specific. In other words the methodology is not suitable to estimate spatially distributed evapotranspiration. Remote Sensing data with increased spatial and temporal resolution is therefore a useful tool to provide information on evapotranspiration on various temporal and spatial scales.

The FAO56 method estimates evapotranspiration on the basis of meteorological input data at a specific location.

### 4.3.2 Bowen Ratio

The Bowen ratio method (Bowen, 1926) is also based on the energy balance. The Bowen ratio ( $\beta$ ) is defined as the quotient of sensible and latent heat flux:

$$\beta = \frac{H}{L_v E} = \frac{c_p \Delta\bar{\theta} / r_{ah}}{L_v \Delta\bar{q} / r_{av}} = \frac{c_p \Delta\bar{\theta}}{L_v \Delta\bar{q}} \qquad \textit{Eq. 43}$$

Where $\Delta\bar{\theta}$ (K) is the average difference in potential temperature between two heights, $\Delta\bar{q}$ is the average difference in specific humidity, and $r_{ah}$ and $r_{av}$ are the aerodynamic resistances to heat and vapor transport respectively. Since the stability functions for heat and vapor are similar Bowen assumed the aerodynamic resistances to heat and vapor transport are also equal. The Bowen ration can therefore be determined by measurements of temperature and specific humidity at two different heights above the surface.

By combining the Bowen ratio with energy balance the latent heat flux can be determined as follows:

$$L_v E = \frac{Q^* - G}{1 + \beta} \qquad \textit{Eq. 44}$$

The net radiation can be determined by a net radiometer and the soil heat flux by soil heat flux plates.

The advantage of the Bowen Ratio method is the ability to measure actual evapotranspiration and that it eliminates wind and turbulent transfer coefficients. The disadvantage is the need for fragile sensors and data loggers, the need for a upwind fetch and the numerical instability when the Bowen ration approaches -1.

### 4.3.3 Eddy correlation method

The eddy correlation method is based on Reynolds decomposition, which forms the basis of the turbulence theory. The value of a quantity A can be written as:

$$A = \overline{A} + A' \qquad \textit{Eq. 45}$$

Where $A$ s the value of quantity $A$ at time t, $\overline{A}$ is the average value of $A$ and $A'$ is the turbulent deviation of the average, generally referred to as the fluctuation part.

Evaporation (kg $m^{-2}$) can be written as the average product over a certain time interval of the vertical component of the wind speed $W$ (m $s^{-1}$), the air density $\rho$ (kg $m^{-3}$) and the specific air humidity $q$ :

$$E = \overline{w\rho\, q} \qquad \textit{Eq. 46}$$

Using Reynolds decomposition and some simplification this can be rewritten to:

$$E = \overline{\rho}\,\overline{w'q'} \qquad \textit{Eq. 47}$$

This means that the evapotranspiration can be calculated by the covariance of the vertical wind speed and specific humidity and the air density. This requires high frequency sensors which can measure the wind speed and specific humidity around 10 times per second. This can be achieved by using sonic anemometers which measure the different directional components of the wind speed and the sonic temperature and a Licor sensor which measures $H_2O$ concentrations in the air.

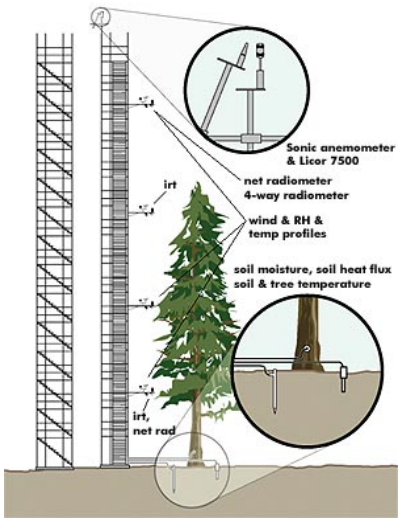


*Figure 8: Typical set-up of an eddy correlation tower*

The advantage of the eddy correlation method is that it directly measures atmospheric turbulence, but skilled staff, complex instrumentation and adequate upwind fetch is required.

### 4.3.4 Scintillometer

A methodology which estimates evapotranspiration at a scale of several kilometers is the scintillation method. The scintillation method is also based on the Monin-Obhukov similarity theory and it is applicable over distances as long as 5 km (De Bruin et al., 1995). A large scintillometer is a device which consists of a transmitter and a receiver and measures the turbulent intensity of the refraction index of air. Variations in the refraction index are caused by fluctuations in temperature and humidity, which can be used to calculate the latent heat flux using the flux-profile relationships and the similarity theory. The scintillation method is an intermediate between in situ field measurements and large area Remote Sensing estimates. Figure 9 shows the operational principle of a scintillometer. Light from a Light Emitting Diode (LED) is bundled in a parallel beam and modulated by a 7KHz oscillator. The light signal is amplified by a receiver and the signal is representative of changes in the refractive index of the atmosphere, which is in its turn the result of the sensible heat flux.

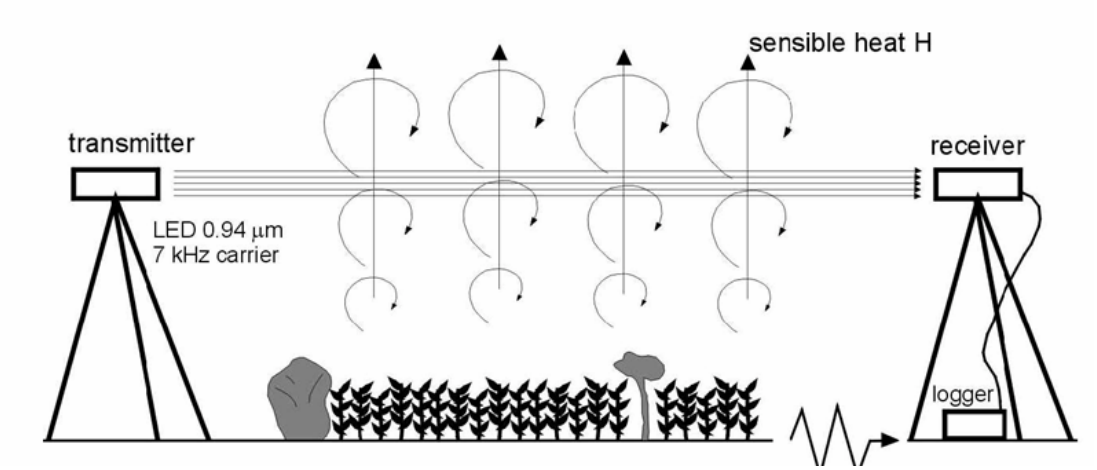


*Figure 9: Operational principle of a scintillometer*

The refractive index structure parameter ($C_n$) is related to the temperature structure parameter ($C_T$) as

$$C_T = 10^6 \left( \frac{C_n T^2}{0.78 p} \right) \cdot \left( 1 + \frac{0.03}{\beta} \right) \qquad \textit{Eq. 48}$$

Where p is the atmospheric pressure (bar), T is the temperature (K) and β is the Bowen ratio. The sensible heat flux H is then related to $C_T$ through, for example, a relation of the form (Koshiek, 1982)

$$H = A C_T^{3/2} \qquad \textit{Eq. 49}$$

Where A is a constant, depending on temperature and boundary layer parameters. For dry lands the methods works fine since β is usually greater than 1.

## 4.4 Remote Sensing methods

It is difficult to classify Remote Sensing algorithms to estimate evapotranspiration (Kite and Droogers, 2000, Courault et al, 2005) since they range from empirical to completely deterministic, with no clear distinction between the different approaches. The complexity of the methods also greatly varies. The common denominator in most methods is that they allow spatially distributed estimates of ET and incorporate (parts of) the energy balance theory, the Monin-Obukhov similarity hypothesis and/or the flux profile relationships. Different examples of methods found in literature in increasing order of complexity and data needs are described below. The following (arbitrary) classification of methods is used:

- Thermal infra-red empirical methods
- Feedback approach
- Land parameterization and Remote Sensing
- Energy balance and similarity theory methods

### 4.4.1 Thermal infra-red empirical methods

This method assumes that it is possible to directly relate daily evapotranspiration (m) to the net radiation (W $m^{-2}$) and the instantaneous difference between surface and air temperature (K) according to the following relationship:

$$ET_d = Q^* + A - B(T_{surface} - T_{air}) \qquad \text{Eq. 50}$$

Where A and B are area specific constants. The methodology assumes that the soil heat flux is negligible when considering daily ET. It also assumes that the ratio of sensible heat flux and net radiation is constant throughout the day. Several authors have implemented this approach (Lagouarde, 1991, Seguin and Itier, 1983, Riou et al., 1998). Surface temperature as well as net radiation can be relatively straightforwardly derived from the spectral reflectance of the thermal and visible bands. The largest hurdle in the process is to acquire a reliable estimate of the air temperature. Two approaches are mentioned by Courault et al. (2005). One approach is to use geo-statistical interpolation methods of meteorological observations. Accuracy typically ranges from 20-30%. A second approach is to estimate $T_a$ using empirical relationships with vegetation indices such as SAVI and NDVI.

### 4.4.2 Feedback approach

A number of authors have used the Penman-Monteith equation as basis to derive ET using Remote Sensing. Granger for example applies a modified version of the Penman-Monteith equation, which has been adapted to the unsaturated case and which uses vapour pressure deficit and net radiation as inputs, to calculate actual evapotranspiration ($ET_{act}$) (Granger, 1989). Granger uses the relative evapotranspiration ($ET_{rel}$), which is defined as the ratio between actual and potential evapotranspiration, to account for non-saturated conditions. By establishing an empirical relationship between $ET_{rel}$ and the drying power, which is defined as $ET_{act}$ / ($ET_{act}$ + $Q^*$), $ET_{act}$ can be determined

on the basis of net radiation, surface temperature, vapour deficit, and roughness heights without the necessity for prior estimates of the potential evapotranspitaion, air temperature and humidity. Granger (1995, 1997, 2000) uses the visible channels to calculate the surface albedo, which is used to calculate net radiation through:

$$Q^* = Q_{swn} + Q_{lwn} \qquad \textit{Eq. 51}$$

Where $Q^*$ (W m$^{-2}$) is the net radiation, $Q_{swn}$ (W m$^{-2}$) is the net shortwave radiation and $Q_{lwn}$ (W m$^{-2}$) is the net longwave radiation. The $Q_{swn}$ is calculated by:

$$Q_{swn} = Q_{sw}(1-\alpha) \qquad \textit{Eq. 52}$$

Where $\alpha$ is the broad band surface albedo. Granger (1997) shows that AVHRR channel 2 albedo is a reasonable estimate of the broad band surface albedo. The net long wave radiation is usually estimated by measurements of temperature and humidity. Granger and Gray assume however that on clear days for dry continental atmospheres the net long wave radiation is proportional to the incoming shortwave radiation through:

$$Q_{lwn} = -4.25 - 0.24Q_{sw} \qquad \textit{Eq. 53}$$

A salient characteristic of the methodology is that a feedback mechanism is implemented to directly estimate vapour pressure deficit. The mechanism states that the temperature and humidity in the air are a reflection of the portioning of energy at the earth's surface. Granger applies the converse and demonstrates that the observed surface temperature is a sufficiently accurate indicator of air humidity. Using field data the following empirical relation was derived for the daily vapour pressure deficit:

$$VP_{def} = -0.278 - 0.015T_{ltm} + 0.669VP^*_{TS} \qquad \textit{Eq. 54}$$

Where $VP_{def}$ (Pa) is the daily vapour pressure deficit, $T_{ltm}$ (K) is the long term mean air temperature and $VP^*_{TS}$ (Pa) is the saturation vapour pressure at the surface temperature.
To calculate the surface temperature Granger adopts a split window technique used by Prata and Platt (1991), which uses surface emissivities ($\varepsilon$) and brightness temperatures ($T$ (K)) of AVHRR channels 4 and 5 respectively according to:

$$T_s = 2.09 + (2.84T_4 / \varepsilon_4) - (2.03T_5 / \varepsilon_5) \qquad \textit{Eq. 55}$$

The last variable for which spatial information is required is the surface roughness, needed to determine the aerodynamic resistance in the Penman-Monteith equation. Vegetation across basins usually varies considerably in type and height and therefore in roughness. Granger uses a linear relationship between the Normalized Difference Vegetation Index (NDVI) and surface roughness using known vegetation heights.

### 4.4.3 Land parameterization and Remote Sensing

Remote Sensing is also used commonly in combination with process based basin scale or agro-hydrological models to perform spatially explicit estimates of evapotranspiration.

Courault et. al. (2005) distinguish two types in this category; remote sensing forced models and assimilation of numerical models. Generally these models describe the exchanges between soil plant and atmosphere according to the physical processes occurring in each compartment with generally a fine time step (second, hour). Different complexity levels appear according to the process description: for example, if the vegetation and soil behavior are separated, then evaporation and transpiration are computed with a surface temperature for each part. Increasing levels of complexity require a higher degree of parameterization, which can (sometimes) be estimated by remote sensing data. A few examples are given below.

Choudhury and DiGirolamo (1998) for example use a biophysical model which links the water, energy and carbon processes by using satellite and ancillary data to quantify total evaporation, transpiration and biomass production (Choudhury, 1997). Transpiration is calculated using the Penman–Monteith equation in which the minimum canopy stomatal resistance is determined by the rate of carbon assimilation. Soil evaporation is computed as energy-limited and exfiltration limited. The rate of carbon assimilation, together with estimated respiration and soil water stress provides biomass production. Satellite observations are used to obtain fractional vegetation cover, surface albedo, incident solar and Photosynthetically Active Radiation (PAR), fractional cloud cover, air temperature, and vapour pressure. Precipitation is obtained by combining satellite and surface observations. Biophysical parameters of the model (e.g. soil hydraulic characteristics, and maximum carbon assimilation rate of a leaf) are determined from published records and land cover of the area.

### 4.4.4 Energy balance and similarity theory methods

#### 4.4.4.1 SEBAL

The Surface Energy Balance Algorithm for Land (SEBAL) formulated by Bastiaanssen et al. (1998) is an image-processing model comprised of 25 computational steps that calculates the actual (ETact) and potential evapotranspiration rates (ETpot) as well as other energy exchanges between land and atmosphere. The key input data for SEBAL consists of spectral radiance in the visible, near-infrared and thermal infrared part of the spectrum. SEBAL computes a complete radiation and energy balance along with the resistances for momentum, heat and water vapour transport for every individual pixel. The resistances are a function of state conditions such as soil water potential (and thus soil moisture), wind speed and air temperature and change from day-to-day.

Satellite radiances will be converted first into land surface characteristics such as surface albedo, leaf area index, vegetation index and surface temperature. These land surface characteristics can be derived from different types of satellites. First, an instantaneous evapotranspiration is computed, that is subsequently scaled up to 24 hours and longer periods.

In addition to satellite images, the SEBAL model requires the following routine weather data parameters:

- Wind speed
- Humidity
- Solar radiation
- Air Temperature

There is no data on land use, soil type or hydrological conditions required to apply SEBAL.

The primary basis for the SEBAL model is the surface energy balance. The instantaneous latent heat flux is calculated for each pixel of the image as a 'residual' of the surface energy budget equation:

$$L_v E = Q^* - G_0 - H \qquad \textit{Eq. 56}$$

Where LvE is the latent heat flux (W m-2), Q* is the net radiation flux at the surface (W/m2), G is the soil heat flux (W/m2), and H is the sensible heat flux to the air (W/m2).
The net radiation (Q*) is computed by subtracting all outgoing radiant fluxes from all incoming radiant fluxes according to

$$Q^* = Q_{s\downarrow} - \alpha Q_{s\downarrow} + Q_{L\downarrow} - Q_{L\uparrow} - (1 - \varepsilon_0) Q_{L\downarrow} \qquad \textit{Eq. 57}$$

Where $Q_{s\square}$ is the incoming short-wave radiation (W/m2), $\alpha$ is the surface albedo (dimensionless), $Q_{L\square}$ is the incoming long wave radiation (W/m2), $Q_{L\square}$ is the outgoing long wave radiation (W/m2), and $\varepsilon_o$ is the surface thermal emissivity (dimensionless). In Eq. 57, the amount of net short-wave radiation ($Q_{S\square}$ - $\alpha$ $Q_{S\square}$) that remains available at the surface, is a function of the surface albedo ($\alpha$). The broad band surface albedo $\alpha$ is derived from the narrow band spectral reflectances $\alpha$ (λ) measured by each satellite band. The incoming short-wave radiation ($Q_{S\square}$) is computed using the solar constant, the solar incidence angle, a relative earth-sun distance, and a computed broad band atmospheric transmissivity. This latter transmissivity can be estimated from sunshine duration or inferred from pyranometer measurements (if available). The incoming long wave radiation ($Q_{L\square}$) is computed using a modified Stefan-Boltzmann equation with an apparent emissivity that is coupled to the shortwave atmospheric transmissivity and a measured air temperature. Outgoing long wave radiation ($Q_{L\square}$) is computed using the Stefan-Boltzmann equation with a calculated surface emissivity and surface temperature. Surface temperatures are computed from the satellite measurements of thermal radiances.

In Eq. 56, the soil heat flux ($G_0$) and sensible heat flux (H) are subtracted from the net radiation flux at the surface ($Q^*$) to compute the "residual" energy available for evapotranspiration ($L_vE$). Soil heat flux is empirically calculated as a $G_0$/Rn fraction using vegetation indices, surface temperature, and surface albedo. Sensible heat flux is computed using wind speed observations, estimated surface roughness, and surface to air temperature differences (ΔT) that are obtained through a sophisticated self-calibration between dry ($L_vE \approx 0$) and wet ($H \approx 0$) pixels. For the wet pixel it is assumed that ΔT = 0. For the dry pixel ΔT is given by:

$$\Delta T = \frac{Hr_{ah}}{\rho_{air} c_p} \qquad \textit{Eq. 58}$$

Where $r_{ah}$ (s $m^{-1}$) is the near surface aerodynamic resistance to heat transfer, $\rho_{air}$ (kg $m^{-3}$) is the moist air density and $c_p$ (J $kg^{-1}$) is the specific heat at constant pressure. SEBAL solves this implicit equation iteratively. In first instance free convection is assumed, thereafter mixed convection is applied and buoyancy effects according the Monin-Obukhov similarity hypothesis are incorporated in the pixel dependent aerodynamic resistance to heat transfer. Empirically it has been shown that there is a linear relation between surface temperature ($T_0$) and ΔT. This relation is used to estimate ΔT for all pixels in the image.

The $L_vE$ time integration is an interesting property of SEBAL. Knowing the instantaneous soil, latent and sensible heat fluxes makes it possible to calculate the evaporative fraction given by:

$$\Lambda = \frac{L_v E}{Q^* - G} \qquad \textit{Eq. 59}$$

The most important assumption of SEBAL is that the evaporative fraction is constant during the day. For periods longer than one day it may be assumed that the soil heat flux equals 0. The 24hr latent heat flux can therefore be determined by

$$L_v E_{24hr} = \Lambda Q^*_{24hr} \qquad \textit{Eq. 60}$$

The final step is to calculate monthly evapotranspiration data. This achieved by inserting $L_vE_{24hr}$ into the Penman-Monteith equation (Eq. 36). Using this approach it is possible to inversely determine the surface resistance ($r_s$). Knowing the spatial distribution of the surface resistance makes it possible to calculate ET based on the Penman-Monteith equation and meteorological data for all days without satellite imagery.

#### 4.4.4.2 SEBS and (S-)SEBI

The surface energy balance system (SEBS) is another semi-empirical process based method. The method is also based on the evaporative fraction in a manner similar to SEBAL. The method was first described by Menenti and Choudhury (1993). The concept was later included in a more comprehensive framework by Su (2002). A simplified method, called S-SEBI, which estimates surface fluxes from Remote Sensing was later further developed by Roerink et al. (2000). S-SEBI determines a reflectance dependant maximum and minimum temperature for dry ($T_H$) and wet pixels ($T_{LE}$) and the evaporative fractions is determines as:

$$\Lambda = \frac{T_H - T_0}{T_H - T_{LE}} \qquad \textit{Eq. 61}$$

The method assumes that at limiting cases at dry and wet pixels there is a linear relation between the maximum $L_vE$ and H and surface reflectance ($r_0$). The method furthermore assumes that

$$T_H = a_H + b_H r_0 \quad \textit{Eq. 62}$$

$$T_{LE} = a_{LE} + b_{LE} r_0 \quad \textit{Eq. 63}$$

$$G_0 = f(NDVI, r_0) Q^* \quad \textit{Eq. 64}$$

$$H = (1 - \Lambda)(Q^* - G_0) \quad \textit{Eq. 65}$$

$$L_v E = \Lambda(Q^* - G_0) \quad \textit{Eq. 66}$$

Because of the dependence on reflectance the major advantage of the method is that no additional meteorological data are required to determine the turbulent fluxes.

## 4.5 Conclusions

The objective of the this project is to use spatial patterns of actual evapotranspiration in the calibration of hydrological models as opposed to more traditional methods which use hydrograph data only. The GO project therefore requires multi-temporal spatially explicit evapotranspiration across the study area. Remote Sensing is the only appropriate tool to generate these data. The point methods discussed in Chapter 4.3 are therefore not suitable.

The Remote Sensing methods discussed provide a range of options. The thermal infra-red method, although straightforward, is a purely empirical approach which depends on meteorological data and is therefore considered less suitable. The feedback approach described by Granger (1998) is a suitable methodology which can be applied across a number of sensors, is also physically based and relatively straightforward. The comprehensive energy balance methods such as SEBAL and SEBS are the most complete, but also the most complex methods. SEBAL has been applied in numerous projects across the globe and is therefore operationally more applicable.

Depending on the costs and complexity it is therefore proposed to apply either the feedback approach or SEBAL in this project to map the actual evapotranspiration in the Krishna basin.

# 5 Calibration methodologies in hydrological modelling

## 5.1 Introduction

The number of major water related disasters such as droughts and floods is on the rise, as well as the number of people affected, total loss in lives, and economic damage. Improved water management is highly required and it is evident that the current focus on day-to-day management should shift to more strategic planning. A key issue in this strategic planning of water resources is the ability to have proper planning and management tools available. These tools can be divided in Operational and Strategic Decision Support Systems: O-DSS and S-DSS, both relying on simulation models that can mimic reality. The O-DSS are mainly hydraulic oriented models able to predict on a time scale from hours to days in high detail how water will flow in river and canal systems, relying on accurate flow measurements upstream to predict timing and quantity of water downstream. These systems have been very effective in reducing the number of fatalities by so-called early-warning systems, but are not very helpful in a more strategic planning of water resources management.

The Strategic Decision Support Systems (S-DSS) have a much more hydrological focus, describing the entire water cycle including natural as well as human induced processes. The objective of these tools is not to predict as accurate as possible the time a flood or drought might occur, but the probability of exceedance of these events and what long-term options might be feasible to reduce these risks. Besides this capability to estimate these extremes, these S-DSS are extremely powerful in evaluating the impact of changes in water management such as reservoir building, changes in water allocation between and within sectors, and impact of climate change.

Despite substantial progress in the development of these S-DSS techniques, the weakest part is currently the lack of data to apply and calibrate these S-DSSs. Traditionally, these S-DSSs are fine-tuned by a calibration process where observed hydrographs are compared to simulated ones. By adjusting the most sensitive and most unreliable input parameters the S-DSS can be calibrated and performs better in describing the current situation and is therefore also more reliable to explore water management options for the future. It must be emphasized here that this is the standard practice for almost every hydrological modeling study. It is clear that in data scarce areas such an approach, which requires observed streamflow data, is impossible and analyses are therefore often based on non-calibrated models, resulting in erroneous output.

The focus of the GO research project "Remotely Sensed based hydrological model calibration for basin scale water resources planning, India" is to use an innovative model calibration procedure based on Remotely Sensed evapotranspiration data. This report discusses the use of hydrological simulation models in general and specifically focuses on calibration procedures.

# 5.2 *Hydrological modelling*

### 5.2.1 Introduction

The increasing water scarcity, the growing demand for food, and the need to link those two in a sustainable way is the challenge for the next decades. Seckler et al. (1999) estimated that by 2025 cereal production will have to increase by 38% to meet world food demands. The World Water Vision, as outcome from the Second World Water Forum in The Hague in 2000, estimated a similar figure of 40% based on various projections and modeling exercises (Cosgrove and Rijsberman, 2000). These figures were more or less confirmed by projections based on an econometric model which showed that the rate of increase of grain production will be about 2% per year for the 2000-2020 period (Koyama, 1998).

To produce this increasing amount of food substantial amounts of water are required. Global estimates of water consumption per sector indicate that irrigated agriculture consumes 85% from all the withdrawals and that this consumptive use will increase by 20% in 2025 (Shiklomanov, 1998). Gleick (2000) presented estimates on the amount of water required to produce daily food diets per region. According to his figures large differences can be found between regions ranging from 1,760 liters per day per person for Sub-Saharan Africa to 5,020 for North America. Differences come from the larger number of calories consumed and the higher fraction of water-intensive meat in the diet of a North American.

This increase in food, and therefore water, requirements coincide with a growing water scarcity at an alarming rate. Recently, a study by the United Nations (UN, 1997) revealed that one-third of the world's total population of 5.7 billion lives under conditions of relative water scarcity and 450 million people are under severe water stress. This relative water scarcity and severe water scarcity are defined using the Relative Water Demand (RWD) expressed as the fraction water demand over water supply. A RWD greater then 0.2 is classified as relative water scarce, while a RWD greater then 0.4 as severe water stress. However, these values as mentioned by the UN are based on national-level totals, ignoring the fact that especially in bigger countries, huge spatial differences can occur. Vörösmarty et al. (2000) showed that including these in-country differences 1.8 billion people live in areas with sever water stress. Using their global water model and some projections for climate change, population growth and economic growth, they concluded that the number of people living in sever water stress will have grown to 2.2 billion by the year 2025.

A study published by the International Water Management Institute (Seckler et al., 1999), based on country analysis, indicated that by the year 2025 8 percent of the population of countries studied (India and China where treated separately, because of their extreme variations within the country) will have major water scarcity problems. Most countries, which contain 80% of the study population, need to increase withdrawals to meet future requirements, and only for 12% of the population no actions are required.

Although the exact numbers on how sever water stress actually is, or will be in the near future, and how much more food we should produce, differ to a certain extent, the main trend is unambiguous: more water for food and water will be scarcer.

References given before are related to the global scale, but it is very clear that at smaller scales, such as basins, extreme variations will occur and many basins with tremendous water problems can be found. This, in combination with the "think globally, act locally" principle, makes the basin the most appropriate scale to focus on.

Data is essential to assess the current conditions of water resources and to explore trends in the past. However, to explore options for the future tools are required that are able to see the impact of future trends and how we can adapt to these in the most sustainable way. Simulation models are the appropriate tools to do these analyses. R.K Linsley, a pioneer in the development of hydrologic simulation at Stanford University wrote already in 1976:
"In summary then it can be said that the answer to 'Why simulate?' is given by the following points:

1. Simulation is generally more adequate because it involves fewer approximations than conventional methods.
2. Simulation gives a more useful answer because it gives a more complete answer.
3. Simulation allows adjustment for change which conventional methods cannot do effectively.
4. Simulation costs no more than the use of reliable conventional methods (excluding empirical formulae which should not be used in any case).
5. Data for simulation is easily obtained on magnetic tape from the Climatic Data Service or the Geological Survey.
6. No more work or time is required to complete a simulation study than for a thorough hydrologic analysis with conventional methods. Often the time and cost requirements are less.
7. In any case, if the time and cost are measured against the quality and completeness of the results, simulation is far ahead of the conventional techniques.
8. Even though the available data are limited, simulation can still be useful because the data are used in a physically rational computational program."

These points are still valid nowadays and can be more or less summarized by the two main objectives where models can be used for: (i) understanding processes and (ii) scenarios analyses. Understanding processes is something that starts right from the beginning during model development. In order to build our models we must have a clear picture on how processes in the real world function and how we can mimic these in our models. The main challenge is not in trying to build in all processes we understand, which is in fact impossible, but lies in our capabilities to simplify things and concentrate on the most relevant processes of the model under construction.

The main reason for the success of models in understanding processes is that models can provide output over an unlimited times-scale, in an unlimited spatial resolution, and for difficult to observe sub-processes. These three items are the weak point in experiments, but are at the same time exactly the components in the concept of sustainable water resources management. A typical example of the application of models to understand processes is shown in Figure 10. Soil moisture profiles are shown on a daily base (high temporal resolution), at every centimeter depth (high spatial resolution) and for relatively difficult measurable processes (soil moisture movement).

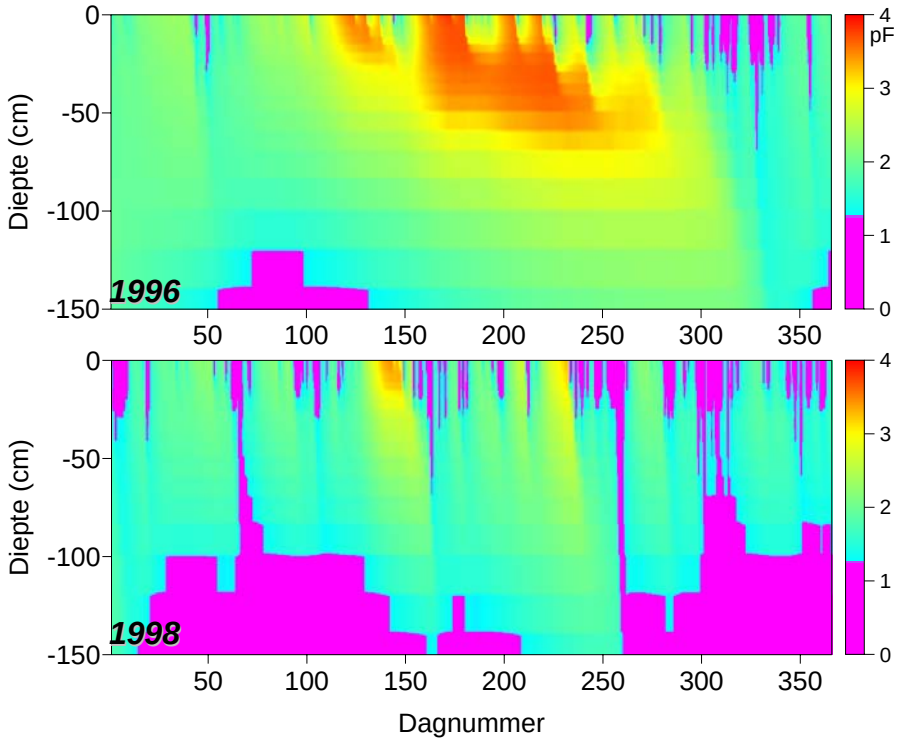


*Figure 10. Daily soil moisture profiles for a typical Dutch polder soil. (Meijer et al., 2004)*

The most important aspect of applying models however is in the use to explore different scenarios. These scenarios can refer to aspects that cannot directly be influenced, such as population growth and climate change. These are often referred to as projections. On the contrary to this are the so-called management scenarios where water managers and policy makers can make decision that will have a direct impact. Examples are changes in reservoir operations, water allocation and agricultural/irrigation practices. In other words: models enable to change focus from a re-active towards a pro-active approach. (Figure 11).

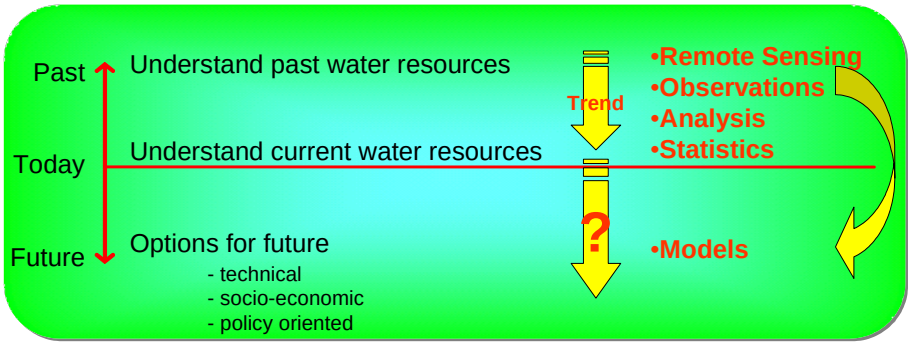


*Figure 11. The concept of using simulation models in scenario analysis.*

### 5.2.2 Concepts of modeling

The term modeling is very broad and includes everything where reality is imitated. The Webster dictionary distinguishes 13 different meanings for the word model where the following definition is most close to the one this study is focusing on: "a system of postulates, data, and inferences presented as a mathematical description of an entity or state of affairs". However we will restrict our definition here to computer models and that a model should have a certain degree of process oriented approach, excluding statistical, regression oriented models. This leads to the following definition: "a model is a computer based mathematical representation of dynamic processes".

The history of hydrological and agro-hydrological models, based on this somewhat restricted definition, is relatively short. One of the first catchment models is the so-called Stanford Watershed Model (SWM) developed by Crawford and Linsley in 1966, but the main principles are still used in nowadays catchment models to convert rainfall in runoff. SWM did not have much physics included as the catchment was just represented by a set of storage reservoirs linked to each other. The value of parameters describing the interaction between these different reservoirs was obtained by trying to optimize the simulated with the observed streamflows. At the other end of the spectrum are the field scale models describing unsaturated flow processes in the soil and root water uptake. One of the first models to be developed was the SWATR model by Feddes et al (1978) based on Richards' equation. Since, these models are based on points and use the concept that unsaturated flow is highly dominated by only vertical transport of water, much more physics could be built in from the beginning.

A huge number of hydrological models exits and applications are growing rapidly. The number of pages on the Internet including "hydrological model" is over 2.7 million (using Google on March 2006). A relevant question for hydrological model studies is therefore related to appropriate model selection. One of the most important issues to consider is the spatial scale to be incorporated in the study and how much physical detail to be included. Figure 12 illustrates the general relation between an increasing amount of physical detail and a decreasing amount of spatial detail.. The figure shows the position of commonly used models in this continuum. .

### 5.2.3 Model classification

The number of hydrological simulation models is unknown, but must be in the order of thousands. Even if we exclude the one-time models developed for a specific study and count only the more generic and more applied models it must exceed thousands. Some existing model overviews, as described later in more detail, include numerous models: IRRISOFT: 105, USBR: 100, CAMASE: 211, and REM: 675, amongst others. Interesting is that there seems to be no standard model or models emerging, as can be seen for example in groundwater modeling where ModFlow is the de-facto standard. Two hypotheses for this lack of standard can be brought forward. The first one is that model development is still in its initial phase, despite the about 25 years of history, and is therefore easy to start developing one's own model in a reasonable amount of time and effort that can compete with similar existing ones. A stimulating factor related to this is that a serious scientist is considered to have his/her own model or has at least developed one during his or her PhD studies. A second reason for the large number of models is a more fundamental one saying that hydrological processes are so complex and diverse that each case requires its specific model or set of models.

It is therefore interesting to see how models can be classified and see whether such a classification might be helpful in selecting the appropriate model given a certain question or problem to be solved. Probably the most generally used classification is the spatial scale the model deals with and the amount of physics included (Figure 12). These two characteristics determine other model behavior as data need, expected accuracy, required expertise, user-friendliness amongst others.

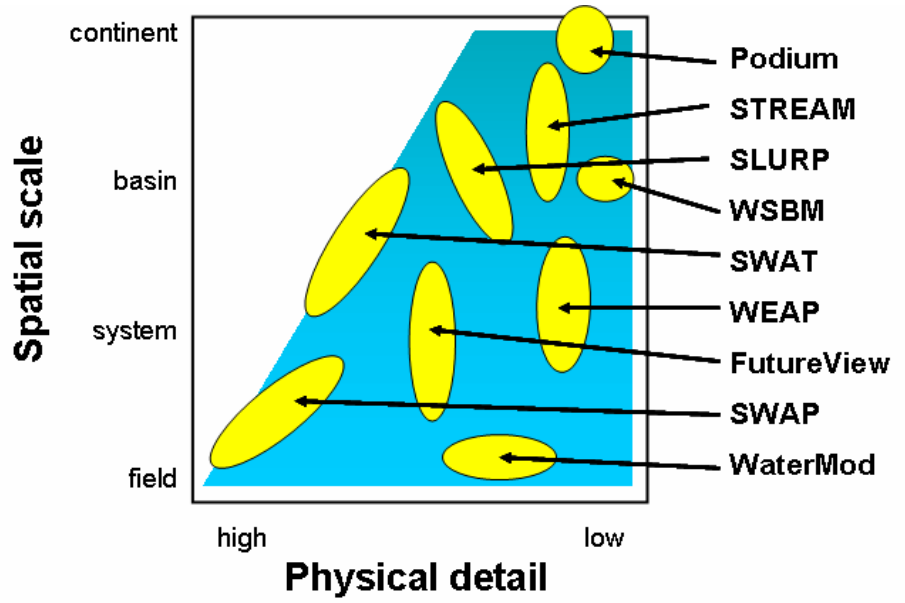


*Figure 12. Spatial and physical detail of hydrological models.*

### 5.2.4 Existing model overviews

A substantial number of overviews exist listing available models and a short summary. Most of this information is provided by the developers of the model themselves and tends therefore biased towards the capacities of the model. The most commonly used model overviews are discussed briefly here, keeping in mind that these overviews are changing rapidly, in size and number, since the Internet provides almost unlimited options to start and update such an overview in a automatic or semi-automatic way. A clear example is the Hydrologic Modeling Inventory project from the United States Bureau of Reclamation, where about 100 mainly river basin models are registered by model developers (USBR, 2002).

An overview of agro-ecosystems models is provided by a consortium named CAMASE (Concerted Action for the development and testing of quantitative Methods for research on Agricultural Systems and the Environment; CAMASE, 2005). The following types of models are distinguished: crop science, soil science, crop protection, forestry, farming systems, and land use studies, environmental science, and agricultural economics. A total of 211 models are included and for each model a nice general overview is provided. Unfortunately the last update of the register was in 1996 and advancements in model development over the last six years are not taken into account.

The United States Geological Survey (USGS, 2006) provides an overview of all their own models, about 50, divided in four categories: geochemical, ground water, surface water, water quality, and general. Some of the models are somewhat outdated, but some commonly used ones are included too. All the

models are in the public domain and can be used without restrictions. For most of the models source code is provided as well.

The United States Department of Agriculture provides also models to be used in crop-water related issues. The National Water and Climate Center of the USDA has an irrigation page (NWCC, 2006) with some water management tools related to field scale irrigation.

United States Environmental Protection Agency is very active in supporting model development. The SWAT model, originating from their research programs, might have the potential to become the de-facto standard in basin scale modeling, and has been included in the BASINS package (BASINS, 2006). More linkages to models and other model overviews are provided too (EPA, 2006).

Modeling efforts of USGS, USDA, USACE, and EPA, combined with some other models, are brought together by the USGS Surface water quality and flow Modeling Interest Group (SMIG, 2006a). SMIG has setup the most complete link to models archives nowadays including links to 40 archives (SMIG, 2006b).

The most up-to-date overview of models used crop growth modeling is the Register of Ecological Models (REM, 2006), with 675 models as per 12-Dec-2005. Besides this overview of models the same website provides general concepts and links to modeling.

### 5.2.5 Model reviews

In the previous section an overview of existing model inventories has been given. Although useful as a catalog it does not provide any independent judgment of model quality. As argued before, the best model does not exist and is a function of the application and questions to be answered. Few studies have been undertaken where a limited amount of models have been tested and reviewed. The majority of these studies focuses on two or three models that are almost similar in nature and conclusions are that models are reasonable comparable.

Texas Natural Resource Conservation Commission evaluated 19 river basin models, referred to as Water Availability Models, in order to select the most suitable model used for management of water resources, including issuing new water right permits (TNRCC, 1998). A total of 26 evaluative criteria were identified as important functions and characteristics for selecting a model that fits the need for the 23 river basins in Texas. Most importantly was the ability of the model to supports water rights simulation. During the evaluation process, each model was assessed and ranked in order of its ability to meet each criterion. The 19 models were in the first phase narrowed down to five: WRAP, MODSIM, STATEMOD, MIKE BASIN, OASIS. Models not selected included WEAP (no appropriation doctrine) and SWAT (not intuitive and user-friendly). The final conclusion was to use the WRAP model with the HEC-PREPRO GUI. As mentioned, the study focused only on models able to assist in water rights questions.

A similar study was performed to select an appropriate river basin model to be used by the Mekong River Commission (MRC, 2000). In fact, it was already decided that considering the requirements of the MRC not one single model could fulfill the needs, but three different types of model were necessary: hydrological (rainfall-runoff), basin water resources, hydrodynamic. Three main criteria

were used to select the most appropriate model: technical capability, user friendliness, and sustainability. Considering the hydrological models 11 were evaluated and the SWAT model was considered as the most suitable one. Since water quality and sediment processes were required models like SLURP were not selected. Interesting is that grid based models were not recommended as they were considered as relatively new. The selected basin simulation model was IQQM. ISIS was reviewed as the best model to be used to simulate the hydrodynamic processes.

An actual model comparison, where models are really tested using existing data, is initiated by the Hydrology Laboratory (HL) of the National Weather Service (NWS), USA. The comparison is limited to hydrological models and their ability to reproduce hydrographs, based on detailed radar rainfall data. This model comparison, referred to as DMIP (Distributed Model Intercomparison Project) has the intention to invite the academic community and other researchers to help guide the NWS's distributed modeling research by participating in a comparison of distributed models applied to test data sets. Results have been published recently, but no distinct conclusions were drawn (Reed et al., 2004).

Sing et al. (2005) evaluated the performance of two popular watershed scale simulation models HSPF and SWAT. Both models were calibrated for a nine-year period and verified using an independent 15-year period by comparing simulated and observed daily, monthly, and annual streamflow. The characteristics of simulated flows from both models were mostly similar to each other and to observed flows, particularly for the calibration results. The final conclusion was SWAT predicts flows slightly better than HSPF for the verification period, with the primary advantage being better simulation of low flows.

### 5.2.6 SWAT model

#### 5.2.6.1 Background

SWAT[2] was developed primarily by the United States Department of Agriculture (USDA) to predict the impact of land management practices on water, sediment and agricultural chemical yields in large complex watersheds with varying soils, land use and management conditions over long periods of time. The SWAT model has been extensively used, is in the public domain and can be considered as becoming the de-facto standard in spatial decision support systems.

SWAT represents all the components of the hydrological cycle including: rainfall, snow, snow-cover and snow-melt, interception storage, surface runoff, up to 10 soil storages, infiltration, evaporation, evapotranspiration, lateral flow, percolation, pond and reservoir water balances, shallow and deep aquifers, channel routing. It also includes irrigation from rivers, shallow and deep groundwater stores, ponds/reservoirs and rivers, transmission losses and irrigation onto the soil surface. It includes sediment production based on a modified version of the Universal Loss Equation and routing of sediments in river channels. SWAT tracks the movement and transformation of several forms of nitrogen and phosphorus in the watershed. It also tracks the movement and decay of pesticides. All include channel routing components and carrying of pollutants by sediments. SWAT has a modular set-up and it goes beyond the scope of this report to get into detail on each of these modules, but reference is made to the theoretical documentation (Neitsch et al, 2001).

[2] http://www.brc.tamus.edu/swat/index.html

For modelling purposes, a watershed may be partitioned into a number of sub-watersheds or sub-basins. The use of sub-basins in a simulation is particularly beneficial when different areas of the watershed are dominated by land uses or soils dissimilar enough in properties to impact hydrology. By partitioning the watershed into sub-basins, the user is able to reference different areas of the watershed to one another spatially. Input information for each sub-basin is grouped or organized into the following categories: climate; hydrologic response units or HRUs; ponds/wetlands; groundwater; and the main channel, or reach, draining the sub-basin. Hydrologic response units are lumped land areas within the sub-basin that are comprised of unique land cover, soil, and management combinations.

No matter what type of problem studied with SWAT, the water balance is the driving force behind everything that happens in the watershed. To accurately predict the movement of pesticides, sediments or nutrients, the hydrologic cycle as simulated by the model must conform to what is happening in the watershed. Simulation of the hydrology of a watershed can be separated into two major divisions. The first division is the land phase of the hydrologic cycle, depicted in Figure 13. The land phase of the hydrologic cycle controls the amount of water, sediment, nutrient and pesticide loadings to the main channel in each sub-basin.

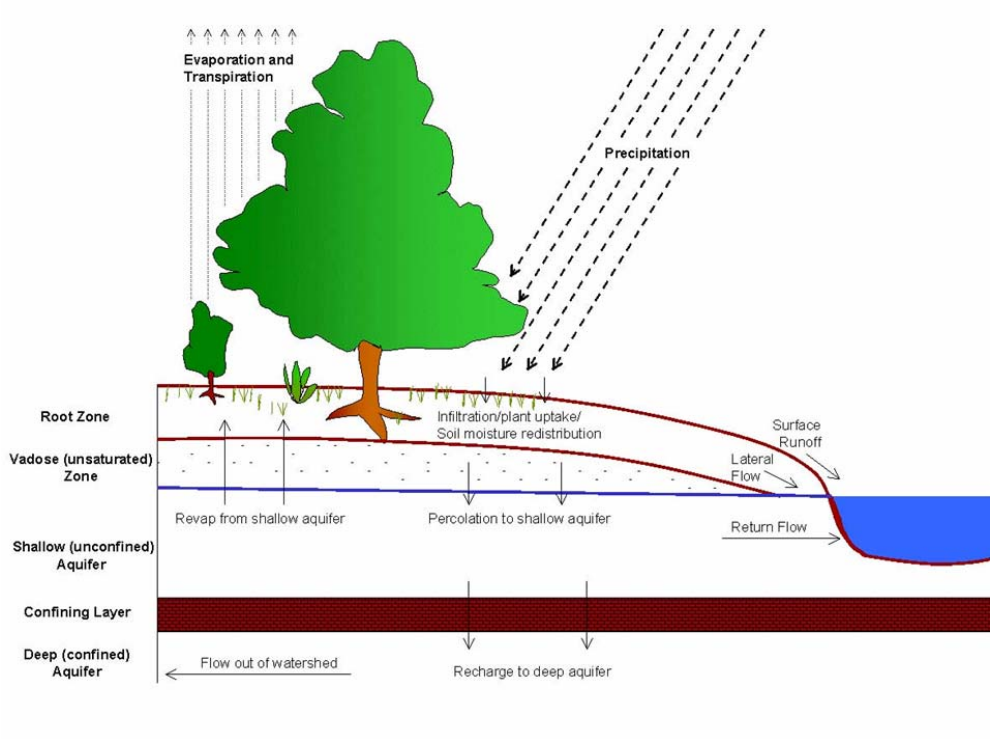


*Figure 13: Water balance SWAT.*

The second division is the water or routing phase of the hydrologic cycle which can be defined as the movement of water, sediments, etc. through the channel network of the watershed to the outlet.
Once SWAT determines the loadings of water, sediment, nutrients and pesticides to the main channel, the loadings are routed through the stream network of the watershed using a command structure. In

addition to keeping track of mass flow in the channel, SWAT models the transformation of chemicals in the stream and streambed.

#### 5.2.6.2 Evaporation

Evapotranspiration is a collective term for all processes by which water in the liquid or solid phase at or near the earth's surface becomes atmospheric water vapour. Evapotranspiration includes evaporation from rivers and lakes, bare soil, and vegetative surfaces; evaporation from within the leaves of plants (transpiration); and sublimation from ice and snow surfaces. The model computes evaporation from soils and plants separately as described by Ritchie (1972). Potential soil water evaporation is estimated as a function of potential evapotranspiration and leaf area index (area of plant leaves relative to the area of the HRU). Actual soil water evaporation is estimated by using exponential functions of soil depth and water content. Plant transpiration is simulated as a linear function of potential evapotranspiration and leaf area index. Potential evapotranspiration is the rate at which evapotranspiration would occur from a large area completely and uniformly covered with growing vegetation which has access to an unlimited supply of soil water. This rate is assumed to be unaffected by micro-climatic processes such as advection or heat-storage effects. The model offers three options for estimating potential evapotranspiration: Hargreaves (Hargreaves et al., 1985), Priestley-Taylor (Priestley and Taylor, 1972), and Penman-Monteith (Monteith, 1965).

#### 5.2.6.3 Crop growth

For each day of simulation, potential plant growth, i.e. plant growth under ideal growing conditions is calculated. Ideal growing conditions consist of adequate water and nutrient supply and a favorable climate. The biomass production functions are to a large extend similar to SEBAL; First the Absorbed Photosynthetical Radiation (APAR) is computed from intercepted solar radiation as a function of LAI, followed by a Light Use Efficiency (LUE) that is in SWAT essentially a function of carbon dioxide concentrations and vapour pressure deficits. Whilst LAI is simulated in SWAT, the fractional Photosynthetical Active Radiation (fPAR) is measured in SEBAL. The crop yield is computed as the harvestable fraction of the accumulated biomass production across the growing season.

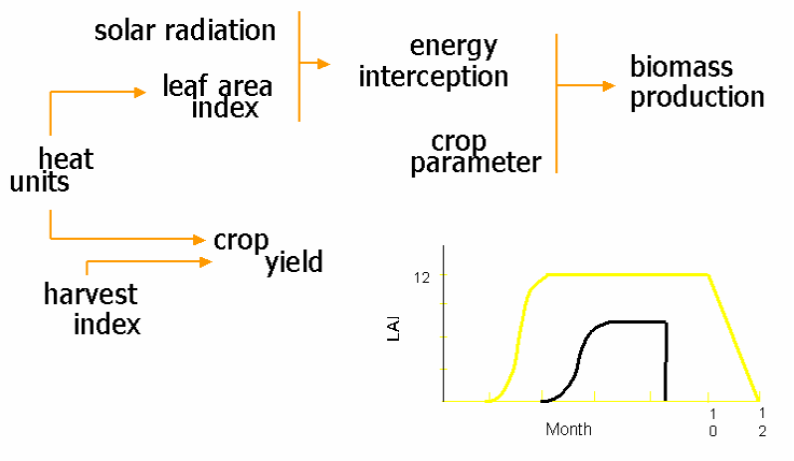


*Figure 14: Parameterization of crop production processes for estimating crop yiel*

#### 5.2.6.4 Irrigation

Irrigation may be scheduled manually or applied automatically by the model as response to a water deficit in the soil. Irrigation water applied to a sub basin is obtained from one of five types of water sources: a reach, a reservoir, a shallow aquifer, a deep aquifer, or a source outside the watershed. For this study it is assumed that all water originated from the shallow aquifer. If automatic irrigation is applied all soil layers are filled up to field capacity. If manually scheduling is used all scheduled water is applied and potential excess water percolates to the shallow aquifer. In this study irrigation water is applied automatically based on a predefined water stress criterion per sub basin. Water stress is 0.0 under optimal water conditions and approaches 1.0 as the soil water conditions vary from the optimal. Water stress is simulated by comparing actual and potential plant transpiration:

$$wstrs = 1 - \frac{E_{t,act}}{E_t} = 1 - \frac{w_{actualup}}{E_t} \qquad \text{Eq. 67}$$

where wstrs is the water stress for a given day, Et is the maximum plant transpiration on a given day (mm H2O), $E_{t,act}$ is the actual amount of transpiration on a given day (mm H2O) and $w_{actualup}$ is the total plant water uptake for the day (mm H2O). The water stress criterion is used in calibrating simulated $E_{t,act}$ with the measured SEBAL $E_{t,act}$.

#### 5.2.6.5 Groundwater

Recharge to unconfined aquifers occurs via percolation of excessively wet root zones. Recharge to confined aquifers by percolation from the surface occurs only at the upstream end of the confined aquifer, where the geologic formation containing the aquifer is exposed at the earth's surface, flow is not confined, and a water table is present. River courses and irrigation canals are connected to the groundwater system, and surface water – groundwater interactions are taken care for.

After water is infiltrated into the soil, it can basically leave again the ground as lateral flow from the upper soil layer – which mimics a 2D flow domain in the unsaturated zone – or from return flow that leaves the shallow aquifer and drains into a nearby river. The remaining part of the soil moisture can feed into the deep aquifer, from where it can be pumped back by means of artificial extraction. The total return flow thus consists of surface runoff, lateral outflow from root zone and aquifer drainage to river.

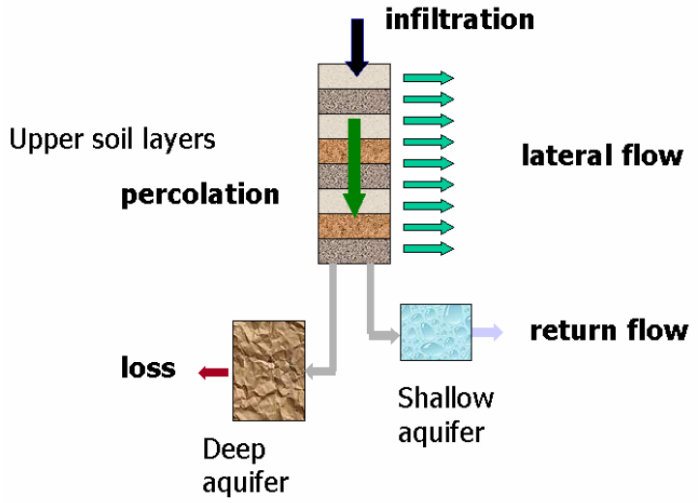

*Figure 15: Schematic diagram of the partitioning of infiltration into sub-surface water fluxes after water uptake by roots have taken place*

SWAT simulates two aquifers in each sub basin. The shallow aquifer is an unconfined aquifer that contributes to flow in the main channel or reach of the sub basin. The deep aquifer is a confined aquifer. Water that enters the deep aquifer is assumed to contribute to stream flow somewhere outside of the watershed (Arnold et al., 1993). The effects of groundwater extractions on base flow ($Q_{gw}$), defined as the contribution of the shallow aquifer to stream flow, is of specific relevance in this study.

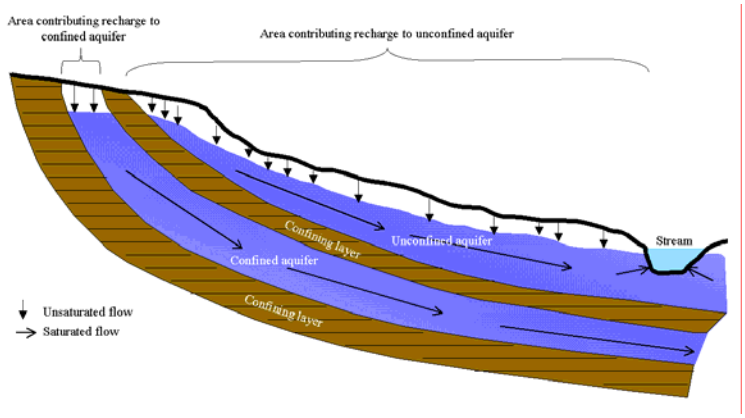


*Figure 16: Schematic representation of shallow and deep aquifers in SWAT (Neitsch et al, 2001)*

Base flow calculations are based on a combination of Hooghoudt (1940) and Smedema and Rycroft (1983) according to

$$Q_{gw,i} = Q_{gw,i-1} \cdot \exp\left[-\alpha_{gw} \cdot \Delta t\right] + w_{rchrg,sh} \cdot \left(1 - \exp\left[-\alpha_{gw} \cdot \Delta t\right]\right) \qquad \text{Eq. 68}$$

where $Q_{gw,i}$ is the groundwater flow into the main channel on day $i$ (mm $H_2O$), $Q_{gw,i-1}$ is the groundwater flow into the main channel on day $i$-1 (mm $H_2O$), $\alpha_{gw}$ is the base flow recession constant, $\Delta t$ is the time step (1 day), $w_{rchrg,sh}$ is the amount of recharge entering the shallow aquifer on day $i$ (mm $H_2O$). To enable the simulation of the effect of groundwater extractions a component was added to the model which assumes a minimal base flow defined as a percentage of the actual amount of water stored in the aquifer. For calculations of water table fluctuations a specific yield is assumed of 0.15 $m^3/m^3$ is assumed.

#### 5.2.6.6 Reservoirs

Reservoirs are located within a sub basin off the main channel. Water flowing into these water bodies must originate from the sub basin in which the water body is located. Reservoirs are located on the main channel network. They receive water from all sub basins upstream of the water body. A schematic representation of reservoirs in SWAT is shown in Figure 17.

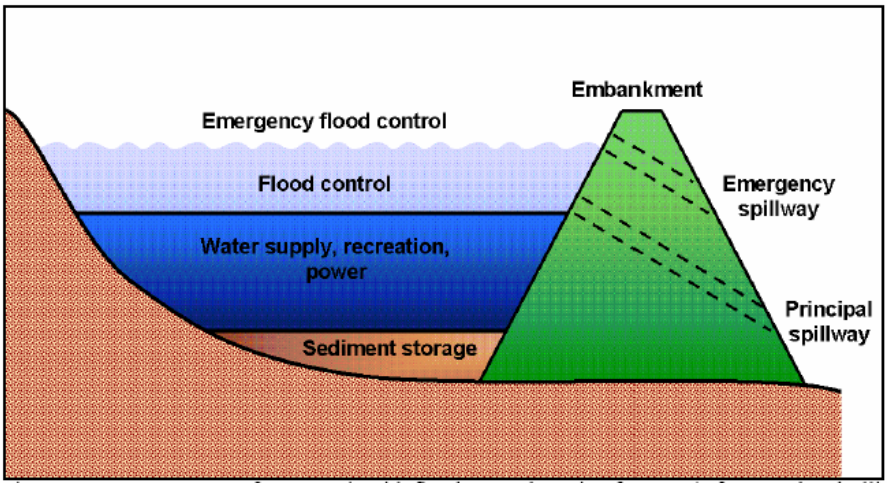


*Figure 17: Schematic representation reservoirs in SWAT (Neitsch et al, 2001)*

The water balance for reservoirs includes inflow, outflow, rainfall on the surface, evaporation, seepage from the reservoir bottom and diversions.

The model offers three alternatives for estimating outflow from the reservoir. The first option allows the user to input measured outflow. The second option, designed for small, uncontrolled reservoirs, requires the users to specify a water release rate. When the reservoir volume exceeds the principle storage, the extra water is released at the specified rate. Volume exceeding the emergency spillway is released within one day. The third option, designed for larger, managed reservoirs, has the user specify monthly target volumes for the reservoir.

## 5.3 *Calibration in hydrological modelling*

### 5.3.1 Introduction

Hydrological models use input data that have, by definition, inaccuracies. These input data or parameters must be estimated for a given catchment and for each computational segment of the model. They must be estimated either by some relationship with physical characteristics or by tuning the parameters so that model response approximates observed response, a process known as calibration.

The process of model calibration is quite complex because of limitations of the models, limitations of the input and output data, imperfect knowledge of basin characteristics, mathematical structure of the models and limitations in our ability to express quantitatively our preferences for how best to fit the models to the data. As a result of these limitations, it is even not clear that a unique set of values exists for the model parameters for a given watershed. When comparing model outputs to observations, a basic question is what causes the differences. (Duan et al., 2003)

The first paper published in the Journal of Hydrology mentioning "calibration" and "model" was published in 1973 by McCuen, although the emphasis was more on sensitivity analysis. Douglas et al. (1973) were the first to publish in the same Journal about a real calibration approach of models.

Attention drawn on calibration procedures has been growing over the last 10 years. In the 2005 issues of the Journal of Hydrology for example 41 articles were published having the word "calibration" mentioned in the abstract. One decade ago (1995) the number of articles was limited to seven.

Recently interest in using simulation models in ungauged or sparsely gauged basins has increased leading to some concerted actions. The most relevant ones are PUB (Prediction in Ungauged Basins) and MOPEX (Model Parameter Estimation Experiment)

Prediction in Ungauged Basins (PUB) refers to the prediction of streamflow, sediment and water quality variables at multiple scales, which is not based on the availability of measured data of these variables, and thus precludes "local tuning" or "calibration". On the contrary, PUB requires the development of new predictive approaches that are based on a deep "understanding" of hydrological functioning at multiple space-time scales. Indeed, PUB will herald a major change of paradigm in surface hydrology from the present one based on "calibration" to one based on "understanding".

The Model Parameter Estimation Experiment (MOPEX) project was established in 1996 with the primary goal to develop techniques for the a priori estimation of the parameters used in land surface parameterization schemes of atmospheric and hydrological models. MOPEX is an open international collaborative endeavor and has a loose group of contributors and participants. The major sponsor is the International Association of Hydrological Sciences (IAHS). So far, the major outcomes are a couple of active working meetings and publications in various journals and working papers. No real secretariat or organizational structure exists.

Calibration of hydrological models can be considered as parameter estimation or more general as optimisation. Calibration requires four dominant elements: (i) objective function, (ii) optimisation algorithm, (iii) termination criteria, (iv) calibration data (Singh and Woolhiser, 2002). Besides these four elements a fifth one can be added: (v) parameters to be optimized. These five elements will be discussed here in more detail.

### 5.3.2 Objective function

The objective function describes the difference between the observed and the simulated value. In conventional hydrological model calibration these observed and simulated values are discharges. Only few studies included other observations, such as groundwater levels and soil moisture contents, in the calibration process. Objective functions come at different flavors and the most frequently used ones will be discussed here.

DeSmedt et al. (2005) performed a flood control modeling study where four different objective functions were evaluated criteria as proposed by Hoffmann et al. (2004). The objective functions are presented in Table 1. $CR_1$ is the model bias, for which the value 0 represents a perfect simulation of the flow volume. $CR_2$ represents the model variance. $CR_3$ is the Nash-Sutcliffe coefficient for evaluating the ability of reproducing the time evolution of flows with a best value of 1. $CR_4$ is a logarithmic transformed Nash-Sutcliffe criterion, giving emphasize for evaluating the quality of low-flow simulations. $CR_5$ is an adapted version of the Nash-Sutcliffe criterion giving more weight to high discharges, and used for evaluating model efficiency for high flows.

*Table 1. Evaluation criteria for the assessment of model performance.*

| Code | Criterion | Description |
|---|---|---|
| $CR_1$ | $\sum_{i=1}^{N} Qs_i \Big/ \sum_{i=1}^{N} Qo_i - 1$ | Model bias for evaluating the ability of reproducing the water balance |
| $CR_2$ | $\sum_{i=1}^{N} \left(Qs_i - \overline{Qo}\right)^2 \Big/ \sum_{i=1}^{N} \left(Qo_i - \overline{Qo}\right)^2$ | Determination coefficient representing the model variance |
| $CR_3$ | $1 - \sum_{i=1}^{N} \left(Qs_i - Qo_i\right)^2 \Big/ \sum_{i=1}^{N} \left(Qo_i - \overline{Qo}\right)^2$ | Model efficiency for evaluating the ability of reproducing all stream-flows |
| $CR_4$ | $1 - \sum_{i=1}^{N} \left[\ln(Qs_i) - \ln(Qo_i)\right]^2 \Big/ \sum_{i=1}^{N} \left[\ln(Qo_i) - \ln\left(\overline{Qo}\right)\right]^2$ | Model efficiency for evaluating the ability of reproducing low flows |
| $CR_5$ | $1 - \sum_{i=1}^{N} \left(Qo_i + \overline{Qo}\right)\left(Qs_i - Qo_i\right)^2 \Big/ \sum_{i=1}^{N} \left(Qo_i + \overline{Qo}\right)\left(Qo_i - \overline{Qo}\right)^2$ | Model efficiency for evaluating the ability of reproducing of high flows |

with
Q : flow ($m^3\ s^{-1}$)
Qs : simulated flow ($m^3\ s^{-1}$)
Qo : observed flow ($m^3\ s^{-1}$)
N : number of observations

In practical cases, however, only one objective function is used, where the RMSE and the Nash-Sutcliffe criterion are the most commonly used ones (Lipiwattanakarn et al., 2006). The Root mean square error (RMSE) is expressed as:

$$RMSE = \left( \frac{\sum_{i}^{N} (Q_{obs,i} - Q_{sim,i})^2}{N} \right)^{1/2} \qquad \text{Eq. 69}$$

RMSE measures the average error between the observed and the simulated discharges, where $Q_{obs}$ is the observed discharge, $Q_{sim}$ is the simulated discharge and N is the number of observations. The closer the RMSE value is to zero, the better the performance of the model. The most frequently used objective function in hydrology is the efficiency index or Nash-Sutcliffe criterion:

$$EI = 1 - \left( \frac{\sum_{i=1}^{N} (Q_{obs,i} - Q_{sim,i})^2}{\sum_{i=1}^{N} (Q_{obs,i} - \overline{Q}_{obs})^2} \right) \qquad \text{Eq. 70}$$

The Nash-Sutcliffe criterion value is in the range of [-∞, 1]. The zero value means the model performs equal to a naive prediction, that is, a prediction using an average observed value. The value less than zero means the model performs worse than the average observed value. A value between 0.6-0.8 is moderate to good. A value more than 0.8 is a good fit. A value of one is a perfect fit.

Most of these objective functions consider only discharge data as calibration factor. If more than one data source will be used, a combined objective function has to be used. Madsen and Jacobsen (2001) calibrated the MIKE-SHE model using groundwater as well as flow data, based on the following combined RMSE approach:

$$F_h(\theta) = \frac{1}{M}\sum_{j=1}^{M}\sqrt{\frac{1}{n_i}\sum_{i=1}^{n_i}\left[h_{obs,i,j} - h_{i,j}(\theta)\right]^2} \quad \text{Eq. 71}$$

$$F_q(\theta) = \sqrt{\frac{1}{n}\sum_{i=1}^{n}\left[q_{obs,i,j} - q_{i,j}(\theta)\right]^2} \quad \text{Eq. 72}$$

$$F_{agg}(\theta) = w_h F_h(\theta) + w_q F_q(\theta) \quad \text{Eq. 73}$$

where:
$F(\theta)$ an objective function that measures the goodness-of-fit of the simulated model with respect to the parameter set $\theta$.
h: groundwater levels
M: total number of groundwater locations
n: total number of observations at one groundwater location
q: runoff at the catchment outlet
$w_h$ : weight assigned to groundwater level data
$w_q$ : weight assigned to runoff data

The first equation is the average root mean squared error (RMSE) of the groundwater levels ($h$) at $M$ locations, and the second equation is the RMSE of the discharge (q). The weighted average measure is given by the last equation.

Selection of the appropriate objective function is critical for a successful optimization, but the best objective function is problem dependent. Many research papers have been published to compare different objective functions all with different conclusions. Some examples:

- Rao and Han (1987) analysed several objective functions in calibrating the urban watershed runoff model and found the least-squares criterion to be the best.
- Servat and Dezetter(1991) employed five different objective functions for calibrating a rainfall-runoff model on a Sudanese savannah area in the Ivory Coast and found the Nash-Sutcliffe efficiency to be the best.

### 5.3.3 Optimization algorithm

Although optimization is in principle quite straightforward, e.g. minimizing the objective function, in real life the problem is very complex as many objective functions have multiple extremes (minima).

In general, optimization algorithms can be categorized as "local" and "global" search methods (Sorooshian and Gupta, 1995). Depending on the hill climbing strategy employed, local search algorithms may be further divided into "direct" and "gradient-based" methods. Direct search methods use only information on the objective function value, whereas gradient-based methods also use information about the gradient of the objective function. Local search methods are efficient for locating the optimum of a uni-modal function since in this case the hill climbing search will eventually reach the

global optimum, irrespective of the starting point. Interesting is that in groundwater modelling, parameter estimation has mainly been based on local gradient-based search techniques (e.g. McLaughlin and Townley, 1996).

In practice, hydrological simulation models have numerous local optima on the objective function surface, and in such cases local search methods are less effective because the estimated optimum will depend on the starting point of the search. For such multi-modal objective functions global search methods are more effective, where the term "global" refers to algorithms that are especially designed for locating the global optimum and not being trapped in local optima. Popular global search methods are the so-called population-evolution-based search strategies such as the shuffled complex evolution (SCE) algorithm (Duan et al., 1992) and genetic algorithms (GA) (Wang, 1991).

In summary five classes of optimization algorithms can be distinguished: (i) direct search methods, (ii) gradient search methods, (iii) random search methods, (iv) multistart algorithms, and (v) shuffled complex algorithms (Sorooshian and Gupta, 1995). The first two can be considered as local search methods and the latter three as global search methods.

In terms of global optimisation techniques Solomatine (1998) distinguished the following five groups:

- set (space) covering techniques;
- random search methods;
- evolutionary and genetic algorithms (can be attributed to random search methods);
- methods based on multiple local searches (multistart) using clustering;
- other methods (simulated annealing, trajectory techniques, tunneling approach, analysis methods based on a stochastic model of the objective function).

For calibration of lumped, conceptual hydrological catchment models a large number of studies have been conducted that compare different automatic algorithms (e.g. Duan et al., 1992; Gan and Biftu, 1996; Cooper et al., 1997; Kuzcera, 1997; Franchini et al., 1998; Thyer et al., 1999). The main conclusion from these studies is that the global population-evolution based algorithms are more effective than multi-start local search procedures, which in turn perform better than pure local search methods.

Global search procedures has been applied in steady state groundwater modelling (Heidari and Ranjithan, 1998; Solomatine et al., 1999), but to the authors' knowledge no attempt has yet been made to apply these techniques for calibration of integrated and distributed catchment models.

Singh and Woolhiser (2002) stated that the shuffled complex evolution global optimisation algorithm has been found to be consistent, effective, and efficient in locating the globally optimum hydrologic model parameters.

Recently SWAT was used to evaluate several the optimization algorithms: Shuffled Complex Evolution (SCE), real-valued simple Genetic Algorithm (GA), multi-start Simplex and Monte Carlo Sampling (MCS) and a new algorithm called the Global Greedy Search (GGS) algorithm (Tolson and Schoemaker, 2006). All algorithms used in this study were coded in Matlab and compared at default or recommended algorithm parameter settings. For the two case studies a maximum of 2500 (6 parameters) respectively 6000 (14 parameters) SWAT model evaluations were used. Results indicated, similar as in

the majority of previous studies, that the SCE algorithm outperformed the Simplex, GA and MCS algorithms.

One of the major conclusions of research on optimization is somewhat disappointing: there is no best algorithm. One algorithm can be very good on one problem and show poor performance on another problem and/or vice versa. Solomatine (1998; 1999) defined three performance indicators that can be used to evaluate the algorithm for a specific problem:

- effectiveness: how close the algorithm gets to the global minimum;
- efficiency: running time of an algorithm measured by the number of function evaluations needed (the running time of the algorithm itself is negligible compared with the former);
- reliability: robustness of the algorithms can be measured by the number of successes in finding the global minimum, or at least approaching it sufficiently closely.

The book published by Duan et al. (2003) on calibration of watershed models came to the clear conclusion that the Shuffled Complex Evolution (SCE) can be considered as the de-facto standard optimization algorithm.

A detailed description of the method appears in Duan et al. (1992). In summary the algorithm has five distinct steps:

1. A "population" of points is selected randomly from the feasible parameter space.
2. The population is partitioned into several complexes, each with $2n + 1$ points, where $n$ is the number of parameters to be optimized.
3. Each complex is evolved independently based on the downhill simplex method.
4. The population is periodically shuffled to share information, and new complexes are formed.
5. Evolution and shuffling are repeated until the specified convergence criteria are satisfied.

Conclusions from most recent studies that the SCE algorithm outperforms other ones should be taken into consideration that these conclusions are mainly based on optimization on flows, while the focus of our study is on calibration using evapotranspiration. Also Skahill and Doherty (2006) recently showed the advantages of the more traditional Gauss–Marquardt–Levenberg (GML) algorithm over the global search ones.

### 5.3.4 Termination criteria

Termination criteria are needed to determine when to stop the iterative search. Methods that have been used include (i) function convergence, (ii) parameter convergence, or (iii) a maximum number of iterations (Hogue et al., 2000) When an algorithm is unable to appreciably change parameter values and improve the objective function value, parameter convergence is achieved. Function convergence occurs when the algorithm is unable to improve the objective function beyond a predefined increment in one or more iterations. A calibrator also may set a maximum number of iterations to stop the search procedure, ensuring that the algorithm does not enter an endless loop.

One simple way to terminate the search is to stop when the algorithm is unable to appreciably improve the value of the function over one or more iterations (**function convergence**). While this can indicate arrival at the location of an optimum, it could also mean only that a very flat region of the response surface has been reached. If precise detection of an optimum is not considered as important, then

function convergence can be a very useful termination criterion. One typical implementation of this criterion is to stop when:

$$\frac{f_i - f_{i-1}}{f_i} \leq Err_f \qquad \text{Eq. 74}$$

where $f_{i-1}$ and $f_i$ are the function values at the $(i-1)^{th}$ and $i^{th}$ steps, respectively, and $Err_f$ is the function convergence criterion (for example $Err_f = 10^{-3}$).

Another way to terminate the search is to stop when the algorithm is unable to appreciably change the parameter values and simultaneously improve the function value over one or more iterations (**parameter convergence**). While this can indicate arrival at an optimum, it could also mean only that a region of high parameter interaction (long narrow valley) on the response surface has been reached. One typical implementation of this criterion is to stop when:

$$\frac{\theta(j)_{i-1} - \theta(j)_i}{\theta(j)_{\max} - \theta(j)_{\min}} \leq Err_\theta \qquad \text{Eq. 75}$$

where $\theta(j)_{i-1}$ and $\theta(j)_i$ are the values of the $j^{th}$ parameter at the $(i-1)^{th}$ and $i^{th}$ steps, respectively, and $Err_\theta$ is the parameter convergence criterion (for example $Err_\theta = 10^{-3}$).

If computer time is limited, and to ensure that the algorithm does not somehow enter an infinite loop, it is normal to terminate the search if a prespecified maximum number of iterations is exceeded, unless the parameter or function convergence criteria are met first (maximum number of iterations). For random search methods, this is the normal way to terminate the search. It is not really possible to give guidelines on the value for this criterion, because it is both algorithm- and problem – dependent. The maximum iterations criterion is used as a backup to prevent waste of computer time.

None of these termination criteria guaranty that the search arrival at the global optimum, except in the most trivial cases where the function is convex and well behaved. These criteria can be used in the same program, so the search will terminate when one of the three criterion is reached (Xu, 2002).

### 5.3.5 Calibration data

It is common practice to use observed discharge data to calibrate hydrological models. In some cases, especially if groundwater models are considered, hydraulic heads in aquifer systems are used. As discussed previously, this may lead to models able to generate runoff accurately even if processes are not well described by model and model parameters. It is therefore erroneous to use models calibrated on discharge data to evaluate other (land) processes, or undertake scenario analysis. The objective of this study is therefore to explore the use of evapotranspiration data as alternative for calibration purposes.

The number of data to apply in a calibration procedure is somewhat less studied. It has been a common practice to use as much data as were available for the calibration, after setting aside part of the data set for verification of the results. However, studies by Sorooshian et al (1983) and Xu and Vandewiele (1994) indicated that the use of longer data sets than what is necessary served only to marginally improve the parameter estimates. In general, from a statistical point of view, the data set used should be at least 20 times the number of parameters to be estimated (for example, if there are

10 parameters, then at least 200 observed data points should be used for computing the function). This is of course an approximate rule of thumb. Gupta and Sorooshian (1985) showed that the standard error (σ) of the estimate of parameter (j) decreases with sample size n approximately according to the formula:

$$\sigma(j) \approx \frac{1}{\sqrt{n}} \qquad \text{Eq. 76}$$

Because the marginal improvement in $1/\sqrt{n}$ becomes small after 500 to 1000 data points, this suggests that two to three years of calibration data should be sufficient for a daily model with not more than 10 parameters, provided the data are of good quality.

### 5.3.6 Parameters to be optimized

The number of parameter to be estimated and which parameters to include in the calibration processes depends on many factors, such as: model considered, observation parameters and number, optimization algorithm, and objectives of the study. Appropriate parameter sensitivity should be done prior to any calibration. Some suggestions specific to SWAT are provided in the SWAT manual:

- ESCO: Soil evaporation compensation factor
- CN2: Curve number that controls runoff according to the American SCS method
- REVAP: Groundwater revap coefficient.
- SHALLST: Threshold depth of water in the shallow aquifer.
- ALPHA_BF: Baseflow alpha factor.

Tolson and Schoemaker (2006) calibrated SWAT using several optimization algorithms: Shuffled Complex Evolution (SCE), real-valued simple Genetic Algorithm (GA), multi-start Simplex and Monte Carlo Sampling (MCS) and a new algorithm called the Global Greedy Search (GGS) algorithm. For two case studies 6 parameters respectively 14 parameters were used (Table 2).

*Table 2. Parameters used to calibrate the SWAT model (in brackets name of the input file).*

| |
|---|
| **Case 1 (6 parameters)** |
| SMTMP (.bsn), Snow melt base temperature (ºC) |
| SURLAG (.bsn), Surface runoff lag coefficient |
| GW_DELAY (.gw), Groundwater delay time (days) |
| ALPHA_BF (.gw), Baseflow alpha factor (days) |
| BIO_E (crop.dat), Radiation-use efficiency ((kg/ha)/(MJ/m2)) |
| BLAI (crop.dat), Maximum potential leaf area index |
| **Case 2 (14 parameters)** |
| TIMP (.bsn), Snow pack temperature lag factor |
| SURLAG (.bsn), Surface runoff lag coefficient |
| APM (.bsn), Peak rate factor for subbasin sediment routing |
| PRF (.bsn), Peak rate factor for main channel sediment routing |
| SPCON (.bsn), Linear channel sediment reentrainment factor |
| SPEXP (.bsn), Exponent channel sediment reentrainment factor |
| GW_DELAY (.gw), Groundwater delay time (days) |
| ALPHA_BF (.gw), Baseflow alpha factor (days) |

| |
|---|
| BIOMIX (.mgt) A, Biological mixing efficiency |
| CN2 (.mgt) A, SCS runoff curve number for moisture condition II |
| AWC_f (.sol) A & B, Available water capacity factor |
| SOL_K_f (.sol) A & C, Saturated hydraulic conductivity |
| T_OPT (crop.dat), Optimal temperature for plant growth (ºC) |
| T_BASE (crop.dat), Minimum temperature for plant growth (ºC) |

Bastiaanssen et al. (2006) applied the SWAT model for the Rio Bravo basin in Mexico and performed a simple calibration using the following parameters as shown in Table 3.

*Table 3. Parameters used to calibrate the SWAT model (in brackets name of the input file).*

| |
|---|
| SOL_Z (.sol), Depth from soil surface to bottom of layer (mm) |
| SOL_AWC (.sol), Available water capacity of the soil layer (mm H2O/mm soil) |
| GW_REVAP (.gw), Groundwater "revap" coefficient |
| RFINC(.sub), Rainfall adjustment (% change) |

### 5.3.7 Calibration tools

#### 5.3.7.1 PEST

PEST is a nonlinear parameter estimation package that can be used to estimate parameters for just about any existing computer model, whether or not a user has access to the model's source code. PEST is able to "take control" of a model, running it as many times as it needs to while adjusting its parameters until the discrepancies between selected model outputs and a complementary set of field or laboratory measurements is reduced to a minimum in the weighted least squares sense.

The Gauss-Marquardt-Levenberg algorithm is used by PEST to optimize the model. For linear models (ie. models for which observations are calculated from parameters through a matrix equation with constant parameter coefficients), optimisation can be achieved in one step. However for nonlinear problems (most models fall into this category), parameter estimation is an iterative process. At the beginning of each iteration the relationship between model parameters and model-generated observations is linearised by formulating it as a Taylor expansion about the currently best parameter set; hence the derivatives of all observations with respect to all parameters must be calculated. This linearised problem is then solved for a better parameter set, and the new parameters tested by running the model again. By comparing parameter changes and objective function improvement achieved through the current iteration with those achieved in previous iterations.

Derivatives of observations with respect to parameters are calculated using finite differences. During every optimisation iteration the model is run once for each adjustable parameter, a small user-supplied increment being added to the parameter value prior to the run. The resulting observation changes are divided by this increment in order to calculate their derivatives with respect to the parameter. This is repeated for each parameter. This technique of derivatives calculation is referred to as the method of "forward differences".

Derivatives calculated in this way are only approximate. If the increment is too large the approximation will be poor; if the increment is too small roundoff errors will detract from derivatives accuracy. Both of these effects will degrade optimisation performance. To combat the problem of derivatives inaccuracy,

PEST allows derivatives to be calculated using the method of "central differences". Using this method, two model runs are required to calculate a set of observation derivatives with respect to any parameter. For the first run an increment is added to the current parameter value, while for the second run the increment is subtracted. Hence three observation-parameter pairs are used in the calculation of any derivative (the third pair being the current parameter value and corresponding observation value). The derivative is calculated either by (i) fitting a parabola to all three points, (ii) constructing a best-fit straight line for the three points or (iii) by simply using finite differences on the outer two points.

PEST is very flexible and is becoming the de-facto standard in groundwater modeling. However, one of the most relevant restrictions is the use of the Gauss-Marquardt-Levenberg algorithm, a gradient based method, sensitive to local minima.

#### 5.3.7.2 UCODE

UCODE_2005 can be used with existing process models to perform sensitivity analysis, data needs assessment, calibration, prediction, and uncertainty analysis. Any process model or set of models can be used; the only requirements are that models have numerical (ASCII or text only) input and output files, that the numbers in these files have sufficient significant digits, that all required models can be run from a single batch file or script, and that simulated values are continuous functions of the parameter values. An estimated parameter can be a quantity that appears in the input files of the process model(s), or a quantity used in an equation that produces a value that appears in the input files. In the latter situation, the equation is user-defined.

UCODE_2005 can compare observations and simulated equivalents. The simulated equivalents can be any simulated value written in the process-model output files or can be calculated from simulated values with user-defined equations. The quantities can be model results, or dependent variables. For example, for ground-water models they can be heads, flows, concentrations, and so on. Prior, or direct, information on estimated parameters also can be considered. Statistics are calculated to quantify the comparison of observations and simulated equivalents, including a weighted least-squares objective function. In addition, data-exchange files are produced that facilitate graphical analysis.

UCODE_2005 can be used in model calibration through its sensitivity analysis capabilities and its ability to estimate parameter values that result in the best possible fit to the observations. Parameters are estimated using nonlinear regression: a weighted least-squares objective function is minimized with respect to the parameter values using a modified Gauss-Newton method or a double-dogleg technique. Sensitivities needed for the method can be read from files produced by process models that can calculate sensitivities, such as MODFLOW-2000, or can be calculated by UCODE_2005 using a more general, but less accurate, forward- or central-difference perturbation technique. Statistics are calculated and printed for use in (1) diagnosing inadequate data and identifying parameters that probably cannot be estimated; (2) evaluating estimated parameter values; and (3) evaluating how well the model represents the simulated processes.

One of the disadvantages of UCODE_2005 is the use of Gauss-Newton as optimization algorithm, which is a gradient based one. For non-linear problems this might lead to finding local minima rather than global ones. However, Skahill and Doherty (2006) argued the advantages of the more traditional

Gauss–Marquardt–Levenberg (GML) algorithm over the global search ones. In summary: model-run efficiency, report useful information on parameter sensitivities and covariances, easily adaptable.

More information on UCODE can be found at: http://www.mines.edu/igwmc/freeware/ucode/

#### 5.3.7.3 MATLAB

Matlab can be considered as the de-facto standard for scientific high-level technical computing and interactive environment for algorithm development, data visualization, data analysis, and numeric computation. MATLAB is used in a wide range of applications, including signal and image processing, communications, control design, test and measurement, financial modeling and analysis, and computational biology. Add-on toolboxes (collections of special-purpose MATLAB functions, available separately) extend the MATLAB environment to solve particular classes of problems in these application areas.

One of the Toolboxes relevant to this study is the Model-Based Calibration Toolbox. Models are available that can be incorperated directly within this toolbox. One of the examples of this is the Shuffled Complex Evolution (SCE-UA) global optimization algorithm, that is provided by the authors and can be downloaded free of charge (http://www.mathworks.com/matlabcentral/fileexchange/loadFile.do?objectId=7671&objectType=file).

#### 5.3.7.4 GLOBE

GLOBE is an optimization tool that can find the minimum a function of multiple variables which value is given by an external program or a dynamic-link library (DLL). It is possible to impose box constraints (bounds) on the variables' values. No special properties of the function are assumed. GLOBE implements the "global" minimization. There are seven (with variations – nine) algorithms implemented that the user can tune to the problem and that can be run in a batch for the same function. GLOBE includes advanced visualization features.

The following algorithms are currently implemented in GLOBE:

- Controlled random search (CRS) (Price, 1983)
- Genetic Algorithm (GA)
- Adaptive cluster covering (ACCO/ACCOL) (Solomatine, 1995)
- Multis (a version of Powell-Brent non-derivative algorithm, with multiple randomized starts)
- M-Simplex (a version of the simplex decent algorithm of Nelder and Mead, with randomized multiple starts)
- Improved Controlled random search (CRS4a) (based on Ali, Storey, 1994)
- Adaptive cluster descent (ACD) (Solomatine, 1999)

Details about the GLOBE program can be found at: http://www.unesco-ihe.org/hi/sol/global.htm

## 5.4 Conclusions

The key features of the GO research project "Remotely Sensed based hydrological model calibration for basin scale water resources planning, India" is that calibration will be based on remote sensed based ET observations rather than on discharges. In this context the following conclusions can be drawn:

- Selection of the appropriate **model** is essential where a balance has to be made between issues as: scale, physical detail, support, availability of source code, expertise, and option of linking the model with remote sensed based ET. The SWAT model offers the best opportunities in this regard.
- There appears to be a general consensus that the appropriate **objective function** for discharge based calibration is the Nash-Sutcliffe one. However, whether this is also the case for ET calibration is questionable and should be evaluated during this study.
- For most calibration studies the global **optimization algorithms** outperformed the local ones. Most studies indicated that the Shuffled Complex Evolution (SCE) algorithm performed best. Since these conclusions are based on discharge calibration it is not clear whether this holds for this study as well. It is therefore required to test several optimization algorithms.
- The **tool** to be used should therefore include more algorithms that can be all applied in one generic step. The selection of GLOBE or MATLAB might be therefore preferable. However, given the complexity of the problem and the innovative aspects of using ET as calibration data, and the uncertainaty in parameter selection, a start with a more direct search algorithm is preferable. The PEST program is therefore the best selection.

# 6 Remote Sensing and hydrological modelling ofthe Upper Bhima catchment

## 6.1 Introduction

This report describes the integration of hydrological modelling and Remote Sensing in the Upper Bhima catchment. The results of this integration, which is the core of the project, are primarily reported in two scientific papers:

- The first paper titled "Spatial calibration of a distributed hydrological model using Remote Sensing derived evapotranspiration in the Upper Bhima catchment, India" is submitted to the internationally scientific journal *Hydrological Processes.* This paper is a methodological paper and focuses on (i) deriving hydrological fluxes by Remote Sensing, (ii) optimisation algorithms used in calibration of simulation models, (iii) equifinality in parameter optimisation, (iv) use of Remote Sensing in parameterisation of hydrological models and (v) the use of Remote Sensing in the calibration of hydrological models in data scarce areas. The paper is attached as Annex 1.
- The second paper titled "Evaluating water use and productivity in the upper Bhima catchment by integrating remote sensing and a process based hydrological model" is submitted to the international scientific journal *Agricultural Water Management*. This paper focuses on how the approach can actually be applied to evaluate potential for possible water savings. This paper is attached as Annex 2.

Setting up a hydrological model, based on Remote Sensing, involves many more steps worth reporting than what has been captured in the scientific papers. This research report is intended to provide a complete and detailed overview of the modelling approach. The method for land use classification, evapotranspiration and precipitation mapping are discussed in detail. The final chapter describes how this all comes together in the model set-up.

## 6.2 Land use classification

### 6.2.1 Introduction

Based on a study for the entire Krishna basin a land use map was available at the start of the project. This land use map (Figure 18) was derived from a temporal series of MODIS[3] Normalized Difference Vegetation Index (NDVI) data. The first results of the evaporation mapping revealed however that the land use map was not accurate enough, specifically in the irrigated areas and the forested areas in the Western Ghats. The Upper Bhima sub-basin has a number of specific characteristics which caused errors in the land use classification.

[3] http://modis.gsfc.nasa.gov/

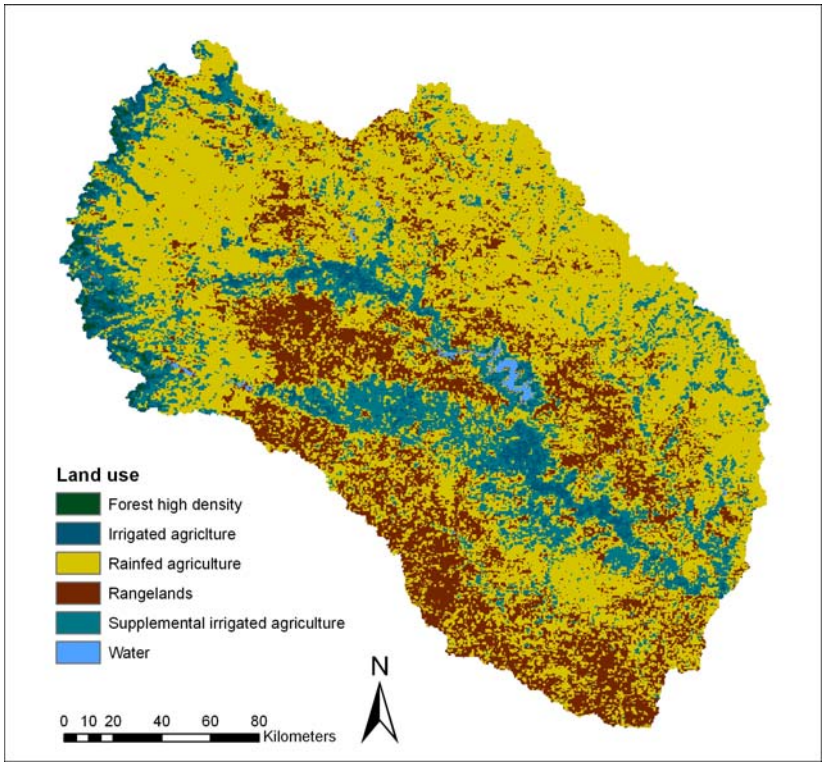


*Figure 18 Land use map based on Krishna basin classification*

First of all the acreage of irrigated agriculture seems to be underestimated. The command areas of the Khadakwasla, Ujani and Yadgaon and Bhatghar reservoirs are mainly cultivated with sugarcane. Sugar cane is a C4 crop, produces large amounts of biomass with yields up 70 t/ha. The growing season of sugarcane has length of 11 months and sugar cane can thus be grown year around. These unique properties might have led to an inaccurate representation of the sugarcane areas. Secondly there seems to be large areas in and around the Western Ghats which are classified as rain fed agriculture but in practice they should be classified as low density forests.

Because of these errors a new land use classification has been performed for the Upper Bhima sub basin. This chapter describes the methodology used and the results of the land use classification.

### 6.2.2 Remote Sensing and land use classification

The application of Remote Sensing is a common technique in land use and land cover (LULC) mapping. Traditionally multi-spectral data are used to classify pixels in the image as a certain LULC unit. The basic assumption being that each LULC unit exhibits unique spectral behaviour. A LULC has unique reflectance and emittance properties at different location along the electromagnetic spectrum. This is illustrated in Figure 19. It shows the spectra of water, bare soil and vegetation and the bands of the Landsat TM satellite. The combination of digital numbers (DN) for each band for each pixel allows the classification of the pixel to a certain land use class. This technique is summarized as spectral pattern recognition.

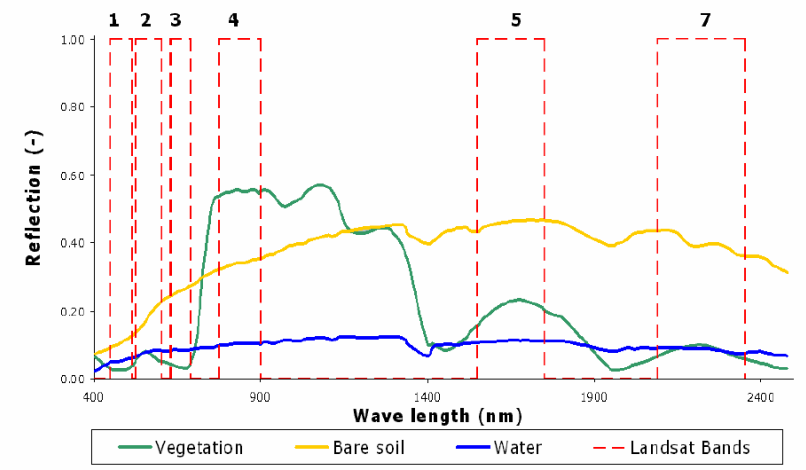


*Figure 19: Spectral behaviour of major land uses and the spectral bands of the Landsat satellite*

Multi-spectral image classification is usually performed using one or a limited number of images. In agricultural areas however there may be distinct spectral and spatial changes during the growing season which necessitates the use of multi-temporal imagery. A single image at the onset of the growing would prohibit the distinction between bare soil and a crop. Problems may also arise when dual-cropping patterns are prevalent. Winter wheat in fall may show a similar spectrum as a pasture in spring. If imagery of multiple dates are used the chances on erroneous classifications are much less (Immerzeel and Droogers, 2005, Bastiaanssen *et al.*, 2006)

There is a distinction between supervised and unsupervised classification techniques (Lillesand and Kiefer, 2000).

In a supervised classification the spectral signatures of training areas with known LULC are specified to the classification algorithm. After the training stage the actual classification process can take place. During the classification process each pixel is compared to the specified spectral signatures and labelled to the corresponding LULC class. There are four popular classification methods which are commonly used:

- The Box classifier method
- The Minimum Distance classifier
- The Minimum Mahalanobis Distance classifier
- The Maximum Likelihood classifier

The Box classifier method is based on the distances towards class means and the standard deviation per band of each class. Multi-dimensional boxes are drawn around class means based on the standard deviation of each class. The user can insert a multiplication factor (usually > 1) to make all boxes a bit wider. If the spectral values of a pixel to be classified fall inside a box, then that class name is assigned. If the spectral values of a pixel fall within two boxes, the class name of the box with the standard deviation is assigned. If the spectral values of a pixel do not fall within a box, the undefined value is assigned. The default multiplication factor is the square root of √3 for 3 bands.

The Minimum Distance classifier is based on the Euclidean distances towards class means only. For the spectral values of a pixel to be classified, the distances towards the class means are calculated. If the

shortest (Euclidean) distance to a class mean is smaller than the user-defined threshold, then this class name is assigned to the output pixel. Else the undefined value is assigned.

For the spectral values of a pixel to be classified with the Minimum Mahalanobis Distance classifier, the distances towards the class means are calculated as Mahalanobis distance, which depends on the distances towards class means and the variance-covariance matrix of each class. The class name with the shortest Mahalanobis distance is assigned, if this distance is smaller than the user-defined threshold value. Else, the undefined value is assigned.

The Maximum Likelihood classification assumes that spectral values of training pixels are statistically distributed according to a multi-variate normal probability density function. For each set of spectral input values, the distance is calculated towards each of the classes is calculated using Mahalanobis distance. Another factor is added to compensate for within class variability. The class name with the shortest distance is assigned, if this distance is smaller than the user-defined threshold value. Else, the undefined value is assigned.

In an unsupervised classification the image data are first of classified by aggregating them into spatial clusters based on the statistical properties of the pixel values (e.g. average and variation). The number of clusters is usually chosen larger then the actual number of LULC classes which are expected. After the clustering the LULC identity is assigned to each land use class based on ground reference data, which is usually not an easy task. In case of the unsupervised classification the classification step is followed by the training step. The clusters are natural groupings of pixels with similar spectral behaviour. There are numerous clustering algorithms that can determine these natural groupings. One common form of clustering is called the K-means approach. The user identifies the number of clusters to be located in the image. The algorithm then randomly locates the number of specified cluster centres in the multidimensional feature space. Each pixel is then assigned to the cluster whose arbitrary mean vector is closest. After all pixels are classified revised mean vectors for each cluster is calculated and the process is iteratively repeated until no significant changes in the location of the mean vectors occur. The convergence criterion used to stop the iteration is specified by the user.
Other commonly used methods are based on textural information of the image. They use information from neighbouring pixels to assign classes to pixels and are referred to as contextual classifiers.

Spectral rationing is another important technique that can support image classifications. It refers to an enhancement technique by combining pixel values from different bands. The most commonly used ratio techniques are ratios to enhance the vegetation cover such as the Normalized Difference Vegetation Index (NDVI). The NDVI is defined as:

$$NDVI = \frac{NIR - RED}{NIR + RED} \qquad \text{Eq. 77}$$

Where NIR is the reflectance in the near infra-red part of the spectrum (wavelength = 0.7-1.1 µm) and RED is the reflectance in the red part of the spectrum (wavelength = 0.6-0.7 µm). Healthy vegetation free of environmental stress reflects well in the NIR part of the spectrum and reflects poorly in the red part of the spectrum. The NDVI amplifies this effect.

In this study a combination of spectral rationing and multi-temporal unsupervised classification is applied to make a land use classification of the Upper Bhima sub basin. A time series of 16 NDVI images acquired with the Moderate Resolution Imaging Spectroradiometer (MODIS) is used to perform an unsupervised classification.

### 6.2.3 MODIS[4]

MODIS is a key instrument aboard the Terra (EOS AM) and Aqua (EOS PM) satellites. Terra's orbit around the Earth is timed so that it passes from north to south across the equator in the morning, while Aqua passes south to north over the equator in the afternoon. Terra was launched on December 18 1999 and Aqua was launched on May 4 2002. These data will improve the understanding of global dynamics and processes occurring on the land, in the oceans, and in the lower atmosphere. MODIS is playing a vital role in the development of validated, global, interactive Earth system models able to predict global change accurately enough to assist policy makers in making sound decisions concerning the protection of our environment.

The MODIS instrument provides high radiometric sensitivity (12 bit) in 36 spectral bands ranging in wavelength from 0.4 µm to 14.4 µm. The responses are custom tailored to the individual needs of the user community and provide exceptionally low out-of-band response. Two bands are imaged at a nominal resolution of 250 m at nadir, with five bands at 500 m, and the remaining 29 bands at 1 km. A ±55-degree scanning pattern at the EOS orbit of 705 km achieves a 2,330-km swath and provides global coverage every one to two days.
In this study the MOD02 product acquired with the Aqua satellite is used. The Level 1B data set contains calibrated and geolocated at-aperture radiances for 36 bands generated from MODIS Level 1A sensor counts (MOD 01). The radiances are in W/(m2 µm sr). The NDVI is calculated using band 1 (620-670 nm) and band 2 (841-876 nm) which both have a spatial resolution of 250 meter:

$$NDVI_{MODIS} = \frac{band2 - band1}{band2 + band1} \qquad \text{Eq. 78}$$

[4] http://modis.gsfc.nasa.gov/index.php

### 6.2.4 Classification of the Upper Bhima sub basin

In this study a time series of 16 cloud free MODIS AQUA NDVI images is used from October 2004 to May 2005. Due to the monsoon cloud free images from June to September could not be obtained. The dates and time of acquisition of the images used are shown in Table 4.

*Table 4: Acquisition dates and time of MODIS imagery. Local time in the Upper Bhima catchment is GMT +5:30*

| Image # | Date | Acquisition time (GMT) | |
|---|---|---|---|
| | | Hour | Minute |
| 1 | 16/10/2004 | 8 | 10 |
| 2 | 21/10/2004 | 8 | 30 |
| 3 | 04/11/2004 | 8 | 40 |
| 4 | 22/11/2004 | 8 | 30 |
| 5 | 03/12/2004 | 8 | 10 |
| 6 | 17/12/2004 | 8 | 20 |
| 7 | 07/01/2005 | 8 | 40 |
| 8 | 18/01/2005 | 8 | 20 |
| 9 | 12/02/2005 | 8 | 15 |
| 10 | 19/02/2005 | 8 | 20 |
| 11 | 14/03/2005 | 8 | 30 |
| 12 | 23/03/2005 | 8 | 20 |
| 13 | 10/04/2005 | 8 | 10 |
| 14 | 19/04/2005 | 8 | 5 |
| 15 | 14/05/2005 | 7 | 55 |
| 16 | 17/05/2005 | 8 | 25 |

The 16 NDVI images which were used in the classification are shown in Figure 20. The NDVI peak is clearly just after the monsoon in October and for the major part of the sub basin the NDVI gradually decreases except for the forested parts in the Western Ghats and the irrigated areas downstream of the main reservoirs (Khadakwasla, Ujani and Yadgaon and Bhatghar). Just before the onset of the monsoon by the end of May the NDVI is lowest in the basin.

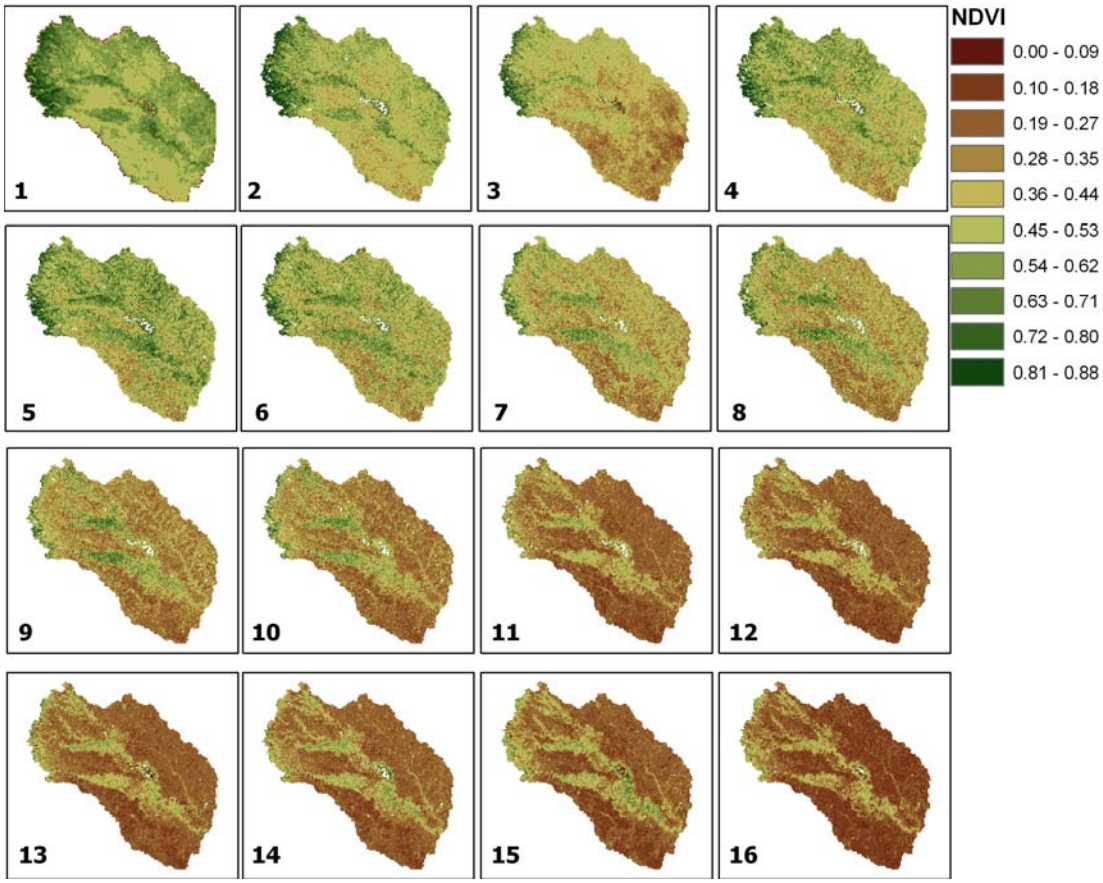


*Figure 20: 16 MODIS NDVI image used in the land use classification*

The 16 NDVI images were stacked into one image and an unsupervised classification using the K-means clustering was applied. Initially 15 clusters were chosen and a 0.95 convergence criterion was applied. The 15 classes were grouped into 7 major land use classes based on a field visit and a visual inspection using the Google Earth application[5], the old land use map and an additional decision rule using the slope derived from the SRTM DEM. The additional decision rule was required to distinguish between supplemental irrigated agriculture and low density forests and between irrigated agriculture and high density forests. Areas with slopes over 4% were classified as low density and high density forest respectively. The specifics of each class are shown in Table 5.

*Table 5: Specifics of the land use classes*

| Class name | Cluster # | Slope criterion | Area (ha) | Area % |
|---|---|---|---|---|
| Water | 1 | N/A | 38950 | 0.9 |
| Rangelands | 2-4 | N/A | 1228175 | 26.8 |
| Rainfed agriculture | 5-8 | N/A | 1536194 | 33.6 |
| Supplemental irrigated agriculture | 9-11 | < 4% (11) | 613575 | 13.4 |
| Irrigated agriculture | 12-15 | < 4% (15) | 910775 | 19.9 |
| Forest high density | 11 | > 4% | 143363 | 3.1 |
| Forest low density | 15 | > 4% | 103369 | 2.3 |

[5] http://earth.google.com

Rain fed agriculture covers the largest area in the basin (33.6%), but there are also considerable irrigated areas. The supplemental irrigated agriculture class covers around 13.4% of the basin area. These are areas which do not obtain their irrigation water from the large scale reservoirs but from groundwater or small tanks. The large command areas downstream of the major reservoirs cover a total area of 19.9%. The final LULC map is shown in Figure 21.

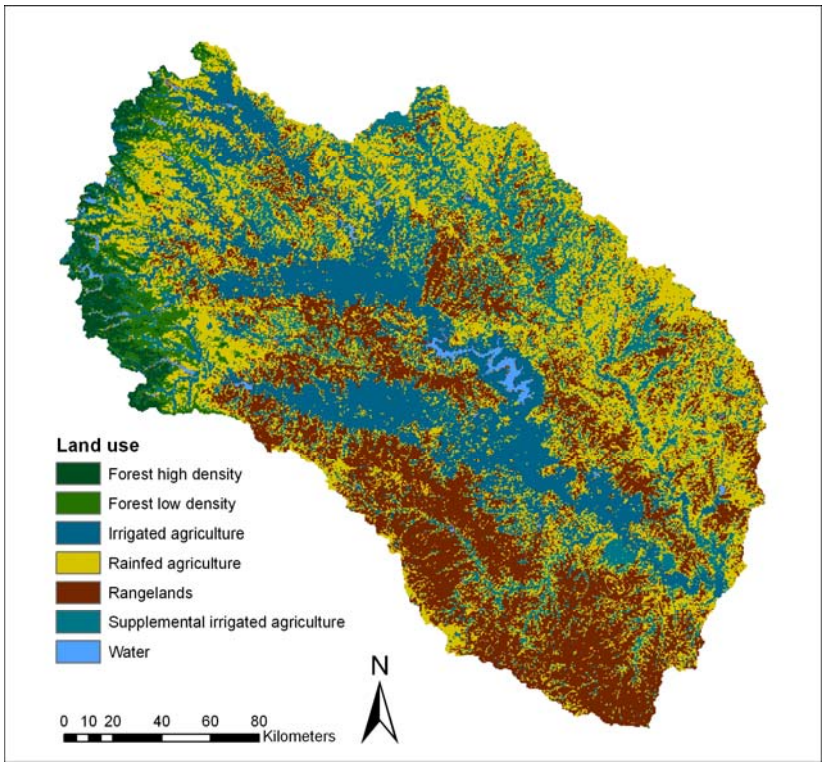


*Figure 21: LULC map Upper Bhima*

Table 6 shows a comparison between the acreages of each class in the old and the new classification. The differences are considerable. The area under rain fed agriculture has been reduced considerably (from 52.8% to 33.6%), while the area under irrigated agriculture has increased (4.4% to 19.9%). The forested areas in the Western Ghats are now also well depicted in the classification.

*Table 6: comparison between the two land use classifications*

| Class name | Area % (old) | Area % (new) |
|---|---|---|
| Water | 0.7 | 0.9 |
| Rangelands | 29.6 | 26.8 |
| Rainfed agriculture | 52.8 | 33.6 |
| Supplemental irrigated agriculture | 11.9 | 13.4 |
| Irrigated agriculture | 4.4 | 19.9 |
| Forest high density | 0.5 | 3.1 |
| Forest low density | 0.0 | 2.3 |

## 6.3 *Evapotranspiration mapping*

### 6.3.1 SEBAL

SEBAL provides a way to estimate and monitor actual ET with spatial sensitivity, without having to have soil moisture, land use and vegetation conditions. SEBAL solves the surface energy balance for heterogeneous terrain on the basis of reflected solar radiation and emitted thermal radiation (surface temperature). The actual ET ($ET_{act}$) fluxes from SEBAL reflect the effects of various natural factors that influence ET, such as moisture availability, presence of pests and disease, salinity, and other factors. The standard ET equations are designed to compute potential ET, or the level of ET that would occur under optimal or "pristine", although sometimes general corrections are applied for conditions where water is limiting limitations by using a reduction coefficient ($ET_{act}=\beta\ ET_{pot}$, e.g. Budyko, 1969).

SEBAL is one of the first mathematical procedures that can operationally estimate spatially distributed $ET_{act}$ from field to river basin scale over an unlimited array of land use types, including desert soil, open water bodies, sparse natural vegetation, rain fed crops, irrigated crops, etc. The SEBAL model solves the energy balance for every individual MODIS and Landsat pixel, thereby providing the spatial sensitivity. Satellite images need to be cloud-free to be processed for energy balance purposes.

The three primary bio-physical inputs from MODIS and Landsat images into SEBAL are (i) surface temperature, (ii) surface albedo and (iii) Normalized Difference Vegetation Index (NDVI) (see Figure 22). All of these parameters are measured directly or derived from measurements recorded by satellite-based sensors. In addition to that, a water mask is created. The water mask is meant for the assignment of particular values that are applicable to water only: emissivity, surface resistance, and soil heat flux/net radiation fraction. The latter fraction is relevant because the equations for soil heat flux for land and water are completely different. An existing generalized land use map is necessary to assign vegetation heights for the computation of the surface roughness for all pixels. This vegetation height is only considered for the turbulent parameters (i.e. momentum flux) and not for anything else. The inputs to SEBAL consists of (i) satellite multi-spectral radiances, (ii) routine weather data and (iii) DEM.

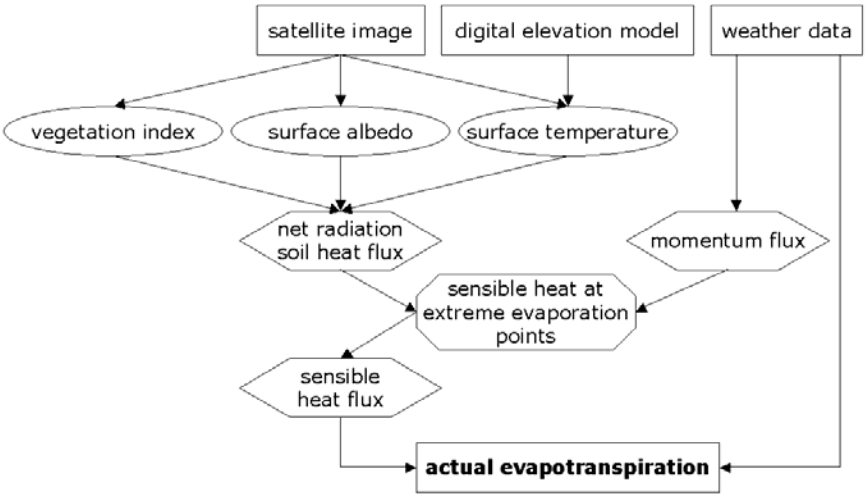


*Figure 22: Data flow and key steps for the determination of spatially distributed ET fluxes according to the SEBAL method*

SEBAL uses a set of algorithms to solve the energy balance at the earth's surface. The instantaneous ET flux is calculated for each pixel within a remotely sensed image as a 'residual' of the surface energy budget equation:

$$\lambda E = Rn - G - H \qquad \text{Eq. 79}$$

where λE is the latent heat flux (W/m2) (which can be equated to ET), Rn is the net radiation flux at the surface (W/m2), G is the soil heat flux (W/m2), and H is the sensible heat flux to the air (W/m2).

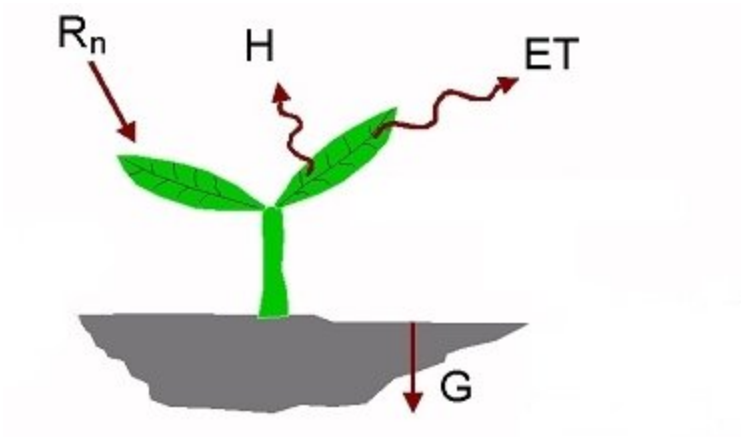


*Figure 23: Main terms of the Surface Energy Balance*

Rn represents the actual radiant energy available at the surface. It is computed by subtracting all outgoing radiant fluxes from all incoming radiant fluxes. This is further specified in the surface radiation balance equation:

$$Rn = RS\downarrow - \alpha\, RS\downarrow + RL\downarrow - RL\uparrow - (1 - \varepsilon 0)\, RL\downarrow \qquad \text{Eq. 80}$$

where $RS\downarrow$ is the incoming short-wave radiation (W/m2), $\alpha$ is the surface albedo (dimensionless), is the incoming long wave radiation (W/m2), $RL\uparrow$ is the outgoing long wave radiation (W/m2), and $\varepsilon o$ is the surface thermal emissivity (dimensionless).

In Eq. (2), the net short-wave radiation ($RS\downarrow - \alpha\, RS\downarrow$) that remains available at the surface is a function of the surface albedo ($\alpha$). The broad band surface albedo $\alpha$ is derived from the narrow band spectral reflectances $\alpha(\lambda)$ measured by each satellite band. The incoming short-wave radiation ($RS\downarrow$) is computed using the solar constant, the solar incidence angle, a relative earth-sun distance, and a computed broad band atmospheric transmissivity. In this application of SEBAL, atmospheric transmissivity was obtained from a few selected automatic weather stations in Nevada that sustained the data integrity check. The incoming long wave radiation ($RL\downarrow$) was computed using a modified Stefan-Boltzmann equation with an apparent emissivity that is coupled to the shortwave atmospheric transmissivity and a measured air temperature. Outgoing long wave radiation (RL) is computed using the Stefan-Boltzmann equation with a calculated surface emissivity and surface temperature. Surface temperature is derived from the narrow-band satellite measurements of thermal infrared radiation.

The challenge in energy balance modelling is to partition net radiation into sensible (H) and latent heat fluxes ($\lambda E$). To guide this partitioning process, extreme values of H are defined for 'hot' and 'cold' pixels selected by the operator. The hot pixel has a high surface temperature associated with the absence of evaporative cooling. Characteristics that qualify pixels for consideration as "hot" pixels are as follows: (i) their surface temperatures occur near the upper end of the frequency distribution of all pixels in the image, (ii) they have relatively scarce vegetative cover (as indicated by NDVI) and (iii) they appear to consist of essentially bare land on the false colour composite.

In contrast, characteristics that qualify pixels for consideration as "cold" pixels are as follows: (i) their surface temperatures occur near the lower end of the frequency distribution, (ii) they appear to be within open water surfaces or well irrigated fields and (iii) they have a low reflectance in the visible part of the spectrum. For each image processed, the operator must decide which pixels to select as the hot and cold pixels.

At the hot pixel it is assumed that ET is zero; thus, $H \approx Rn-G$. At the cold pixel, it is assumed that sensible heat is very small or zero, because all or most of the net available energy is used for ET; thus, $\lambda E \approx Rn-G$. The sensible heat does not necessarily have to be exactly zero, but it should be small.

Select of the hot and cold pixels for each image constrains the range of sensible heat within realistic bounds, essentially providing a self-calibrating feature, with the H fluxes for all other pixels lying between. Interpolation between these two bounds is done according to a linear function of surface temperature where the a and b coefficients are obtained from linking H to the surface temperature at the hot and cold pixels:

$$H = \{\rho a\ cp\ u^*\ (a + b\ T0)\} / \{\ln(z2/z1) - \psi h\ (z2,L) + \psi h\ (z1,L)\} \quad \text{Eq. 81}$$

Where $\rho a$ (kg/m3) is the moist air density, cp (J/kg/K) is the specific heat at constant pressure, u* (m/s) is the friction velocity, z (m) is the near-surface reference height to which the a,b coefficients as well as the constant H flux applies, $\psi h$ (-) is the stability correction for heat transport and L (m) is the Monin Obukhov length. Eq. (3) requires single layer wind speed observations and surface roughness for the determination of friction velocity u* to be known:

$$u^* = \{u(z2)\ k\} / \{\ln(z2/z0m) - \psi m\ (z2,L) + \psi m\ (zom,L)\} \quad \text{Eq. 82}$$

where z0m (m) is the surface roughness length for momentum transport and k (-) the von Karman's constant. SEBAL uses an iterative process to correct for atmospheric instability caused by buoyancy effects of surface heating. The surface roughness z0m is computed from estimates of vegetation height based on a simple land use mask and the actual LAI following the simple roughness model of Raupach (1994) and suggestions of model performance tests published by Verhoef et al. (1997).

In Eq. (1), the soil heat flux (G) and sensible heat flux (H) are subtracted from the net radiation flux at the surface (Rn) to compute the "residual" energy available for evapotranspiration (λE). Soil heat flux is empirically calculated as a G/Rn fraction using instantaneous surface temperature and an approximation for near-surface soil temperature at sunrise. A light interception reduction function is applied for the presence of foliage using NDVI as an indicator for canopies.

The λE time integration in SEBAL is split into two steps. The first step is to convert the instantaneous latent heat flux (λE) into daily λE24 values by holding the evaporative fraction constant. The evaporative fraction EF is:

$$EF = \lambda E / (Rn - G) \qquad (-) \quad \text{Eq. 83}$$

Field measurements under various environmental conditions indicate that EF is nearly constant with time during the diurnal cycle. Thus, because EF ~ EF24, the 24 hour latent heat flux can be approximated by:

$$\lambda E24 = EF\ \xi\ (Rn24 - G24) \qquad (W/m2) \quad \text{Eq. 84}$$

where ζ (-) is an advection enhancement parameter. It is assumed that the evaporative fraction EF specified in Eq. (5) remains quasi-constant during daytime hours and that variations can be related to advection ξ. Experimental work has demonstrated that this holds true for environmental conditions where soil moisture does not significantly change (e.g. Shuttleworth et al., 1989; Brutsaert and Sugita, 1992; Nicols and Cuenca, 1993; Kustas et al., 1994; Crago, 1996; Farah, 2001). This needs to be true for single days only to get an appropriate value for λE24 during satellite overpass days.

Advection occurs when hot desert air is blown over irrigated areas, typically in the afternoon, by winds driven by differences in air densities. The regional scale atmospheric circulation adds extra energy to moist vegetation. This extra energy can increase ET to the extent that it exceeds the net available

energy (Rn-G0), which from an energy balance point of view implies that the sensible heat flux is directed towards the surface (H is negative).

Within SEBAL, advection is incorporated into the $\zeta$ parameter that varies with the weather conditions and the moisture of the underlying soils. The impact of weather conditions on advection is expressed by the changes of the evaporative fraction of the reference crop ETgrass between satellite overpass and the 24-h counterpart governed by day and night weather conditions. The influence of advection decreases non-linearly with soil moisture content, which implies that only wet surface are exposed to advection.

Depending on the time scale chosen, different time integrations of (Rn- G0) need to be obtained. For the daily time scale, ET24 is formulated as:

$$ET_{24} = \frac{86400 \cdot 10^3}{\lambda \rho_w} \lambda E24 \qquad \text{(mm d-1)} \qquad \text{Eq. 85}$$

where Rn24 (W m-2) is the 24-h averaged net radiation, $\lambda$ (J kg-1) is the latent heat of vaporization, $\rho$w (kg m-3) is the density of water.

The second step is the conversion from a daily latent heat flux into 14-day values, which was achieved by application of the Penman-Monteith equation:

$\lambda E24PM = (sa\ Rn24 + \rho acp\ \Delta e/ra) / (sa + \gamma\ (1 + rs/ra))$ (W/m2) Eq. 86

where sa (mbar/K) is the slope of the saturated vapour pressure curve, ρacp (J/m3 K) is the air heat capacity, Δe (mbar) is the vapour pressure deficit, γ (mbar/K) is the psychrometric constant and ra (s/m) is the aerodynamic resistance. The parameters sa, Δe and ra are controlled by meteorological conditions, and Rn and rs by the hydrological conditions.

The SEBAL computations can only be executed for cloudless days. The result of λE24 (Eq. 85) has been explored to convert the Penman-Monteith equation (Eq. 86) and to quantity rs inversely using λE24= λEPM. The spatial distribution of rs so achieved, will consequently be used to compute λE24 by means of Eq. 86 for all days without satellite image available (e.g. Farah, 2001). The total ETact for a given period can be derived from the shorter term average values of sa, Δe, ra and Rn

The standard 250 m Digital Elevation Model (DEM) has been used for the correction of air pressure and related air density and psychrometric constant at higher elevation. The DEM is also used to correct the absorbed solar radiation values, both for slope and aspect. Southern facing terrain, due to the angle of incidence, absorbs more solar radiation per unit land than the Northern facing slope.

### 6.3.2 Reference evapotranspiration

Figure 24 shows the reference ET ($ET_{ref}$) of the catchment. $ET_{ref}$ is generally homogeneously distributed, except for some effects of slope and aspect in the Western Ghats. The average $ET_{ref}$ for the eight month period from October 2004 to May 2005 is approximately 1200 mm.

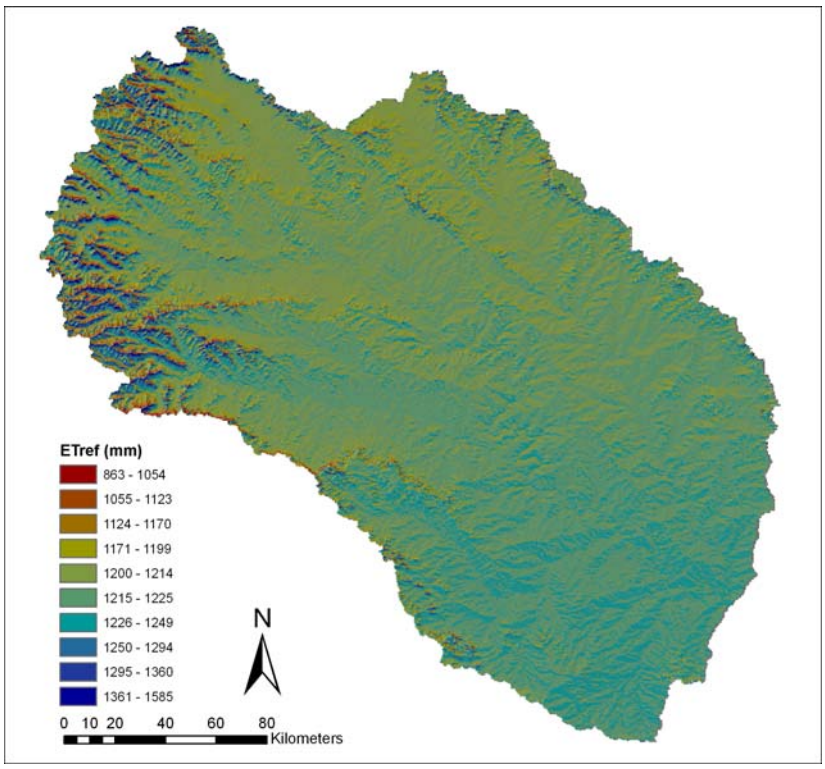


*Figure 24: Total reference evapotranspiration from 1 October 2004 to 31 May 2005*

The distribution of $ET_{ref}$ in time is shown in Figure 25. $ET_{ref}$ is minimal in December (110 mm/month) and maximized in May (220 mm/month)

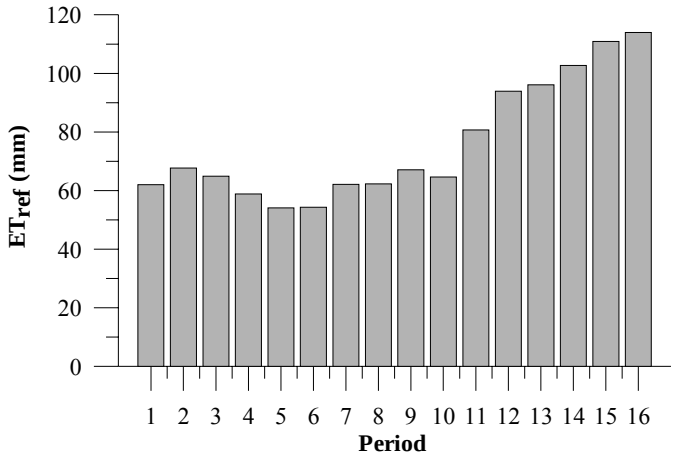


*Figure 25: Bi-weekly reference evapotranspiration from 1 October 2004 to 31 May 2005*

### 6.3.3 Potential Evapotranspiration

Potential ET ($ET_{pot}$) is not only governed by meteorological processes, but also by plant and crop characteristics and their respective growth cycles. It can be interpreted as the evapotranspiration under optimal environmental conditions without nutrient or water stress. The spatial variation in $ET_{pot}$ is much larger than in $ET_{ref}$ (Figure 26). $ET_{pot}$ ranges from 1700 mm/8 months in the forested areas in the Western Ghats to around 300 mm/8 months in the idle rangelands.

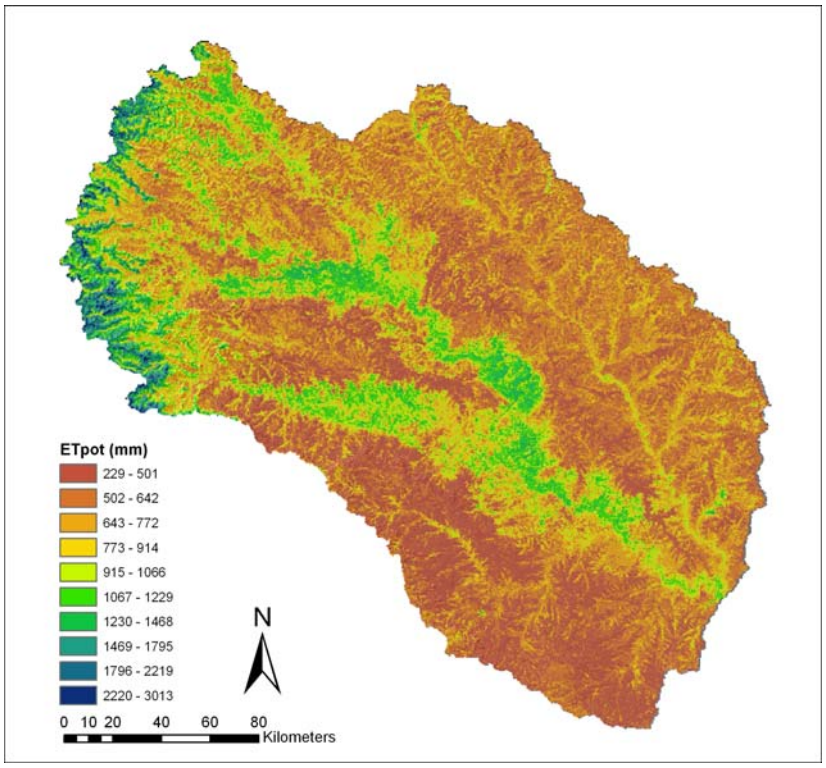


*Figure 26: Total potential evapotranspiration from 1 October 2004 to 31 May 2005*

### 6.3.4 Actual Evapotranspiration

Actual evapotranspiration ($ET_{act}$) is derived from $ET_{pot}$ after inferring environmental stress, e.g. nutrient, water, pests and diseases. The land use patterns, specifically open water, are clearly visible in Figure 27. The sum of the eight month actual ET ranges from around 100 mm for the idle rangelands to over 1500 mm for the open water surfaces.

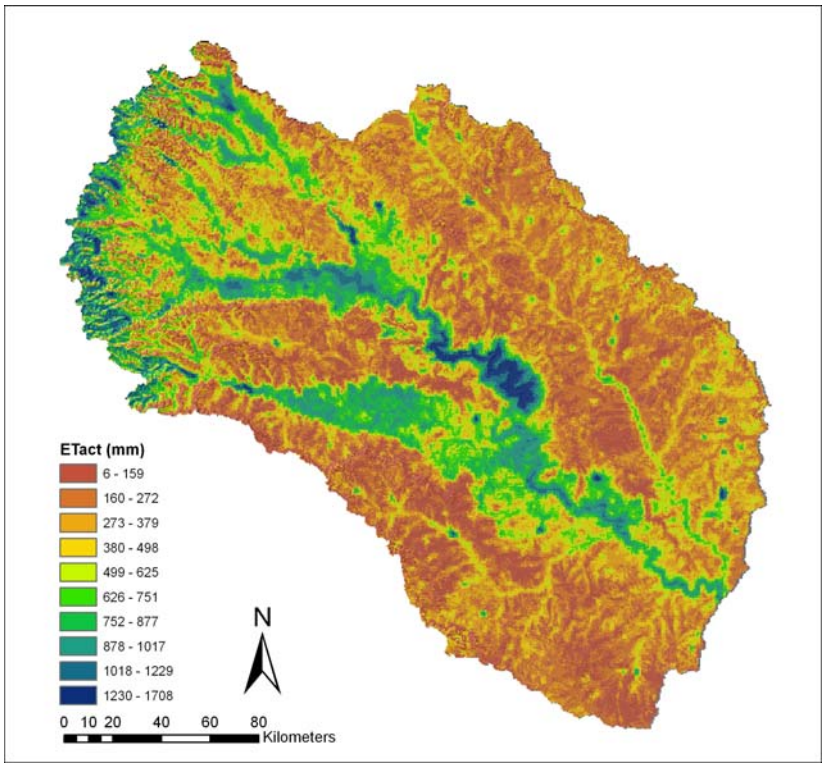


*Figure 27: Total actual evapotranspiration from 1 October 2004 to 31 May 2005*

It is also interesting to evaluate the temporal patterns in $ET_{pot}$ and $ET_{act}$ per land use class (Figure 28). The figure shows large differences between the land use classes. Water (WATR) has the highest $ET_{act}$ throughout the year. The general temporal patterns are consistent with a peak in evaporative depletion just after the monsoon. The forested land covers have the largest evaporation deficit ($ET_{pot}$-$ET_{act}$), while for the irrigated sugarcane (AGR3) the ET deficit is relative small due to continuous irrigation. AGR3 is high throughout the year even in the extremely dry period from February to May.

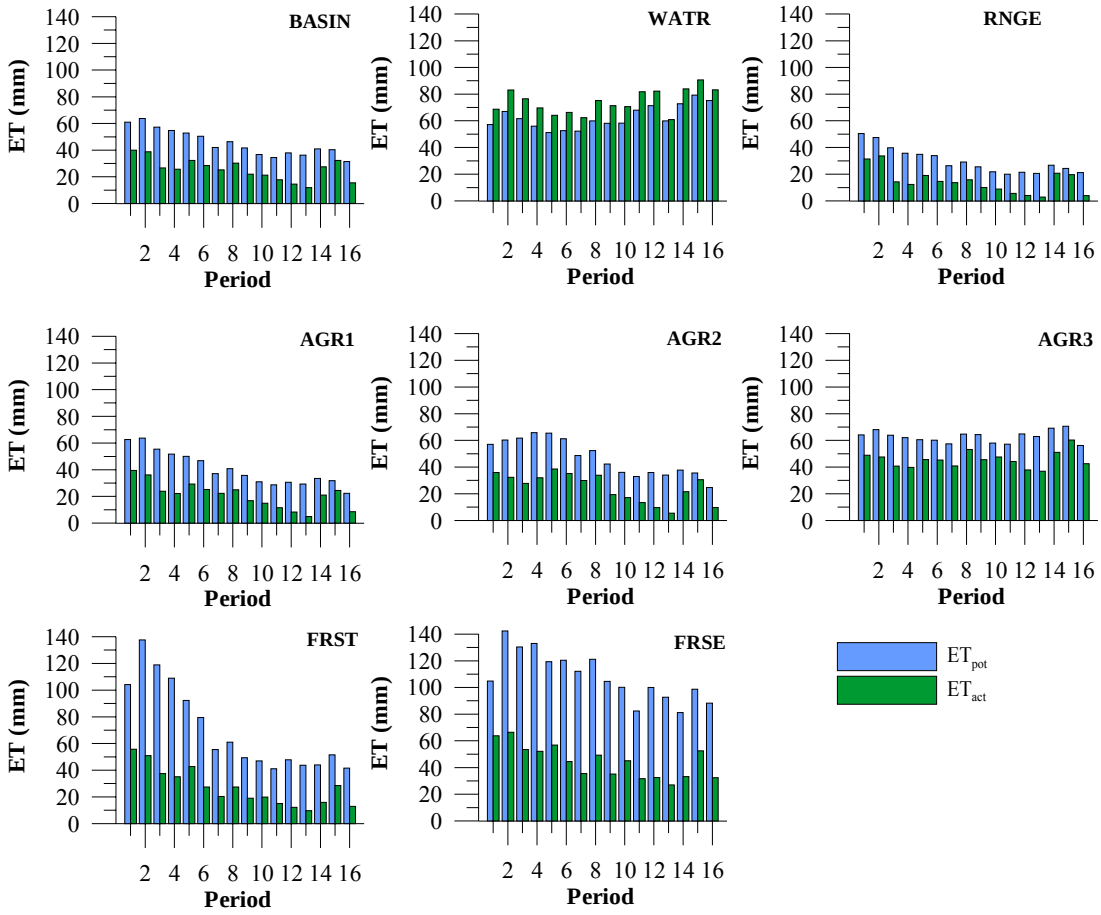


*Figure 28: Bi-weekly potential and actual evapotranspiration per land use from 1 October 2004 to 31 May 2005*

### 6.3.5 Biomass production

SEBAL also calculates the monthly biomass production. The sugarcane areas are clearly visible. Sugarcane is a C4 crop and produces twice the amount of biomass under the same condition of a regular C3 crop. The eight months sum of biomass production for sugarcane is around 50,000 kg/ha, while the idle range lands produce less than 5,000 kg/ha.

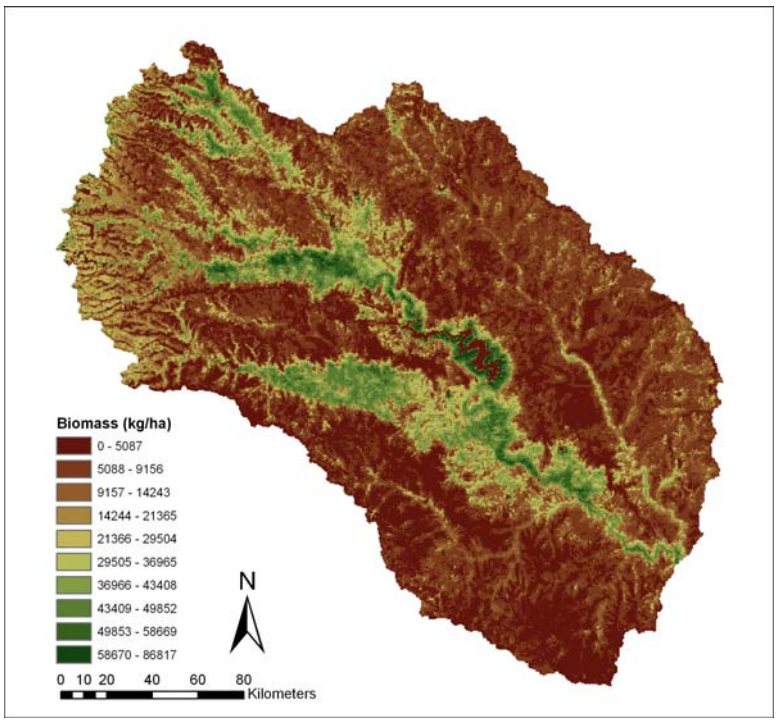


*Figure 29: Total biomass production from 1 October 2004 to 31 May 2005*

In time biomass production roughly follows the $ET_{act}$ pattern with a peak after the monsoon (1400 kg/ha) and a minimum biomass production at the end of the dry season (400 kg/ha)

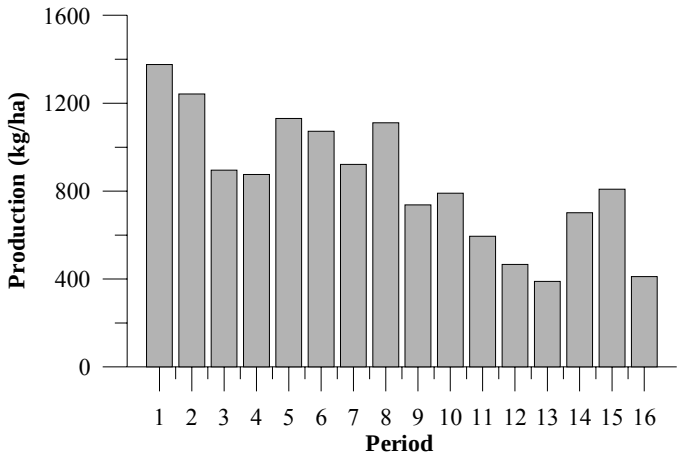


*Figure 30: Bi-weekly biomass production from 1 October 2004 to 31 May 2005*

## 6.4 *Precipitation mapping using Remote Sensing*

### 6.4.1 Introduction

A limited set of precipitation data from meteorological stations is available for the Upper Bhima catchment. A dataset with monthly precipitation data for 8 Indian Meteorological Department (IMD) stations and for 15 additional stations from the National Data Centre (NDC) in Pune were available. The location, source and time coverage of the data is shown in Figure 31.

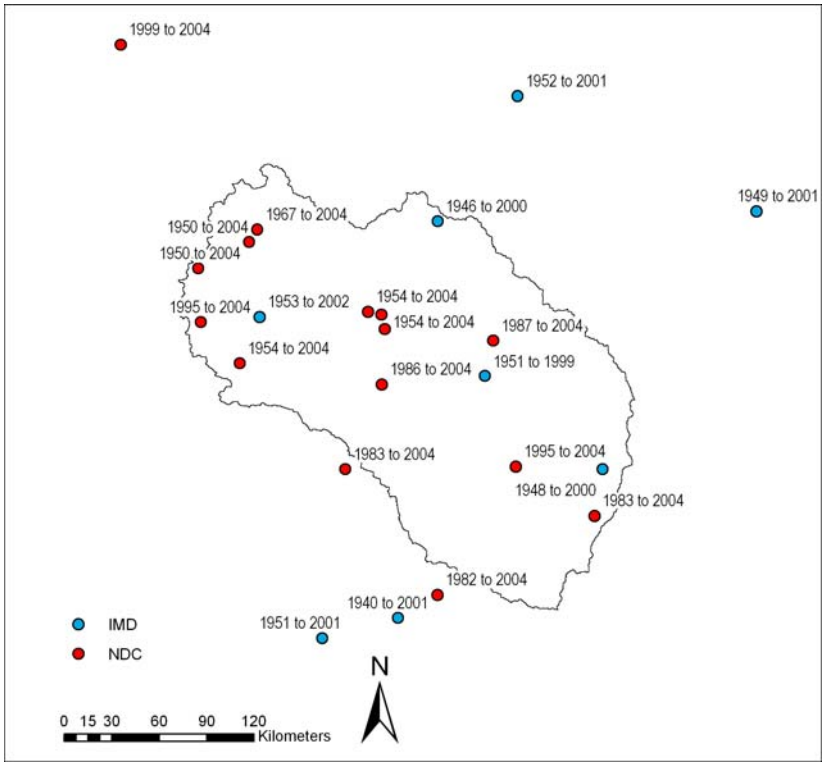


*Figure 31: Location, source and time overage monthly precipitation data*

Since there is an extreme spatial variation in precipitation ranging from 2000 mm in the Western Ghats to 650 mm in the most eastern part of the sub-basin it is important to have a dense network of meteorological stations. In this study SEBAL evapotranspiration maps will be used to calibrate the hydrological model. SEBAL data are available from October 2004 until May 2005, but precipitation data are only available up to 2004 for a limited number of stations. For these reasons Remote Sensing derived precipitation from the Tropical Rainfall Monitoring Mission (TRMM) is used in this study.

### 6.4.2 Tropical Rainfall Monitoring Mission[6]

The Tropical Rainfall Measuring Mission (TRMM) is a joint space project between NASA and the Japanese Aerospace Exploration Agency (JAXA). TRMM is designed to measure tropical precipitation and its variation from a low-inclination orbit combining a suite of sensors to overcome many of the limitations of remote sensors previously used for such measurements from space. The fundamental

[6] http://trmm.gsfc.nasa.gov/

objective of TRMM is to understand the role of latent heat in driving the circulation of the global atmosphere. With the inclusion of rain radar, TRMM will provide the first opportunity to estimate the vertical profile of the latent heat that is released through condensation. The TRMM rainfall data is particularly important for studies of the global hydrological cycle and for testing the realism of climate models, and their ability to simulate and predict climate accurately on the seasonal time scale. Other scientific issues such as the effects of El Niño on climate could be addressed with a reliable, extended time series of tropical rainfall observations as well. The TRMM satellite has a latitudinal range from 50°S - 50 °N. The TRMM satellite has been launched November 27 in 1997 and the mission has recently been extended to 2009.

The observatory for rainfall observations consists of precipitation radar, a multi-frequency microwave radiometer and a visible and infrared (VIS/IR) radiometer. Used in this combination in a complementary way, these sensors, with the designed orbit of 350 km altitude and inclination of 35°, will meet the measurement accuracy for rainfall needed to fulfil the stated science objectives of the mission. For related precipitation observations (i.e., lightning) and for additional important climate observations, a lightning imager and an Earth radiation budget sensor have been added. A brief description of each of the five instruments is included here:

- The Precipitation Radar (PR), the first in space, will measure the 3-D rainfall distribution over both land and ocean. More specifically, this instrument will define the layer depth of the precipitation and provide information about the rainfall reaching the surface, the key to determining the latent heat input to the atmosphere. A unique feature is that it will permit the measurement of rain over land where passive microwave channels have more difficulty. The PR is an electronical scanning radar operating at 13.8 GHz with horizontal polarization using a 128-slotted waveguide antenna and solid state power amplifiers to develop an active phased array. The horizontal resolution is 4.3 km at nadir, the range resolution is 250 m and the scanning swath width is 220 km.
- The multi-channel microwave radiometer, designated as the TRMM Microwave Imager (TMI), is designed to provide information on the integrated column precipitation content, its areal distribution, and its intensity. The horizontal resolution will allow the definition and investigation of most rainfall types, including convective cells. The technique is best suited for estimates over oceans, where data are needed most for climate model verification. The TMI will operate on 5 frequencies, of which 4 will have dual polarization thus providing 9 channels of data. The 5 frequencies are 10.65 GHz, 19.35 GHz, 22.235 GHz (single polarization), 37.0 GHz and 85.5 GHz. The horizontal resolution of the TMI will range from 5 km at 85.5 GHz to 45 km at 10.65 GHz. A scan angle of 65° will provide a swath width of 760 km.
- The Visible Infrared Scanner (VIRS) will provide very high resolution information on cloud coverage, type, and cloud top temperatures and also serve as the link between these data and the long and virtually continuous coverage by the geosynchronous meteorological satellites. The VIRS is a 5 channel cross-track scanning radiometer operating at 0.63, 1.6, 3.75, 10.80, and 12.0 microns. The instrument, with a swath width of 720 km, will provide cloud distributions by type and height and rain estimates from brightness temperatures at a horizontal resolution of 2.1 km (nadir). Direct correlation with PR and TMI measurements will assist in providing more accurate rain estimates from VIRS thereby enhancing its capability for verifying or calibrating the rain estimates from operational meteorological satellites.

- The Lightning Imaging Sensor (LIS) is designed to investigate the global incidence of lightning, its relationship with the global electric circuit, and, in conjunction with the PR, TMI, and VIRS, its correlation with rainfall. Lightning is not a necessary condition for tropical rainfall such as warm rain or even for some convective rainfall in the tropics. However, when updrafts and downdrafts are sufficient to cause lightning, rainfall results. LIS will be optimized to detect the lightning location, mark the time of occurrence, and measure the radiant energy. LIS is a calibrated optical sensor operating at 0.7774 microns and will observe the distribution and variability of lightning over the Earth. The horizontal resolution at nadir will be 5 km and the swath width will be 590 km.

Several orbital and gridded data products are available for download at the Goddard Distributed Active Archice Centre (DAAC)[7]. For this study the 3B-43 product is used. The global rainfall algorithm (3B-43) combines the estimates generated by combined instrument rain calibration (3B-42) and global gridded rain gauge data from CAMS, produced by NOAA's Climate Prediction Center and/or global rain gauge product, produced by the Global Precipitation Climatology Center (GPCC). The output is rainfall for 0.25x0.25 degree grid boxes for each month.

### 6.4.3 Downscaling and calibration of TRMM data

For the model simulation the irrigation year June 2004 to May 2005 will be used in the simulations. SEBAL data are available from October 2004 to May 2005. The total precipitation at the original resolution from June 2004 to May 2005 is shown on the left side of Figure 34. The 0.25 degree resolution is still too coarse for application in a simulation model. Therefore a downscaling procedure is developed and applied to the data. For all meteorological stations in the sub-basin which cover the period 1998-2004 the monthly TRMM data were extracted. For each station a regression analysis was performed on the monthly precipitation amounts.

*Table 7: Slope, intercepts and $R^2$ for the 13 selected meteorological stations*

| Station | Slope | Intercept | $R^2$ |
|---|---|---|---|
| Ambavade-2 | 0.26 | 21.94 | 0.29 |
| Askheda | 0.80 | 18.15 | 0.80 |
| Barur (Takali) | 0.59 | 16.34 | 0.51 |
| Chaskman | 1.06 | 11.79 | 0.81 |
| Kashti | 0.40 | 18.49 | 0.37 |
| Khamgaon | 0.86 | 18.29 | 0.65 |
| Late | 0.47 | 2.65 | 0.50 |
| Pargaon | 0.84 | 20.15 | 0.64 |
| Rosa (Kolgaon) | 0.71 | 15.34 | 0.57 |
| Sakhar | 1.09 | 0.84 | 0.82 |
| Shirur | 0.32 | 12.69 | 0.45 |
| Sidhewadi | 0.58 | 19.03 | 0.51 |
| Wegre (Muthe) | 0.70 | 37.58 | 0.68 |

Table 7 shows the slopes, intercepts and $R^2$ values of the regression analysis. The $R^2$ values vary from 0.29 (Ambavade-2) and 0.82. For Askheda and Sakhar the scatter plots are shown in Figure 32.

[7] http://disc.sci.gsfc.nasa.gov/data/datapool/TRMM/01_Data_Products/index.html

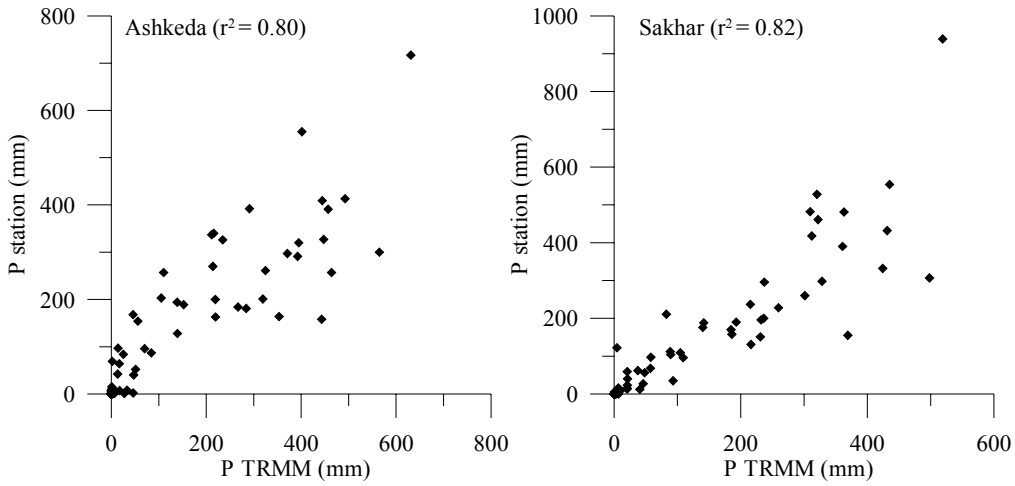


*Figure 32: Scatterplots for monthly TRMM precipitation and observed precipitation from 1998-2004 for two meteorological stations*

The next step in the downscaling procedure is the spatial interpolation of the slopes and intercepts of the meteorological stations (Figure 33). To avoid erroneous precipitation amounts, especially in the dry seasons, only those station with an $R^2$ > 0.50 and an intercept < 20 are used in the interpolation (7 stations). The slopes range from 0.57-1.10 and the intercepts range from 0-22 mm/month.

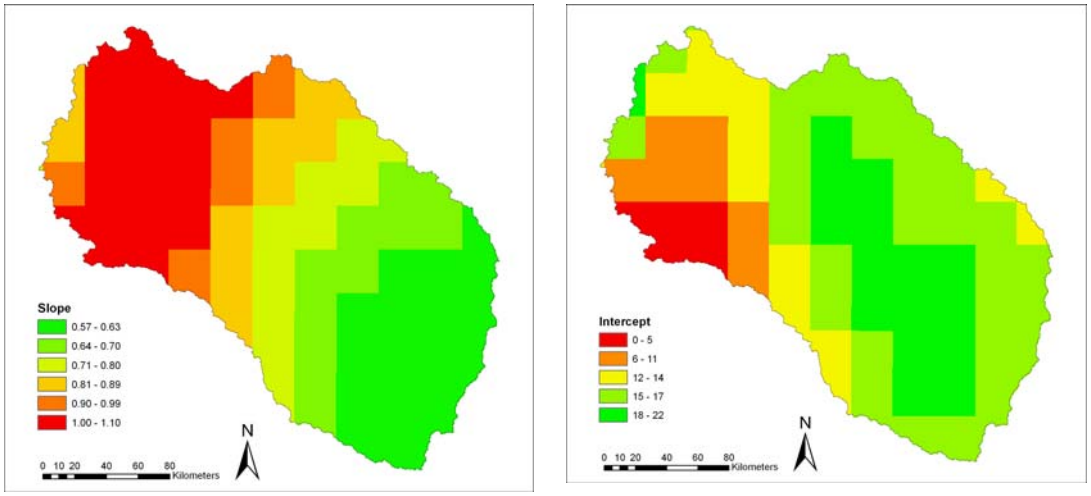


*Figure 33: Slope and intercept used to scale TRMM derived precipitation*

The final step in the procedure is to convert the centers of the TRMM grid boxes to points and to interpolated these points to a raster of a higher resolution (0.005 degrees by 0.005 degrees). A spline tension interpolator was used with weight 1 and using 4 surrounding points (Franke, 1982). The result of this downscaling procedure is shown in Figure 34.

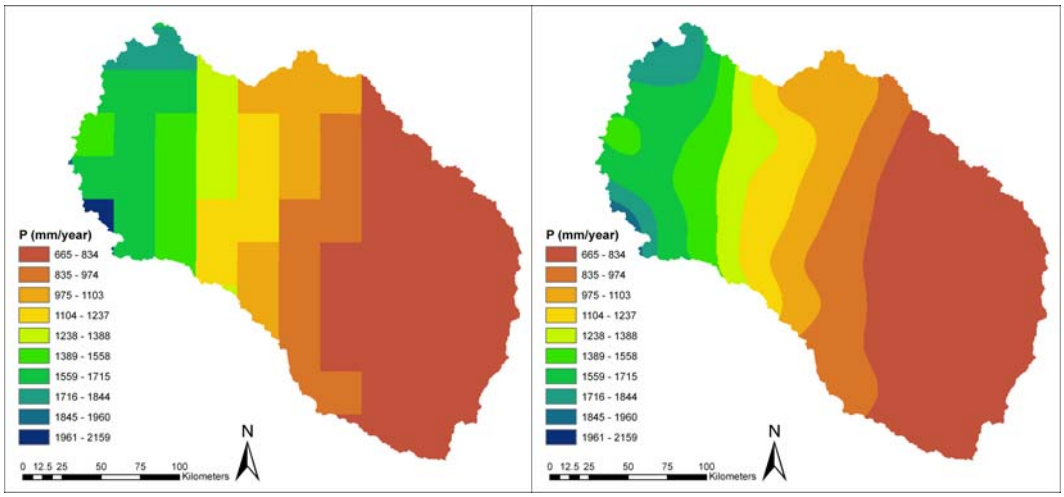


*Figure 34: Total precipitation from June 2004 to May 2005. The scaled TRMM data is shown in the left figure and the downscaled TRMM data is shown in the right figure.*

This downscaling procedure is repeated for each month between June 2004 and May 2005. Figure 35 shows the monthly precipitation in the basin. Precipitation is clearly concentrated in the monsoon months from June to September with the peak in July 2005. There is a clear decreasing trend from the western to the eastern part of the sub basin.

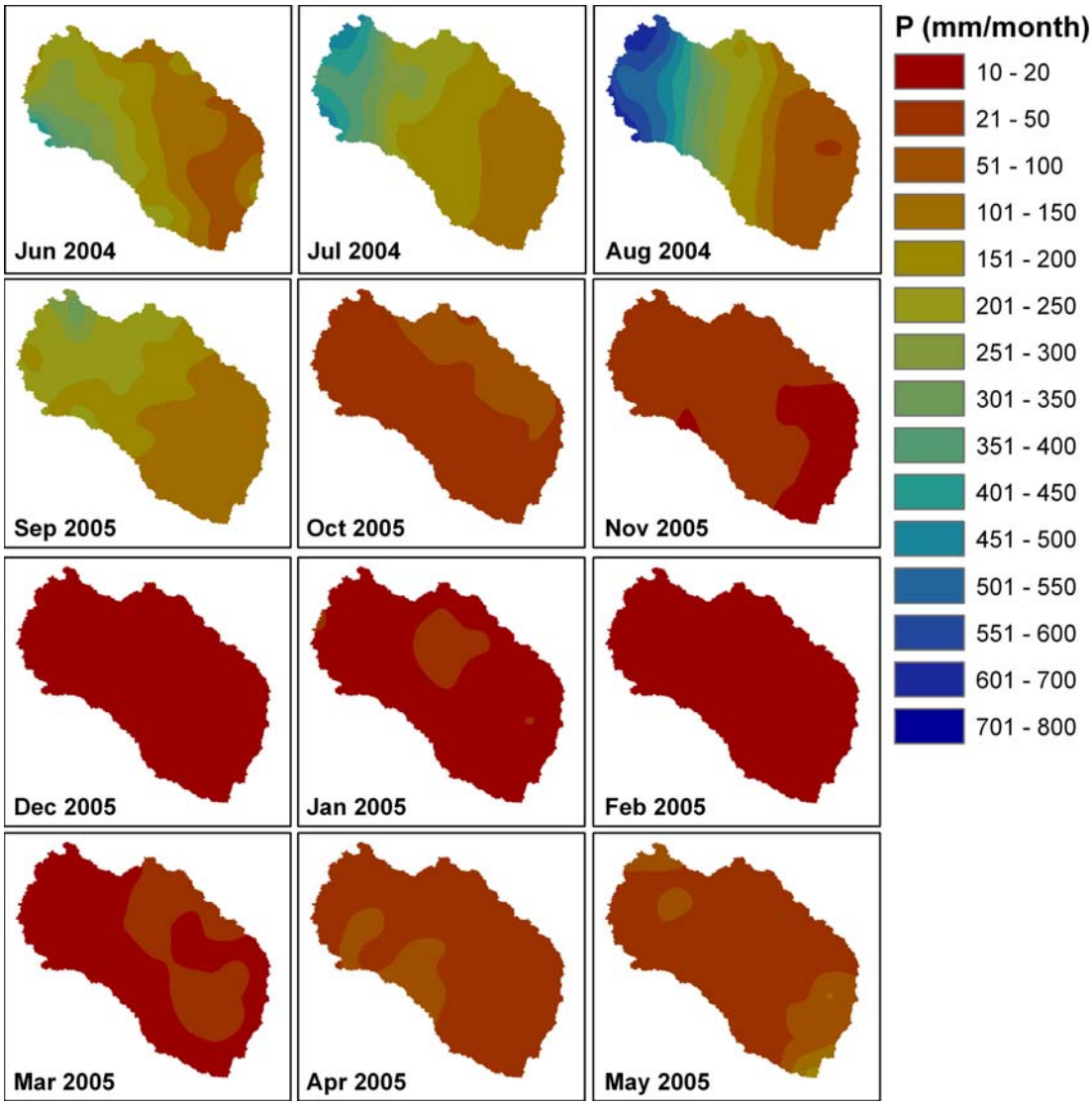


*Figure 35: Monthly downscaled TRMM derived precipitation in the Upper Bhima sub basin*

## 6.5 *Modeling the Upper Bhima catchment*

The SWAT model of the Upper Bhima catchment is created in several consecutive steps, which are described in this chapter. Based on the topography the catchment is subdivided into smaller units (sub- basins)

### 6.5.1 Topography

A Remote Sensing derived digital elevation model (DEM) acquired with Shuttle Radar Topographic Mission (SRTM)[8] is used to partition the catchments in sub-basins and rivers. GIS based hydrological surface function are used in an automated procedure of the SWAT GIS interface (AVSWAT). The original DEM has a spatial resolution of 90m, but to reduce calculation times the DEM is resampled to a spatial resolution of 250 m.

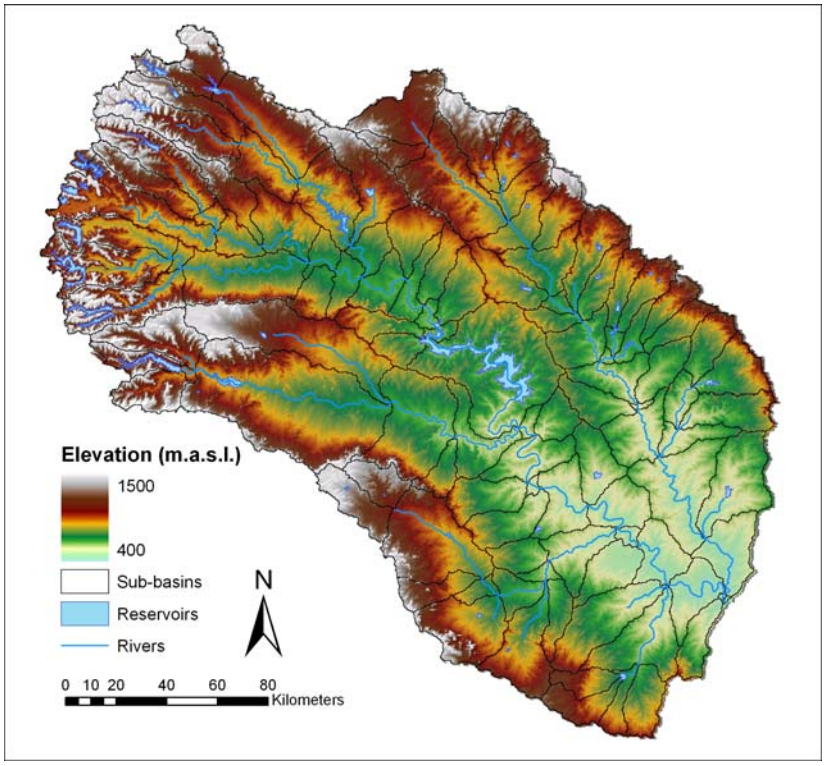


*Figure 36: Digital elevation model, sub-basins, and major rivers*

Figure 36 show the DEM of the catchment. The elevation ranges from 414m in the east of the catchment to 1458m in the western Ghats. The elevation distribution of the entire catchment is shown in Figure 37. It shows that nearly 95% of the area of the catchment is below 800m.

[8] http://www2.jpl.nasa.gov/srtm/

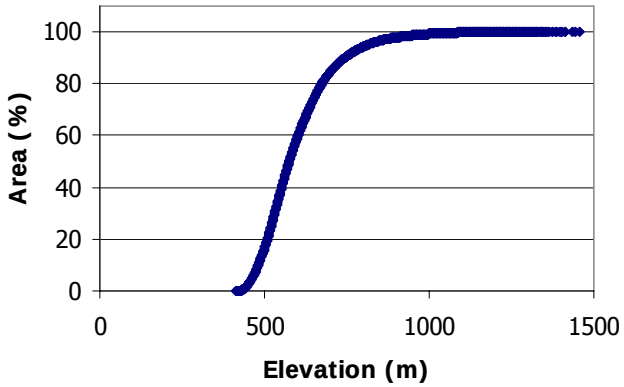


*Figure 37: Elevation distribution in the catchment*

The catchment has an area of 4.567.781 ha and a total of 115 sub-basins are delineated with a minimum area of 20.000 ha (Figure 36).

### 6.5.2 Soils

The FAO UNESCO digital soil map of the world is used in this study (FAO, 1995). The Digital Soil Map of the World (DSMW) CD-ROM is based on the FAO/UNESCO Soil Map of the World. The FAO-Unesco Soil Map of the World was published between 1974 and 1978 at 1:5.000.000 scale. The soil map of the world was prepared on the base of the topographic map series of the American Geographical Society of New York . The legend of the original soil map of the World (FAO, 1974) comprises an estimated 4930 different map units, which consist of soil units or associations of soil units. When a map unit is not homogeneous, it is composed of a dominant soil and component soils. The latter are: associated soils, covering at least 20 % of the area; and inclusions, important soils which cover less than 20 % of the area. The legend of the soil map of the world (1974) comprises 106 soil units (from Af to Zt), grouped in 26 major soil groupings. The soil map for the upper Bhima catchment is shown in Figure 38.

The majority of the alluvial plains in the catchment consist of chromic vertisols. Vertisols are churning heavy clay soils with a high proportion of swelling 2:1 lattice clays. These soils form deep wide cracks from the surface downward when they dry out, which happens in most years. Dry Vertisols have a very hard consistence; wet vertisols are (very) plastic and sticky. It is generally true that vertisols are friable only over a narrow moisture range but their physical properties are greatly influenced by soluble salts and/or adsorbed sodium. Infiltration of water in dry (cracked) vertisols with surface mulch or a fine tilth is initially rapid. However, once the surface soil is thoroughly wetted and cracks have closed, the rate of water infiltration becomes almost zero. (The very process of well/shrink implies that pores are discontinuous and non-permanent.) If, at this stage, the rains continue (or irrigation is prolonged), vertisols flood readily. The highest infiltration rates are measured on vertisols that have a considerable shrink/swell capacity, but maintain a relatively fine class of structure. Not only the cracks transmit water from the (first) rains but also the open spaces between slickensided ped surfaces that developed as the peds shrunk. Data on the water holding capacity of vertisols vary widely, which may be attributed to the complex pore space dynamics. Water is adsobed at the clay surfaces and retained between crystal lattice layers. By and large, vertisols are soils with good water holding properties. However, a large proportion of all water in vertisols, and notably the water held between the basic

crystal units, is not available to plants. Investigations in the Sudan Gezira have shown that the soil moisture content midway between large cracks changes very little, if at all, when the clay plain is flooded for several days or even several weeks. The soil's moisture content decreases gradually from more than 50 percent in the upper 20 cm layer to 30 percent at 50 cm depth. Deeper than 100 cm, the soil moisture content remains almost invariant throughout the year.

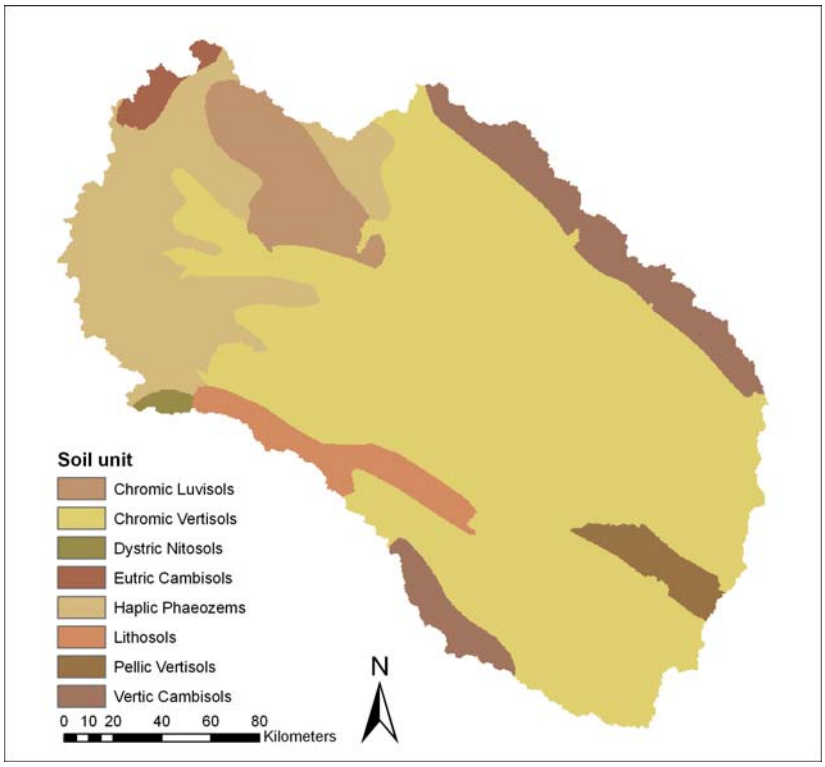


*Figure 38: FAO/UNESCO soil map of the Upper Bhima catchment*

The upland areas mainly have a luvisol soil type. This soil type is common in upland areas with a distinct wet and dry season. Luvisols have favourable physical properties; they have granular or crumb surface soils that are porous and well aerated. The `available' moisture storage capacity is highest in the argic horizon (15 to 20 volume percent). The argic horizon has a stable blocky structure but surface soils with a high silt content may be sensitive to slaking and erosion. Most vuvisols are well drained but vuvisols in depression areas with shallow groundwater may develop gleyic soil properties in and below the argic horizon. Stagnic properties are found where a dense illuviation horizon obstructs downward percolation and the surface soil becomes saturated with water for extended periods of time.

The physical properties needed for the SWAT model are also derived from the FAO soil map of the world. These are summarized in Table 8.

*Table 8: Soil physical properties*

| Code | Description | Depth | AWC | Clay | Silt | Sand | Bulk density | Organic carbon content |
|---|---|---|---|---|---|---|---|---|
| | | cm | mm/mm | % | % | % | g/cm3 | % |
| Be66-2c | Eutric Cambisols | 1280 | 0.21 | 22 | 35 | 43 | 1.21 | 0.79 |
| Bv12-3b | Vertic Cambisols | 1430 | 0.10 | 50 | 21 | 30 | 1.59 | 0.77 |
| Hh11-2bc | Haplic Phaeozems | 1368 | 0.15 | 28 | 24 | 48 | 1.51 | 0.52 |
| I-Hh | Lithosols | 950 | 0.17 | 21 | 21 | 58 | 1.45 | 0.56 |
| Lc75-1b | Chromic Luvisols | 1430 | 0.14 | 29 | 21 | 50 | 1.53 | 0.60 |
| Nd51-2b | Dystric Nitosols | 2250 | 0.19 | 34 | 18 | 48 | 1.19 | 0.74 |
| Vc43-3ab | Chromic Vertisols | 2150 | 0.20 | 32 | 16 | 52 | 1.20 | 0.52 |
| Vc44-3a | Chromic Vertisols | 1430 | 0.07 | 54 | 23 | 23 | 1.70 | 0.59 |
| Vc45-3a | Chromic Vertisols | 1550 | 0.07 | 58 | 19 | 23 | 1.71 | 0.41 |
| Vp42-3a | Pellic Vertisols | 1550 | 0.08 | 57 | 23 | 21 | 1.65 | 0.51 |

### 6.5.3 Hydrological Response Units

Hydrological Response Units (HRUs) are the smallest unit of calculation in the SWAT model and are defined as unique combinations of soil and land use. Before determining the HRUs a pre-processing step is taken. However an area threshold is specified for both soils and land use. This threshold determines whether a certain soil or land use class is used as an HRU based on the proportion of the total sub basin area the soil class or land use type has. The thresholds used are 10% and 5 % for soil and land use respectively. The HRUs are created using an automated procedure in the AVSWAT interface. A total of 768 HRU are generated. A map with the HRUs is shown in Figure 39.

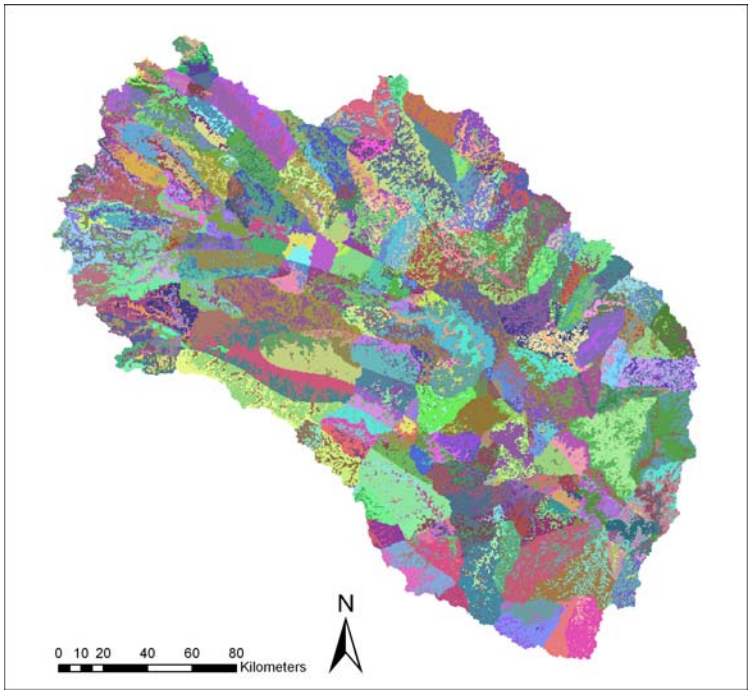


*Figure 39: Hydrological Response Units in the catchment*

### 6.5.4 Meteorology

The SWAT model requires the following daily meteorological parameters:

- Solar radiation
- Minimum and maximum temperature
- Relative humidity
- Wind speed
- Precipitation

Different sources of information have been used to derive the daily weather data from 1 June 2004 to 31 May 2005. For all parameters data are used for two different meteorological stations; one in Pune and one in Sholapur (Figure 40). Similar to the procedure in SEBAL: the data of the two stations have been averaged. For precipitation a virtual meteorological station is created for each of the 112 subbasins.

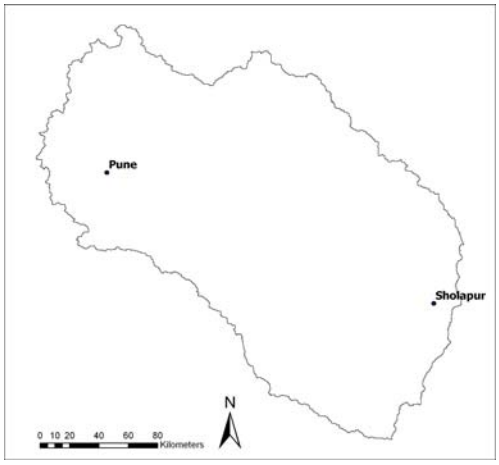


*Figure 40: Location of the meteorological stations*

#### 6.5.4.1 Solar radiation

The solar radiation is defined as the amount of radiation reaching a horizontal plan on the earth's surface. First the extraterrestrial radiation at the top of the atmosphere was calculated, which is then corrected for scattering, reflection and adsorption by atmospheric gases, clouds and dust. The extraterrestrial radiation is depending on the latitude and the Julian day in the year. The amount of solar radiation ($Q_s$ (MJ $m^{-2}$ $day^{-1}$)) reaching the surface of the earth is calculated using the Angström formula:

$$Q_s = \left( a_s + b_s \frac{n}{N} \right) \cdot Q_a \qquad \text{Eq. 87}$$

Where $a_s$(-) is a regression constant, expressing the fraction of extraterrestrial radiation reaching the earth on overcast days, $a_s+b_s$ is the fraction of extraterrestrial radiation reaching the earths surface on clear days, n/N (-) is the relative sunshine duration and $Q_a$ (MJ $m^{-2}$ $day^{-1}$) is the extraterrestrial radiation. Values of 0.25 and 0.50 are used for $a_s$ and $b_s$ respectively.

Solar radiation is calculated for both Pune and Sholapur (Figure 41). The relative sunshine duration is derived from the IWMI climate atlas[9].

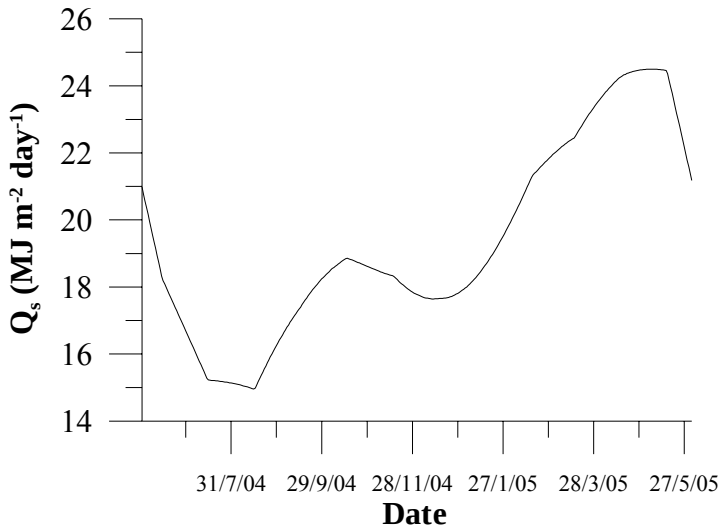


*Figure 41: Average daily solar radiation Pune and Sholapur*

#### 6.5.4.2 Temperature

Public domain data[10] are used for daily maximum and minimum temperature (Figure 42).

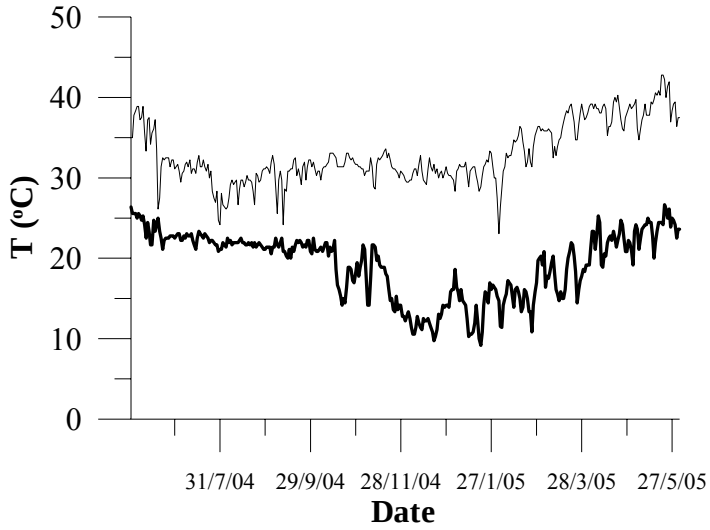


*Figure 42: Average daily maxium and minium temperature*

[9] http://www.iwmi.cgiar.org/WAtlas/atlas.htm
[10] http://www.wunderground.com

#### 6.5.4.3 Relative humidity

Public domain data[10] are used for daily relative humidity.

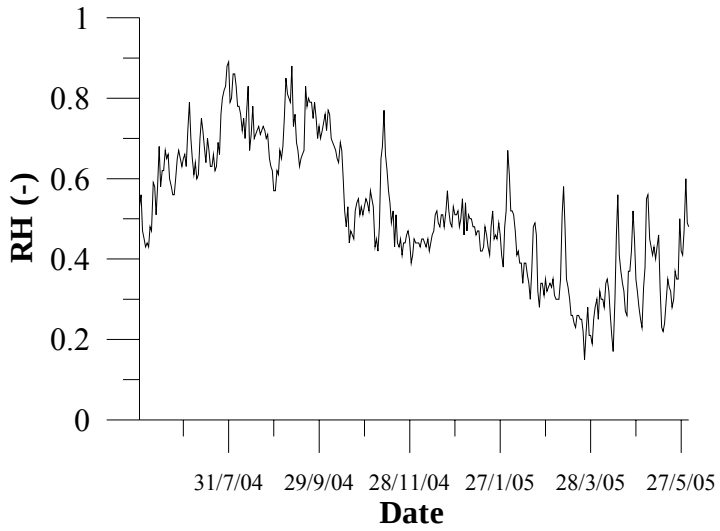


*Figure 43: Average daily relative humidity*

#### 6.5.4.4 Wind speed

Public domain data[10] are used for wind speed.

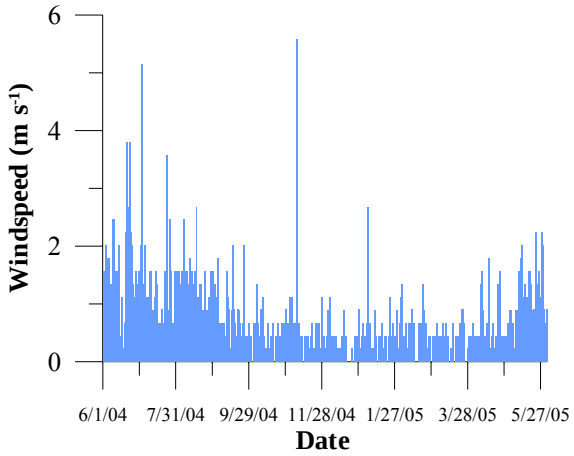


*Figure 44: Average daily windspeed*

#### 6.5.4.5 Precipitation

Because of the spatial variation in precipitation a different approach has been adopted. The TRMM precipitation rasters as described in Chapter 6.4 are used to generated monthly precipitation for each sub basin from October 2004 to September. At the center of each sub basin a virtual meteorological station is generated. The monthly precipitation data are converted to daily values using the following procedure:

- A random day in the month is selected.
- A random amount of precipitation is generated. In the monsoon months (June, July, August, September) this amount is between 30 and 60 mm day$^{-1}$. In all other months this amount is between 10 and 20 mm day$^{-1}$.
- This process is repeated until the total amount of monthly precipitation is distributed.

An example of the daily precipitation of two sub basins is given in Figure 45. Sub basin 57 is located in the Western ghats in the south western part of the catchment and sub basin 61 is located in the eastern part of the catchment.

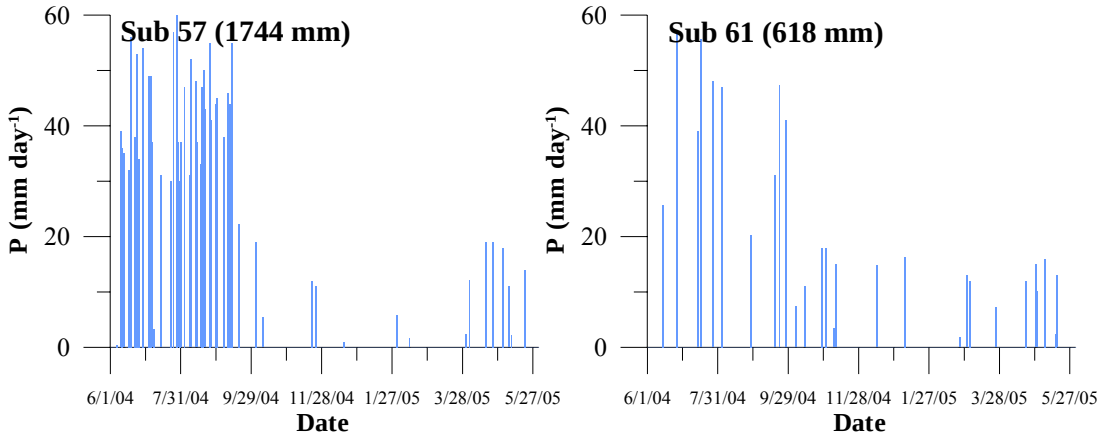


*Figure 45: Daily precipitation for sub basins 57 and 61*

### 6.5.5 Management practices

Quantifying the impact of land management and land use on water supply and quality is a primary focus of environmental modelling. SWAT allows very detailed management information to be incorporated into a simulation. In the model for the Upper Bhima catchment the following operations are used:

- The plant operation initiates plant growth. This operation can be used to designate the time of planting for agricultural crops or the initiation of plant growth in the spring for a land cover that requires several years to reach maturity (forests, orchards, etc.). The plant operation will be performed by SWAT only when no land cover is growing in an HRU. Before planting a new land cover, the previous land cover must be removed with a kill operation or a harvest and kill operation. Information required in the plant operation includes the timing of the operation (month and day or fraction of base zero potential heat units), the total number of heat units required for the land cover to reach maturity, and the specific land cover to be simulated in the HRU.
- The harvest and kill operation stops plant growth in the HRU. The fraction of biomass specified in the land cover's harvest index (in the plant growth database) is removed from the HRU as yield. The remaining fraction of plant biomass is converted to residue on the soil surface.

- The fertilizer operation applies fertilizer or manure to the soil. Information required in the fertilizer operation includes the timing of the operation (month and day or fraction of plant potential heat units), the type of fertilizer/manure applied, the amount of fertilizer/manure applied, and the depth distribution of fertilizer application.
- Application of irrigation water. Information is required on the amount of irrigation water to be applied, the salt content of the irrigation and the timing of the operation.

The agricultural land use classes need to be parameterized for different crops and management activities such as fertilization and irrigation. As described in chapter 6.2 three agricultural land use classes have been defined, which have been parameterized as follows:

*Table 9: management operations rainfed agriculture (AGR1)*

| Date | Crop | Operation | Remarks |
|---|---|---|---|
| Jun-10 | Sorghum | Planting of crop | |
| Jun-22 | Sorghum | Fertilizer application | 300 kg/ha Urea |
| Sep-30 | Sorghum | Harvest | |

*Table 10: management operations supplemental irrigated agriculture (AGR2)*

| Date | Crop | Operation | Remarks |
|---|---|---|---|
| Jun-10 | Sorghum | Planting of crop | |
| Jun-10 | Sorghum | Fertilization | 300 kg/ha Urea |
| Aug-01 | Sorghum | Fertilization | 300 kg/ha Urea |
| Sep-29 | Sorghum | Harvest | |
| Oct-15 | Winter wheat | Planting of crop | |
| Oct-17 | Winter wheat | Fertilization | 300 kg/ha Urea |
| Nov-01 | Winter wheat | Fertilization | 300 kg/ha Urea |
| Nov-10 | Winter wheat | Irrigation | 40 mm |
| Nov-20 | Winter wheat | Irrigation | 40 mm |
| Dec-15 | Winter wheat | Irrigation | 100 mm |
| Jan-15 | Winter wheat | Irrigation | 100 mm |
| Feb-10 | Winter wheat | Fertilization | 300 kg/ha Urea |

*Table 11: management operations intensive irrigated agriculture (AGR3)*

| Date | Crop | Operation | Remarks |
|---|---|---|---|
| Jun-02 | Sugarcane | Planting of crop | |
| Jun-02 | Sugarcane | Fertilization | 300 kg/ha Urea |
| Jun-15 | Sugarcane | Irrigation | 60 mm |
| Jul-15 | Sugarcane | Irrigation | 40 mm |
| Aug-15 | Sugarcane | Irrigation | 50 mm |
| Sep-01 | Sugarcane | Fertilization | 300 kg/ha Urea |
| Sep-15 | Sugarcane | Irrigation | 20 mm |
| Oct-15 | Sugarcane | Irrigation | 50 mm |
| Nov-15 | Sugarcane | Irrigation | 40 mm |
| Dec-15 | Sugarcane | Irrigation | 40 mm |
| Jan-01 | Sugarcane | Fertilization | 300 kg/ha Urea |
| Jan-15 | Sugarcane | Irrigation | 40 mm |
| Feb-15 | Sugarcane | Irrigation | 50 mm |
| Mar-15 | Sugarcane | Irrigation | 100 mm |
| Apr-15 | Sugarcane | Irrigation | 100 mm |
| May-15 | Sugarcane | Irrigation | 100 mm |
| May-30 | Sugarcane | Harvest | |

### 6.5.6 Reservoirs

The upper Bhima catchment is a complex catchment and stream flow is for a large part determined by reservoirs in the upstream area of the catchment which receives most precipitation. Data on reservoirs is scarce and sensitive given the water disputes between the different states. A total of 13 reservoirs have been modeled in SWAT. The actual reservoirs and the locations of the reservoirs in the model are shown in Figure 46. SWAT locates the reservoirs for routing purposes on the sub basin boundary. In the model a user specified release rate is used to model outflow out of the reservoir. Besides monthly releases the following inputs are required for each reservoir:

- RES_ESA: Surface area of the reservoir when filled to the emergency spillway (ha)
- RES_PSA: Surface area of the reservoir when filled to the principal spillway (ha)
- RES_EVOL: Volume of water held in the reservoir when filled to the emergency spillway ($10^4$ $m^3$ $H_2O$)
- RES_PVOL: Volume of water held in the reservoir when filled to the principal spillway ($10^4$ $m^3$ $H_2O$)
- RES_VOL: Initial Volume of water held in the reservoir when filled at the beginning of the simulation ($10^4$ $m^3$ $H_2O$)

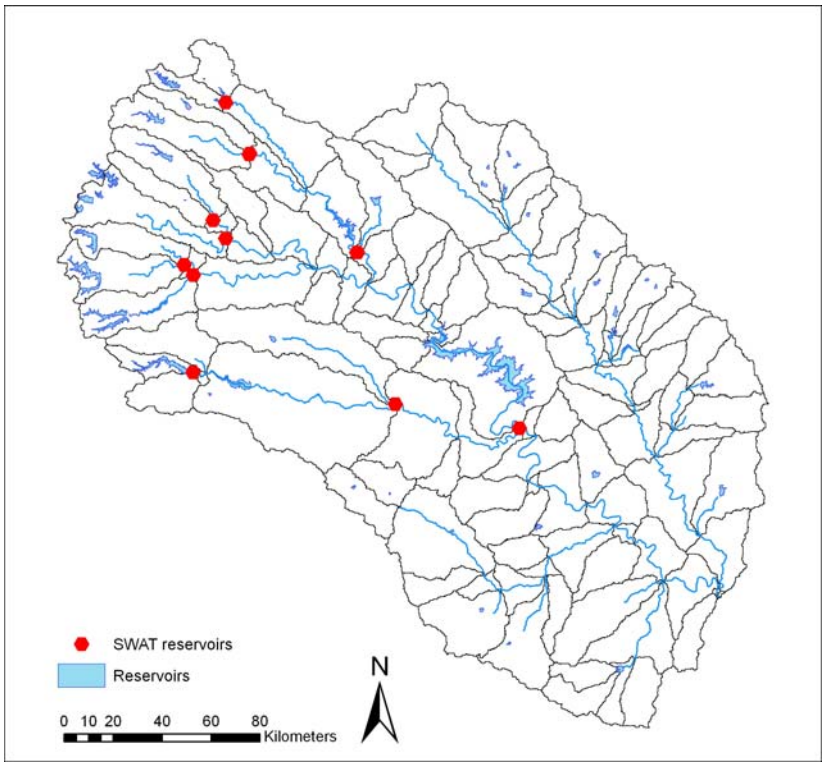


*Figure 46: Location of reservoirs*

For modelling purposes the reservoirs are grouped together into two reservoirs; one for the Ujani branch in the middle and one for the Bhatghar branch in the south. It is assumed that all areas with AGR3 land use receive their irrigation water directly from the reservoirs. The irrigation year 2004-2005 is an average year and it is assumed that the irrigation amounts specified in

Table 11 are actually required. The required stream flows to fulfil these irrigation requirements for both branches are shown in Figure 47.

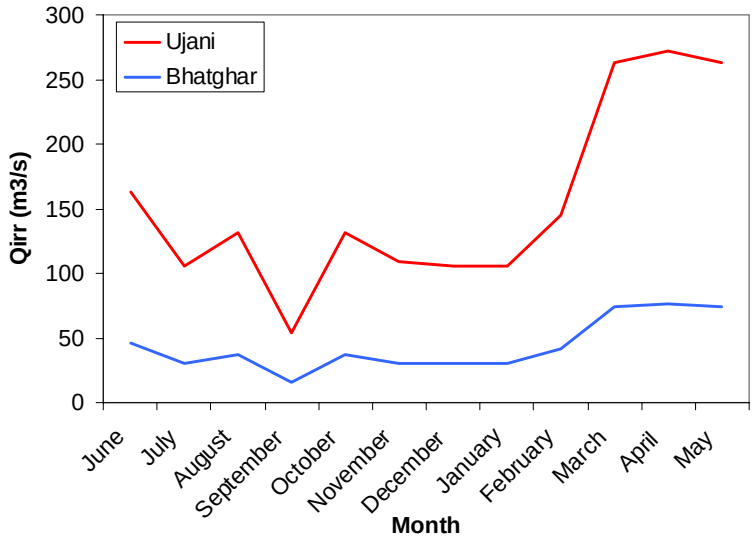


*Figure 47: Stream requirements to fullfill irrigation requirements*

The difference between the amount of water that flows into the reservoirs and the amount that is required for irrigation is released as stream flow to downstream basins. The distribution across the different months is based on the historical monthly stream flow distribution presented in.

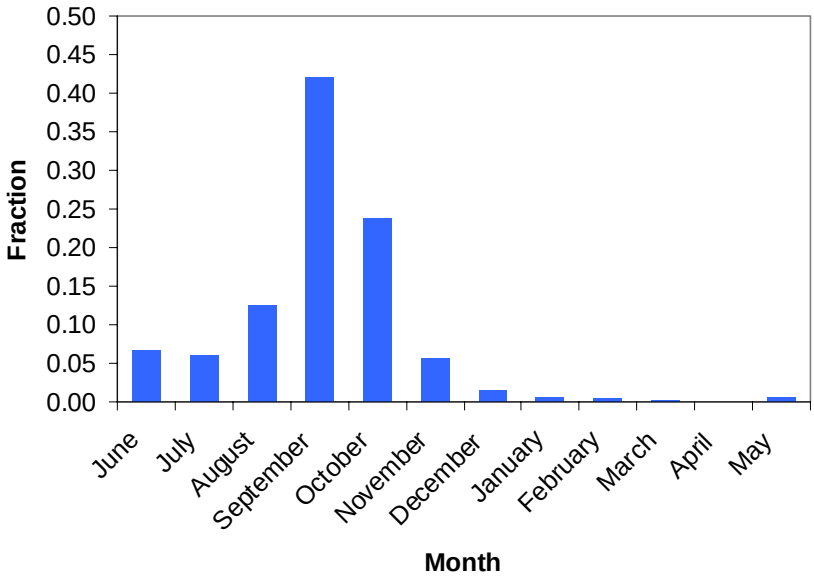


*Figure 48: Monthly fractions of annual streamflow*

## 6.6 Calibration

Major objective of the project is to use the spatial patterns of ET in the auto calibration of the SWAT model. The model independent parameter estimation package PEST will be used for this purpose (Doherty, 2004).

The purpose of PEST (which is an acronym for Parameter ESTimation) is to assist in data interpretation, model calibration and predictive analysis. Where model parameters and/or excitations need to be adjusted until model-generated numbers fit a set of observations as closely as possible then, provided certain continuity conditions are met, PEST should be able to do the job. PEST will adjust model parameters and/or excitations until the fit between model outputs and laboratory or field observations is optimised in the weighted least squares sense. Where parameter values inferred through this process are nonunique, PEST will analyse the repercussions of this non-uniqueness on predictions made by the model.

The first step in setting up PEST is however to define a logical set of parameters and observation which are to be used in the optimization. Using a spatial set-up results in a number of new challenges. The SEBAL analysis provides an eight month time series with a biweekly time step of both reference and actual ET. SWAT provides a 12 month monthly time series of reference ET ($ET_{ref}$) and actual ET ($ET_{act}$) per HRU. The parameter optimization is performed on actual ET. The SEBAL data are first aggregated to monthly data and summarized per HRU in order to be able to directly compare model outputs to the SEBAL analysis.

For more details and a discussion of results reference is made to the two scientific papers attached in annex 1 and annex 2.

# 7 Cost benefit analysis

The project will be the base to generate substantial other projects, both research oriented as well as commercial. As first concrete follow-ups of this project FutureWater has recently submitted a number of proposals that are in line with the methodology developed in this project:

- A proposal in the framework of the "Pre-kwalificatie ESA programma's (PEP)". The evapotranspiration based approach has been extended to satellite remote sensing of precipitation and groundwater using gravity measurements. This hydrological triangle is then linked to a modelling framework similar to what has been achieved in this project.
- Two proposals in the framework of the "Partners for Water" program. One proposal is focusing on the integration of Remote Sensing and a water allocation model in China and a second proposal focuses on the integration of Remote Sensing, models and an economic approach in Ghana to promote water savings.

It should be emphasised that the subject of this research, water, is a fast growing market. On a global scale it is estimated that investments in the water sector for the developing world will more than double from US$ 75 billion per year currently to US$ 180 billion per year in 2025 (The World Water Council). Similar estimates at a global scale are US$ 5,000 billion per year currently and an annul growth rate of 11%.

More concrete, an economic analysis has been done to assess the benefits that will emerge from the current project on a five years forecast as a direct result of this project.

| | 2008 | 2009 | 2010 | 2011 | 2012 |
|---|---|---|---|---|---|
| Growth in turnover (€ x 1000) | 40 | 100 | 100 | 100 | 80 |
| Growth in profit (40%) (€ x 1000) | 16 | 40 | 40 | 40 | 32 |

On top of the NIVR GO subsidy FutureWater has invested a total of nearly 70 k€ in personnel costs in the current project and we anticipate an additional 30 k€ investment for marketing the approach. The total investment then equals 100 k€ and the return on investment is approximately 3 years. This could be accelerated if the above described proposals would be granted.

# 8 Conclusions and outlook

A unique operational product that integrates Remote Sensing and hydrological modelling with great potential for applications in similar data scarce basins in the world has been developed in this project. Taking into account the anticipated growth in investments in the water sector and the need for strategic decision support systems in data poor environments, it is concluded that FutureWater will greatly enhance its business potential. IWMI as a project partner will apply the approach, not only in India, but in modelling projects across the world. FutureWater considers the project as a great success and important for the future.

The publication of the approach in international scientific journals as well as a more accessible project website (http://www.futurewater.nl/krishna) will market the approach to the scientific community as well as stakeholder working in practical water management.

FutureWater intends to further expand this field of work. The current project has been limited to Remote Sensing of evapotranspiration and precipitation. This could be further extended by including data from gravity satellites that enable measurement of changes in groundwater. It is anticipated that an inclusion of both evapotranspiration and groundwater in the calibration algorithm further reduces uncertainty and improves insight in the most important hydrological processes.

# 9 References


Allen, R.G., Howell, T.A., Pruitt, W.O., Walter, I.A. and Jensen, M.E. (eds), 1991, Lysimeters for evapotranspiration and environmental measurements. ASCE, New York, USA, pp 444.

Allen, R., Pereira, L.A., Raes, D., Smith, M., 1998, Crop evapotranspiration; guidelines for computing crop water requirements, FAO Irrigation and Drainage Paper No. 56, FAO, Rome

BASINS, 2006. BASINS, Better Assessment Science Integrating Point and Nonpoint Sources. http://www.epa.gov/waterscience/basins/index.html

Bastiaanssen, W.G.M., M. Menenti, R.A. Feddes and A.A.M. Holtslag, 1998. The Surface Energy Balance Algorithm for Land (SEBAL): Part 1 formulation, J. of Hydr. 212-213: 198-212

Bastiaanssen, W., Klaasse, A., Zwart, S., Immerzeel, W. and Droogers, P., 2006, The hydrological flow path and options for sustainable water resources management in the overexploited Rio Bravo Basin; A preliminary analysis from remote sensing and hydrological modeling, WaterWatch report, Wageningen

Bowen, I.S., 1926, The ratio of heat losses by conduction and by evaporation from any water surface, Phys. Rev., Springer Verlag, 383-414

Brutsaert, W. (1982) Evaporation into the atmosphere. D. Reidel Publishing Co., Dordrecht, The Netherlands, pp 300.

Brutsaert, W. and M. Sugita, 1992. Application of self preservation in the diurnal evolution of the surface energy balance budget to determine daily evaporation, J. Geophys. Res. 97(D17): 18377-18362

Burnash, R.J.E., Ferral. R.L. & McGuire, R.A. (1973)..A Generalised Streamflow Simulation System, Joint Federal-State River Forecast Center, Sacramento, California.

CAMASE. 2005. Agro-ecosystems models. http://library.wur.nl/camase/

Choudhury, B.J., 1997. Estimating land surface evaporation using multispectral satellite and ancillary data. In: Kite, G.W., Pietroniro, A., Pultz, T. (Eds.), Applications of Remote Sensing in Hydrology, Proc. Symp. No 17, NHRI, Saskatoon, Canada.

Choudhury, B.J., 2000. Seasonal and interannual variations of total evaporation and their relations with precipitation, net radiation, and net carbon accumulation for the Gediz Basin area. J. Hydrol. 229 (1/2), 77–86.

Choudhury, B.J., DiGirolamo, N.E., 1998. A biophysical processbased estimate of global land surface evaporation using satellite and ancillary data. I. Model description and comparison with observations. J. Hydrol. 205, 164–185.

Courault, D., Seguin, B. and Olioso, A., 2005, Review on estimation of evapotranspiration from Remote Sensing data: From empirical to numerical modelling approaches, Irrigation and Drainage Systems, 19, 223-249

Cosgrove, W.J.; and F.R. Rijsberman. 2000. *World Water Vision: Making water everybody's business*. London, UK: Earthscan..

Crago, R.D., 1996. Conservation and variability of the evaporative fraction during the daytime, J. of Hydr. 180: 173-194

Crawford, N.H. and R.K. Linsley. 1966. Digital Simulation in Hydrology: Stanford Watershed Model IV, Stanford Univ., Dept. Civ. Eng. Tech. Rep. 39, 1966.

De Bruin, H.A.R., van den Hurk, B.J.J.M., Kohsiek, W., 1995. The scintillation method tested over a dry vineyard area. Boundary-Layer Meteorol. 76, 25–40.

DeSmedt, F. Y.B. Liu and S. Gebremeskel. 2005. Integrated modelling of hydrological processes on basin scale. Department of Hydrology and Hydraulic Engineering, Vrije Universiteit Brussel.

Douglas, J.R., R.T. Clarke, S.G. Newton. 1975..The use of likelihood functions to fit conceptual models with more than one dependent variable. Journal of Hydrology, Vol. 29: 181-198

Droogers, P., and W.G.M. Bastiaanssen. 2001. Combining remote sensing and hydrological models to enhance spatial and temporal variability. Remote Sensing and Hydrology 2000. (Proceedings of a symposium held at Santa Fe, New Mexico, USA, April 2000). IAHS Red Books 267: 574–579.

Duan, Q., Sorooshian, S. and Gupta, V., 1992, Effective and Efficient Global Optimisation for Conceptual Rainfall-Runoff Models, Water Resources Research, Vol. 28, No. 4, pages 1015-1031.

Duan, Q., Sorooshian, S. and Gupta, V., 1993, a Shuffled Complex Evolution Approach for Effective and Efficient Optimisation, Journal of Optimisation Theory Application, Vol. 76, No. 3, pages 501-521.

Duan, Q., Sorooshian, S. and Gupta, V., 1994, Optimal Use of the SCE-UA Global Optimisation Method for Calibrating Watershed Models, Journal of Hydrology, No. 158, pages 265-284.

Duan, Q. H. V. Gupta, S. Sorooshian, A.N. Rousseau, and R. Turcotte. 2003. Calibration of watershed models. Water Science and Applications Series Volume 6. American Geophysical Union.

DMIP. 2002. Distributed Model Intercomparison Project. http://www.nws.noaa.gov/oh/hrl/dmip/

EPA. 2006. Environmental Protection Agency, Information Sources. http://www.epa.gov/epahome/models.htm

Farah, H.O., 2001. Estimation of regional evaporation under different weather conditions from satellite and meteorological data, Ph.D. thesis, Department of Agrohydrology, Wageningen University, The Netherlands: 170 pp.

FAO, 1974. FAO-Unesco Soil Map of the World, 1:5.000.000. Unesco, Paris.

FAO, 1995. FAO-Unesco digital Soil Map of the World and derived soil properties, 1:5.000.000. Unesco, Paris.

Gieske, A., 2003, Operational solution for actual evapotranspiration, in: Understanding Water in a Dry Environment: Hydrological Processes in Arid and Semi-arid zones, ed. Simmers, I., Balkema Publishers, the Netherlands

GLOBE. 2006. Global optimization tool GLOBE. http://www.unesco-ihe.org/hi/sol/global.htm

Granger, R.J., 1989. Evaporation from natural nonsaturated surfaces. J. Hydrol. 111, 21–29.

Granger, R.J., Gray, D.M., 1990. A net radiation model for calculating daily snowmelt in open environments. Nordic Hydrol. 21, 217–234.

Granger, R.J., 1995. A feedback approach for the estimate of evapotranspiration using remotely-sensed data. In: Kite, G.W., Pietroniro, A., Pultz, T.J. (Eds.), Application of remote sensing in hydrology (Proceedings of the Second International Workshop, NHRI Symposium No. 14, Saskatoon, October 18–19, 1994, NHRI, pp. 211–222.

Granger, R.J., 1997. Comparison of surface and satellite-derived estimates of evapotranspiration using a feedback algorithm. In: Kite, G.W., Pietroniro, A., Pultz, T.J. (Eds.), Application of remote sensing in hydrology. Proceedings of the Third International Workshop, NHRI Symposium No. 17, October, 1996; NASA, Goddard Space Flight Center, Greenbelt, MD, NHRI, pp. 71–81.

Doherty, J., 2004, PEST; Model-Independent Parameter Estimation; User Manual: 5th edition. Watermark Numerical Computing

Franke R. 1982. Smooth Interpolation of Scattered Data by Local Thin Plate Splines. Comp. & Maths. with Appls. 8: 237-281.

Hargreaves, G.L., G.H. Hargreaves, and J.P. Riley. 1985. Agricultural benefits for Senegal River Basin. J. Irrig. and Drain. Engr. 111(2):113-124.

Hooghoudt, S.B. 1940. Bijdrage tot de kennis van enige natuurkundige grootheden van de grond. Versl. Landbouwkd. Onderz. 46: 515-707.

Hoffmann L, El Idrissi A, Pfister L, Hingray B, Guex F, Musy A, Humbert J, Drogue G, Leviandier T., Development of regionalized hydrological models in an area with short hydrological observation series, River Research and Applications 20(3), 243-254, 2004.

Hogue, T.S., S. Sorooshian, H. Gupta, A. Holz, D. Braatz. 2000. A Multistep Automatic Calibration Scheme for River Forecasting Models. Journal of Hydrometeorology: Vol. 1, No. 6, pp. 524–542.

Immerzeel, W.W. and Droogers, P., 2005, Exploring evaporation reduction in the Hai basin; analysis using the SWAT model, FutureWater report, Wageningen

Ines, A.V.M., and Droogers, P., 2002. Inverse modeling in estimating soil hydraulicfunctions: a Genetic Algorithm approach. Hydrology and Earth System Sciences 6:49-65.

IRRISOFT. 2000. Database on IRRIGATION & HYDROLOGY SOFTWARE. http://www.wiz.uni-kassel.de/kww/irrisoft/irrisoft_i.html#index

IWMC. 2002. Water quality model comparison chart. Illinois Watershed Management Clearinghouse. http://web.aces.uiuc.edu/watershed/model/COMPARE.HTM

Jackson, R.B., Carpenter, S.R., Dahm, C.N., McKnight, D.M., Naiman, R.J., Postel, S.L., and Running, S.W., 2001. Water in a changing world. Ecological Applications 11, 1027-1045.

Kite, G.W. and Droogers, P., 2000, Comparing evapotranspiration estimates from satellites, hydrological models and field data, Journal of Hydrology, 229, 3-18

Koyama, O. 1998. *Projecting the future world food situation*. Japan International Research Center for Agricultural Sciences Newsletter 15.

Lagouarde, J.-P. 1991. Use of NOAA-AVHRR data combined with an agrometeorological model for evaporation mapping. International Journal of Remote Sensing 12: 1853–1864.

Lillesand, T.M. and Kiefer, R.W., 2000, Remote Sensing and Image Interpretation, 4th edition, John Wiley & Sons, New York

Lipiwattanakarn, S., N. Sriwongsitanon and S. Saengsawang. 2006. Performance Comparison of a Conceptual Hydrological Model and a Back-propagation Neural Network Model in Rainfall-Runoff Modeling. Department of Water Resources Engineering, Faculty of Engineering, Kasetsart University, Bangkok, Thailand.

Linsley, R.K. 1976. Why Simulation? Hydrocomp Simulation Network Newsletter, Vol: 8-5. http://www.hydrocomp.com/whysim.html

Lyall and Macoun Consulting Engineers (1986).. *WARAS Reference Manual, Version 1.0*, prepared for the former Department of Water Resources, NSW..

Madsen, H. and T. Jacobsen. 2001. Automatic calibration of the MIKE SHE integrated hydrological modelling system. *In*: 4th DHI Software Conference, 6-8 June, 2001, Scanticon Conference Centre, Helsingør, Denmark.

McCuen, R.H. 1973. The role of sensitivity analysis in hydrologic modeling. Journal of Hydrology, Volume 18: 37-53.

Meijer, F., M. Jaarsma, R. Loeve, P. Droogers. 2004. Flexible weirs to retaining water. (In Dutch). H2O 12:24-27.

Menenti, M. and Choudhury, B.J. 1993. Parametrization of land surface evapotranspiration using a location dependent potential evapotranspiration and surface temperature range. In: Bolle H.J. et al. (Eds.), Exchange Processes at the Land Surface for a Range of Space and Time Scales, IAHS Publication. vol. 212, pp. 561–568.

Monin, A.S., and A.M. Obukov, 1954. Basic laws of turbulent mixing in the atmosphere near the ground. Tr. Akad. Nauk SSSR Geoph. Inst., No. 24(151), 1963-1987.

Monteith, J.L., 1965, Evaporation and environment, Sym. Soc. Exp. Biol., 19, 205-234

MRC, Mekong River Commission. 2000. Review of Available Models. Water Utilisation Project Component

Nash, J. E., and J. V. Sutcliffe, 1970: River flow forecasting through conceptual models, 1, a discussion of principles. J. Hydrol., 10(3), 282-290.

Neitsch, S.L., J.G. Arnold, J.R. Kini , J.R. W Lliams, K.W. King. 2002. Soil And Water Assessment Tool, Theoretical Documentation,Version 2000. Texas Water Resources Institute, College Station, Report TR-191

Nicols, W.E. and R.H. Cuenca, 1993. Evaluation of the evaporative fraction for the parameterization of

the surface energy balance, Water Resources Research 29(11): 3681-3690 NOAA National Weather Service, West Gulf River Forecats Center.

NWCC. 2006. Water Management Models. http://www.wcc.nrcs.usda.gov/nrcsirrig/irrig-mgt-models.html

Penman, H.L., 1948, Natural evaporation from open water, bare soil and grass, Proc. Roy. Soc., A, 193, 120-146.

Prata, A.J., Platt, C.M.R., 1991. Land surface temperature measurements from the AVHRR, Proceedings of the Fifth AVHRR Data Users' Meeting. Tromso, Norway, 25–28 June 1991, pp. 433– 438.

Priestley, C.H.B. and R.J. Taylor. 1972. On the assessment of surface heat flux and evaporation using large-scale parameters. Mon. Weather Rev. 100:81-92.

Rao, A. R., and Han, J. 1987. Analysis of objective functions used in urban runoff models. Adv. Water Resour., 10, 205–211.

Reed, S., Koren, V., Smith, M., Zhang, Z., Moreda, F., Seo, D.J. 2004. Overall distributed model intercomparison project results. Journal of Hydrology, Volume 298, Issue 1-4: 27-60.

REM. 2006. Register of Ecological Models (REM). http://www.wiz.uni-kassel.de/ecobas.html

Riou, C., Itier, B. & Seguin, B. 1988. The influence of surface roughness on the simplified relationship between daily evaporation and surface temperature. International Journal of Remote Sensing 9(9): 1529–1533.

Ritchie, J.T. 1972. A model for predicting evaporation from a row crop with incomplete cover. Water Resour. Res. 8:1204-1213.

Roerink, G.J., Su, B. & Menenti, M. 2000. S-SEBI A simple remote sensing algorithm to estimate the surface energy balance. Physics Chim Earth (B) 25(2): 147–157.

Seckler, D.; R. Barker; and U. Amarasinghe. 1999. Water scarcity in the twenty-first century. *Water Resources Development* 15: 29-42.

Servat, E., and Dezetter, A. 1991. Selection of calibration objective functions in the context of rainfall-runoff modeling in a Sudanese savannah area. Hydrol. Sci. J., 6: 307–330.

Seguin, B. & Itier, B. 1983. Using midday surface temperature to estimate daily evaporation from satellite thermal IR data. International Journal of Remote Sensing 4: 371–383.

Shuttleworth, W.J., R.J. Gurney, A.Y. Hsu and J.P. Ormsby, 1989. FIFE: the variation in energy partitioning at surface flux sites, IAHS Publ. 186: 67-74

Singh, J., H.V. Knapp, J.G. Arnold, M. Demissie. 2005. Hydrological modeling of the Iroquois river watershed using HSPF and SWAT. Journal of the American Water Resources Association. Volume 41, Number 2, April 2005, pages 343-360.

Sivapalani M, Takeuchi K, Frank SW, Gupta VK, Karambiris H, Lakshmi V, Liang X, McDonell JJ, Mendiondo, EM, O'Conell PE, Oki T, Pomeroy JW, Schertzer D, Uhlenbrook S, Zehe E. 2003. IAHS Decade on Predictions in Ungauged Basins (PUB), 2003–2012: Shaping an exciting future for the hydrological sciences. Hydrological Sciences 48: 857-880

Skahill BE, Doherty J. 2006. Efficient accommodation of local minima in watershed model calibration. Journal of Hydrology (in press).

SMIG. 2006a. Surface-water quality and flow modeling interest group. http://smig.usgs.gov/SMIG/SMIG.html

Skahill, B.E., J. Doherty. 2006. Efficient accommodation of local minima in watershed model calibration. Journal of Hydrology (in press).

Smedema, L.K. and D.W. Rycroft. 1983. Land drainage—planning and design of agricultural drainage systems, Cornell University Press, Ithica, N.Y.

SMIG. 2006b. Archives of Models and Modeling Tools. http://smig.usgs.gov/SMIG/model_archives.html

Solomatine. D.P. 1998. Genetic and other global optimization algorithms - comparison and use in calibration problems. Proc. 3rd Intern. Conference on Hydroinformatics, Copenhagen, Denmark, 1998. Balkema Publishers. pp.1021-1028

Solomatine, D.P. (1999). Two strategies of adaptive cluster covering with descent and their comparison to other algorithms. Journal of Global Optimization, 1999, vol. 14, No. 1, pp. 55-78.

Sorooshian, S., and Gupta V. K. 1995. Chapter 2: Model calibration. Computer models of watershed hydrology, V. P. Singh, ed., Water Resources Publications, Littleton, Colorado: 23–68.

Su, Z. 2002. The surface energy balance system (SEBS) for estimation of turbulent heat fluxes. Hydrology and Earth System Sciences 6: 85–99.

Sugita, M. and Brutsaert, W. (1990) Regional surface fluxes from remotely sensed skin temperature and lower boundary layer measurements. Water Resources Research, 26, 2937-2944.

TNRCC, Texas Natural Resource Conservation Commission. 1998. An Evaluation of Existing Water Availability Models. Technical Paper #2. http://www.tnrcc.state.tx.us/permitting/waterperm/wrpa/wam.html

Tolson, B.A., Schoemaker, C.A. 2005. Comparison of optimization algorithms for the automatic calibration of SWAT2000. In:.Karim Abbaspour and Raghavan Srinivasan, (ed.) 3rd International SWAT Conference July 11-15 2005, Zürich, Switzerland.

Tucker, C.J., 1979, Red and photographic infrared linear combination for monitoring vegetation. Remote Sensing of Environment, 8, 127-150

United Nations. 1997. Comprehensive Assessment of the Freshwater Resources of the World (overview document) World Meteorological Organization, Geneva.

USBR. 2002. Hydrologic Modeling Inventory. http://www.usbr.gov/pmts/rivers/hmi/2002hmi/index.html

USGS. 2006. Water Resources Applications Software. http://water.usgs.gov/software/

Verhoef, A., De Bruin, H.A.R., and Van den Hurk, B.J.J.M. (1997) Some practical notes on the parameter kB-1 for sparse vegetation. J. Appl. Meteor., 36, 560-572.

Vijay P. Singh, V.P., and D.A. Woolhiser. 2002. Mathematical Modeling of Watershed Hydrology. Journal of Hydrologic Engineering, Vol. 7, No. 4, 270-292.

Xu, Chong-yu. 2002. Hydrological Models. Uppsala University Department of Earth Sciences Hydrology

# Annex 1: Paper Hydrological Processes

# Spatial calibration of a distributed hydrological model using Remote Sensing derived evapotranspiration in the Upper Bhima catchment, India.

| | |
|---|---|
| Journal: | *Hydrological Processes* |
| Manuscript ID: | HYP-06-0321.R1 |
| Wiley - Manuscript type: | Research Article |
| Date Submitted by the Author: | n/a |
| Complete List of Authors: | Immerzeel, Walter; FutureWater, FutureWater<br>Droogers, Peter; FutureWater, FutureWater |
| Keywords: | Evapotranspiration, Hydrological Model, Optimisation, Calibration, SWAT |
| | |

## Abstract

Calibrating spatially distributed hydrological models is complex due to the lack of reliable data, uncertainty in representing the physical features of a river catchment, and the implementation of hydrological processes in a simulation model. In this paper, an innovative approach is presented which incorporates Remote Sensing derived evapotranspiration in the calibration of the Soil and Water Assessment Tool (SWAT). The Gauss–Marquardt–Levenberg algorithm is implemented to optimise different combination of land use, soil, groundwater, and meteorological model parameters. In the best performing optimisation, the $r^2$ between monthly sub-basin simulated and measured actual evapotranspiration ($ET_{act}$) was increased from 0.40 to 0.81. $ET_{act}$ was more sensitive to the groundwater and meteorological parameters than the soil and land use parameters. Traditional calibration on a limited number of discharge stations lumps all hydrological processes together and chances on the equifinality problem are larger. In this study we have shown this problem can be constrained by using spatially distributed observations with a monthly temporal resolution. The success of the approach is entailed into the spatial and temporal isolation of the calibration problem. At a spatial resolution below the sub-basin level further study is required to fine-tune the calibration procedure.


**Key words:** Evapotranspiration; Hydrological Model; Optimisation; Calibration; SWAT

## 1 Introduction

Calibration of physically based, distributed hydrological models is complex given limitations of the input data, complexity of the mathematical representation of hydrological processes, and incomplete knowledge of basin characteristics. A priori, it is not clear whether a unique set of model parameters exists for a given catchment. While comparing model outputs to observations the main question is what the causes of these differences are (Duan *et al*., 2003)? Model calibration is usually based on the comparison between modelled and observed hydrographs for a limited number of locations and a small number of input parameters are varied in a trial and error mode to achieve a desired response (Gupta *et al*., 1998; Anderston *et al.*, 2002). In a complex distributed hydrological model with numerous parameters with a high spatial and temporal heterogeneity this approach can be cumbersome. To overcome these difficulties a number of different auto-calibration or parameter optimisation methods have been developed that deploy a systematic approach to parameter estimation.

The type of optimisation algorithm applied is the dominant distinguishing factor in parameter estimation (Singh and Woolhiser, 2002).The objective function describes the difference between the observed and model simulated values. RMSE statistics and the Nash-Sutcliffe criterion (Nash and Sutcliffe, 1970) are amongst the most commonly used. Minimizing the objective function is complex; because most discharge based objective functions in distributed hydrological models have multiple extremes. Optimisation algorithms adopt either a gradient (Levenberg (1944); Marquard (1963)) or a global search method such as the shuffled complex evolution algorithm (Kuczera, 1997) and

genetic algorithms (Wang, 1991). Global optimisation algorithms are designed for locating the global optimum. Local search algorithms have been criticized for getting trapped in local minima. The most important advantage of a local search is nonetheless its efficiency; e.g., the number of model calls required to find the optimum set of parameters. Skahill and Doherty (2006) show how the algorithms underlying the Gauss–Marquardt–Levenberg (GML) method of computer-based parameter estimation can be improved to enhance the possibility to find the global minimum while retaining the model run efficiency.

Using a limited number of discharge stations in the optimisation may well lead to the equifinality problem; e.g., there are more than one parameter combination leading to similar results (Beven, 1993; Beven, 2000; Beven, 2001; Beven and Freer, 2001; Beven 2006; Franks *et al*, 1997). High spatial heterogeneity in combination with a large number of model parameters inhibits the identification of one set of parameters describing the natural system. If river discharges in a catchment are mainly governed by human decisions (e.g., dams and reservoirs) they may not be usable in determining the natural characteristics of the system. Hydrological parameters measured using Remote Sensing, which has a high spatial and temporal observational resolution, could provide a suitable solution in this respect. Measuring hydrological parameters such as evapotranspiration and soil moisture using Remote Sensing is a growing field of research (Bastiaanssen *et al.*, 1998; Hall *et al.*, 1992; Kite and Droogers, 2000; Su, 2000). The use of Remote Sensing in the parameterisation of hydrological models is an even newer field; Wood (1995) empirically evaluates scale issues using Remote Sensing data and a hydrological model. Other studies use Remote Sensing to parameterise hydrological models (Boegha

*et al.,* 2004; Houser *et al.*, 1998; Kite and Pietroniro, 1996; Shuttleworth, 1998). Less work has been done in the use of Remote Sensing in the actual calibration using optimisation algorithms of hydrological models. Campo *et al.* (2006) show the use of Remote Sensing derived soil moisture in the calibration of a distributed hydrological model using a local search algorithm developed by Nelder and Mead (1965).

In summary five partially overlapping fields of expertise can be identified that deal with the topic of this study: (i) deriving hydrological fluxes by Remote Sensing, (ii) optimisation algorithms used in calibration of simulation models, (iii) equifinality in parameter optimisation, (iv) use of Remote Sensing in parameterisation of hydrological models and (v) the use of Remote Sensing in the calibration of hydrological models in data scarce areas. Evidently not all topics can be extensively covered and the focus of this was on the latter. The objective was to evaluate the method of using Remote Sensing derived actual evapotranspiration ($ET_{act}$), based on the Surface Energy BALance algorithm (SEBAL; Bastiaanssen *et al*., 1998), to calibrate the process-based hydrological model Soil and Water Assessment Tool (SWAT; Arnold *et al.*, 1998), in the water scarce Upper Bhima catchment in southern India. The Parameter ESTimation (PEST) software (Doherty, 2005), incorporating the gradient search GML optimisation method, was used for this purpose.

## 2 Study area

The Upper Bhima catchment (45,678 $km^2$) is located in the upstream part of the Krishna basin in southern India and originates in the Western Ghat mountains and covers part of the Maharasthra state (Figure 1). The catchment is located between 16.5°-19.5 ° latitude and 73.0° -76.5° longitude. The elevation ranges from 414 meter in the east to 1458 meter in the Western Ghat mountains and 95% of the catchment is below 800 meter and relatively flat. The average slope of the catchment is 2%.

The catchment has two main tributaries, the Sina River which drains the north eastern part and the Bhima River which drains the remainder. The catchment is an important source of water for the entire Krishna basin as a major part of the precipitation falls in the Western Ghat range in the east of the catchment and is retained and released to downstream areas through an intricate set of reservoirs, especially along the Bhima tributary. Flows in the rivers are, therefore, mainly human controlled and respond less directly to variations in the climate excitations and biophysical conditions and are hence less suitable to use for calibration. The reservoirs accumulate water during the monsoon season (June to September), and this is gradually released throughout the irrigation season (October to May).

The catchment has a highly diverse climate mainly caused by the interaction between the monsoon and the Western Ghat mountain range (Gunnel, 1997). The precipitation ranges from less than 600 mm in the eastern part of the basin to over 1800 mm in the mountains in the west with an average of 941 mm during the averagely wet irrigation year 2004-2005 (Figure 1). Figure 2 shows the monthly precipitation (P) and reference

evapotranspiration ($ET_{ref}$) in the basin. $ET_{ref}$ is calculated using Penman-Monteith (Monteith, 1965) and alfalfa as reference crop. The catchment has a high annual $ET_{ref}$ (1814 mm) ranging from 224 mm/month in May to 108 mm/month in December. More than 75% of the annual precipitation occurs during the monsoon. Between October and May, large precipitation deficits occur with the peak in May (179 mm) just before the onset of the monsoon.

The state of Maharasthra has a diverse cropping pattern characterized by cultivation of sugarcane, sorghum, wheat, corn, millet, groundnut, grass fodder, and a variety of horticultural crops (Neena, 1998). Three main types of agricultural systems were identified in the catchment: (i) rain fed agriculture with a single crop (e.g. sorghum) cultivated during the monsoon, (ii) supplemental irrigated agriculture with one rain fed crop during the monsoon (e.g. sorghum) and a (groundwater) irrigated crop planted in October and harvested in February (e.g. winter wheat) and (iii) irrigated perennial sugarcane which has a growing period of 11 months and which is grown throughout the year and irrigated from water released by the reservoir system. Other natural land covers include rangelands, mixed forests, evergreen forests and water surfaces.

## 3 Methods

### *SEBAL*

The Surface Energy Balance Algorithm for Land (SEBAL) formulated by Bastiaanssen et al. (1998) was used to calculate bi-weekly $ET_{act}$ from October 2004 to May 2005. Spectral radiances in the visible, near-infrared, and thermal infrared part of the spectrum derived from 16 MODIS satellite images were used. Two cloud free images were selected each month and the MOD02HKM product was used in the analysis. This Level 1B product contains calibrated and geolocated radiances for MODIS spectral bands 1 through 7 at 250 (band 1 and 3) and 500m (band 3 to 7) resolution. The thermal band is downscaled and the final resolution of the $ET_{act}$ images is 250 meter. The acquisition dates and overpass time are shown in Table 1.

SEBAL converts satellite radiances into land surface characteristics such as surface albedo, leaf area index, vegetation index, and surface temperature, which were used in solving the instantaneous energy budget equation given by

$$L_v E = Q^* - G_0 - H \qquad (1.)$$

Where $L_vE$ is the latent heat flux (W m-2), Q* is the net radiation flux at the surface (W/m2), $G_0$ is the soil heat flux (W/m2), and H is the sensible heat flux to the air (W/m2). The net radiation (Q*) was computed by subtracting all outgoing radiant fluxes from all incoming radiant fluxes according to

$$Q^* = Q_{s\downarrow} - \alpha Q_{s\downarrow} + Q_{L\downarrow} - Q_{L\uparrow} - (1-\varepsilon_0)Q_{L\downarrow} \qquad (2.)$$

Where $Q_{s\downarrow}$ is the incoming short-wave radiation (W/m2), $\alpha$ is the surface albedo (dimensionless), $Q_{L\downarrow}$ is the incoming long wave radiation (W/m2), $Q_{L\uparrow}$ is the outgoing long wave radiation (W/m2), and $\varepsilon_o$ is the surface thermal emissivity (dimensionless). In Eq. 2, the amount of net short-wave radiation ($Q_{S\downarrow}$ - $\alpha$ $Q_{S\downarrow}$) that remains available at the surface is a function of the surface albedo ($\alpha$). The broad band surface albedo $\alpha$ was derived from the narrow band spectral reflectances $\alpha$ ($\lambda$) measured by each MODIS satellite band (Zhong and Li, 1988). The incoming short-wave radiation ($Q_{S\downarrow}$) was computed using the solar constant, the solar incidence angle, a relative earth-sun distance, and a computed broad band atmospheric transmissivity. This transmissivity was estimated from sunshine duration or inferred from pyranometer measurements. The incoming long wave radiation ($Q_{L\downarrow}$) was computed using a modified Stefan-Boltzmann equation with an apparent emissivity that is coupled to the shortwave atmospheric transmissivity and a measured air temperature. Outgoing long wave radiation ($Q_{L\uparrow}$) was computed using the Stefan-Boltzmann equation with a calculated surface emissivity and surface temperature. Surface temperatures were computed from the satellite measurements of thermal radiances.

Soil heat flux was empirically calculated as a $G_0$/Rn fraction using vegetation indices, surface temperature, and surface albedo. Sensible heat flux was computed using wind speed observations, estimated surface roughness, and surface to air temperature differences ($\Delta T$), that were obtained through a sophisticated self-calibration between dry ($L_vE \approx 0$) and wet ($H \approx 0$) pixels. Franks and Beven (1999) used a similar approach to distribute spatial evapotranspiration. The wet and dry pixels were manually selected in the image. For the wet pixel it is assumed that $\Delta T = 0$. For the dry pixel $\Delta T$ is given by:

$$\Delta T = \frac{Hr_{ah}}{\rho_{air} c_p} \quad (3.)$$

Where $r_{ah}$ (s $m^{-1}$) is the near surface aerodynamic resistance to heat transfer, $\rho_{air}$ (kg $m^{-3}$) is the moist air density and $C_p$ (J $kg^{-1}$) is the specific heat at constant pressure. SEBAL solves this implicit equation iteratively. Empirically it has been shown that there is a linear relation between surface temperature ($T_0$) and $\Delta T$. This relation was used to estimate $\Delta T$ for all pixels in the image.

Knowing the instantaneous soil, latent, and sensible heat fluxes made it possible to calculate the evaporative fraction given by:

$$\Lambda = \frac{L_v E}{Q^* - G} \quad (4.)$$

The most important assumption of SEBAL is that the evaporative fraction is constant during the day and this assumption allows the conversion of an instantaneous $L_vE$ value to a daily value. Experimental work has demonstrated that this holds true for environmental conditions where soil moisture does not significantly change (e.g., Shuttleworth et al., 1989; Brutsaert and Sugita, 1992; Nicols and Cuenca, 1993; Kustas et al., 1994; Crago, 1996; Franks and Beven, 1997).

For periods longer than one day it may be assumed that the soil heat flux equals 0. The 24hr latent heat flux could therefore be determined by

$$L_v E_{24hr} = \Lambda Q^*_{24hr} \quad (5.)$$

The final step was to calculate biweekly evapotranspiration data. This was achieved by inserting $L_vE_{24hr}$ into the Penman-Monteith equation (Monteith, 1965). Using this

approach it was possible to inversely determine the surface resistance ($r_s$). There are some known associated problems with this approach. There is a strong relationship between the aerodynamic ($r_a$) and surface resistances and uncertainty in $r_a$ leads to incorrect estimates of $r_a$ (Beven, 1979; Franks *et al.*, 1997). By using a consistent $r_a$ from meteorological data the error in the eventual ET estimate is however minimal. Knowing the spatial distribution of the surface resistance made it possible to calculate $ET_{act}$ based on the Penman-Monteith equation and meteorological data for all days without satellite imagery (Bastiaanssen and Bandara, 2001). SEBAL has been extensively validated (Bastiaanssen *et al.*, 1998[b]).

The 16 biweekly $ET_{act}$ images of the Upper Bhima catchment were accumulated to eight monthly images from October 2004 to May 2005, which were all used in the calibration of the SWAT model. SEBAL could not be applied during the monsoon months (June to September) due to the lack of cloud free imagery.

*SWAT*

A SWAT model was built and simulations were run on a daily basis from June 2004 to May 2005. SWAT is a distributed hydrological model providing spatial coverage of the integral hydrological cycle including atmosphere, plants, unsaturated zone, groundwater, and surface water. The model is comprehensively described in literature (Arnold *et al*., 1998; Srinivasan *et al.*, 1998).

Conceptually SWAT subdivides the catchment into sub-basins and a river network based on a digital elevation model (DEM). Based on unique combinations of soil and land use, the sub-basins were further detailed into hydrological response units (HRUs), which were the fundamental units of calculation. A total of 115 sub basins and 768 HRUs were delineated in the Upper Bhima catchment.

The Penman-Monteith method (Monteith, 1965) was used in SWAT to calculate daily reference evapotranspiration for alfalfa ($ET_{ref}$) and potential plant transpiration ($ET_p$). Daily data on radiation, wind speed, relative humidity, and air temperature for two different meteorological stations were used (Figure 1). Potential daily plant transpiration is calculated using actual daily crop height and leaf area index (LAI), required to determine the aerodynamic resistances and canopy resistances respectively. Potential soil evaporation is an exponential function of $ET_{ref}$ and the soil cover and is further reduced during periods with high plant water use. Actual soil evaporation is limited by the soil water content ($\theta$) and is reduced exponentially when $\theta$ drops below field capacity.

To calculate actual plant transpiration the potential plant water uptake is defined by

$$w_{p,z} = \frac{ET_p}{\left[1 - e^{\beta_w}\right]} \cdot \left[1 - e^{\left(-\beta_w \cdot \frac{z}{z_{root}}\right)}\right] \quad (6.)$$

Where $w_{p,z}$ (mm $H_2O$) is the potential plant water uptake from the soil surface to a specified depth from the soil surface on a given day, $ET_p$ (mm $H_2O$) is the maximum plant transpiration on a given day, $\beta_w$ (-) is the water use distribution parameter, z is the depth from the soil surface (mm), and $z_{root}$ is the depth of root development in the soil (mm). Actual plant water uptake equals actual plant transpiration and is, similarly to soil evaporation, reduced exponentially when θ drops below field capacity. Actual evapotranspiration ($ET_{act}$) is the sum of interception, actual soil evaporation, and actual plant transpiration.

Meteorological data in SWAT are parameterized on sub-basin level. Because no precipitation data were available for the simulation period and to be able to capture the spatial heterogeneity in precipitation, monthly gridded precipitation estimates with a spatial resolution of 25 km derived with the Tropical Rainfall Monitoring Mission (TRMM; Kumerrow *et al.*, 1998) was used. The monthly grids were scaled using linear regression with 11 meteorological stations between 1998 and 2004 (Figure 1). This relationship was used to extend the time series to the simulation period. The grid based monthly data were aggregated per sub-basin and converted to daily precipitation using a weather generator. A total of 115 hypothetical meteorological stations were thus inferred on the model.

The major reservoirs (20) are mainly located along the Bhima branch. For modelling purpose, the reservoirs are clustered into two reservoirs. Because the simulation year was an averagely wet year, the assumption was made that over the entire year there was no

net increase or decrease in reservoir storage. The reservoirs inflow was largest during the monsoon season and throughout the irrigation year the water was used for irrigation. The unused excess water was released using a monthly distribution derived from historical measurements.

Land used in this study was based on a 15 class unsupervised land use classification using a time series of 16 MODIS derived Normalized Difference Vegetation Index (NDVI) images with a spatial resolution of 250 meter. The same imagery was used for the land use classification and the SEBAL analysis (Table 1). Based on existing land use map and field surveys 15 classes were clustered into the land use classes defined in Table 2. The results were visual verified with high resolution satellite imagery. The final land use map is shown in Figure 3.

The FAO digital soil map of the world (FAO, 1995) was used derive soil properties. Eight different soil units are identified in the catchment. The alluvial plains are predominantly characterized by vertisols and the Western Ghats and steeper slopes by luvisols.

*PEST*

In this study PEST (2005 version) was used to calibrate the SWAT model using $ET_{act}$ acquired with SEBAL.

PEST is a non-linear parameter estimation package that can be used to estimate parameters for just about any existing computer model (Doherty, 2005). PEST is able to run a model as many times as it needs to while adjusting its parameters until the

discrepancies between selected model outputs and a complementary set of field or laboratory measurements is reduced to a minimum.

PEST uses the GML algorithm is to optimize the model. The theory underlying the GML method is derived from the linear parameter estimation theory. The relation between a hydrological model (X), a set of parameters (p), a set of observations (H) and residuals in the observations (ε) can be described as:

$$X \cdot p = H + \varepsilon \quad (7.)$$

The goal of PEST is to find that p that minimises the objective function, which is defined as the sum of squared deviations between model generated values and experimental observations and can be written as:

$$\Phi = (H - Xp)' Q (H - Xp) \quad (8.)$$

Where Q is proportional to the inverse of C(ε), the covariance matrix of measurement noise. The objective function used in PEST is closely related to the commonly used root mean square error (RMSE) through:

$$RMSE = \left(\frac{\Phi}{N}\right)^{\frac{1}{2}} \quad (9.)$$

Φ is minimized when

$$p = (X^t Q X)^{-1} X^t Q h \quad (10.)$$

For linear models optimisation can be achieved in one step, whereas for non-linear problems it is an iterative process. At the beginning of each iteration the relationship between model parameters and model-generated outputs is linearised by formulating a Taylor expansion about the currently best parameter set; hence, the derivatives of all observations with respect to all parameters must be calculated. This linearised problem is

then solved for a better parameter set, and the new parameters tested by running the model again.

However, one of the most relevant restrictions in the GML algorithm, a gradient based method, is sensitivity to local minima. Recent advances in the GML algorithm have improved the capability to identify the global minimum in surface water models (Skahill and Doherty, 2006). The most pronounced advantage of the GML method is that it can generally complete a parameter estimation process with an extremely high level of model run efficiency.

*Calibration strategy*

The core of the calibration as tested in this study consists of a comparison of seven different parameter set estimations. The entire flowchart of the calibration strategy, including pre and post-calibration steps, is summarized in Figure 4.

Because $ET_{ref}$ is the basis for the $ET_{act}$ calculations, first, a simple adjustment was performed on the SWAT input solar radiation to ensure that calculated SWAT $ET_{ref}$ and measured SEBAL $ET_{ref}$ were equal. To account for impacts of slope and aspect on incident solar radiation SEBAL incorporates a digital elevation model (DEM) based correction. At the same time SEBAL $ET_{ref}$ assumes grass as a reference crop and SWAT assumes alfalfa.

After adjusting of $ET_{ref}$, it was verified through a set of box whisker plots whether $\Delta ET_{act}$ ($ET_{act}$ SEBAL – $ET_{act}$ SWAT) was explained by variation in land use, different soil type, month, or precipitation zone.

This analysis leads to the identification of a number of PEST optimisation runs for a single type of variable. Each PEST run optimizes a set of variables related to either of these explaining factors. The results of each PEST run (Φ reduction and $r^2$) were used to identify a number of combination PEST runs. Final results were analyzed at basin, sub-basin, and HRU level. All $ET_{act}$ optimisation runs calculated the Φ based on monthly data at sub basin level. A total of 920 observations (8 months times 115 sub basins) were used in the objective function. The following optimisation runs were formulated (Figure 4):

- Available water capacity (AWC). The AWC is defined as the difference between the field capacity of the soil and the permanent wilting point. It is defined per soil layer per soil type and determines, to a large extent, the water holding capacity of the soil. Ten different soil types with two layers each resulted in 20 different parameters to be optimized. AWC should is bound by the range 0.05 mm/mm and 0.60 mm/mm.
- Maximum potential leaf area index (BLAI). The LAI is the leaf area divided by the land area. The BLAI is one of six parameters that determine leaf area development of a crop in SWAT and determines the maximum threshold. BLAI is specified per land use type (Table 2) and, excluding water surfaces, resulted in 6 parameters to be optimized. The bounding range is between 2.0 and 8.0 for AGR1, AGR2, FRSE and FRST, between 5.0 and 12.0 for AGR3 and between 1.0 and 8.0 for RNGE.
- Monthly rainfall increment (RFINC). The RFINC is specified per month and per sub-basin and is defined as the relative monthly adaptation in rainfall. The assumption was made that the spatial distribution of the TRMM derived

precipitation was correct, however that for specific months the scaled absolute amounts of precipitation could be incorrect. This led to one variable to be optimized per month. RFINC is allowed to vary between -200% and 200% of the original monthly precipitation.

- Groundwater revap coefficient (REVAP1 and REVAP2). Water may conceptually move from the shallow aquifer into the overlying unsaturated zone. The process of water being evaporated from the capillary fringe in dry periods is referred to as groundwater revap and in SWAT quantified by the revap coefficient ($\beta_r$) multiplied by $ET_{ref}$. Two optimisation runs were designed. For the first optimisation run one $\beta_r$ for each land use, except water, was defined (REVAP1, 6 variables). For the second optimisation run it was assumed that $\beta_r$ varies per land use and per elevation zone. Four different elevation zones were defined (0-500 m, 500-600 m, 600-700m and >700m). In combination with land use this resulted in 21 unique $\beta_r$ resulting from unique combinations of elevation zone and land use class (REVAP2, 21 variables). For both optimisation runs the revap coefficient may range between 0.0 and 0.5.

Two combined optimisation runs were performed based on the results of the individual runs (COM1 and COM2). COM1 combined AWC, RFINC and GWREVAP and COM2 combined AWC, RFINC and GWREVAP2.

The results of the best performing combination run were validated using historical stream flow data.

## 4 Results

Monthly analysis of the $ET_{ref}$ differences between SEBAL and SWAT revealed that the differences between SEBAL and SWAT typically range from 6.1 mm month$^{-1}$ in May 2005 to 29.9 mm month$^{-1}$ in March 2005 with an average monthly difference of 16 mm month$^{-1}$. Figure 5 shows the results of the $ET_{ref}$ adjustments. SWAT $ET_{ref}$ (base) is consistently lower than SEBAL $ET_{ref}$. With a modest relative adaptation of solar radiation per month and per sub-basin, the monthly differences were reduced to minimal (adjusted). On average radiation values were increased by 3.5% with a maximum of 7% for one sub basin in March.

SWAT simulated $ET_{act}$ with the base model (base) in the 2004-2005 irrigation year was 775 mm with the highest $ET_{act}$ in August (112 mm) and the lowest in February (34 mm). Figure 6 shows box-whisker plots of monthly $\Delta ET_{act}$ per land use, soil type, month, and precipitation class respectively. The order of magnitude of SWAT $ET_{act}$ is similar to SEBAL, $\Delta ET_{act}$ is on average slightly positive indicating that $ET_{act}$ measured by SEBAL is slightly higher than SWAT simulated values. The distribution of $\Delta ET_{act}$ resembles a normal distribution for most cases, but ranges between the first and third quartile are considerable and vary between land uses, soil types, months and precipitation classes.

Table 3 presents the results for the different optimisation runs. In the base run the RMSE was equal to 24 mm/month and $ET_{act}$ SWAT iwas generally higher than the $ET_{act}$ SEBAL ($\varepsilon$ = 5.2 mm/month). The AWC run reduced the RMSE to 22 mm and the average value for the AWC after optimisation was 0.22 mm/mm, while the average initial value was 0.15 mm/mm. The model was relatively insensitive to maximum plant leaf area index

(BLAI). The RMSE was not reduced and the average of the residuals only decreased by 0.4 mm/month. The RFINC optimisation run had a significant effect and the $r^2$ increased from 0.40 to 0.70. The average adjustment in monthly precipitation during the calibration months was limited (-13 mm/month) with a maximum in December (21 mm) and a minimum in April (-29 mm). $ET_{act}$ SWAT was also sensitive to the groundwater revap coefficient. The GWREVAP run (6 variables) resulted in a RMSE of 17 mm and ε was reduced to 1.6 mm/month. GWREVAP2 (21 variables) yielded a slightly higher $r^2$ but no significant improvements in RMSE and ε were observed. The best results were achieved by the combination runs (COM1 and COM2). COM2 yielded the best results in the optimisations: 2987 model calls were required to increase $r^2$ from 0.40 to 0.81. The RMSE in that case equalled 13 mm/month and $ET_{act}$ SWAT was on average only 0.5 mm/month higher. The COM1 results were also good, but significantly less model calls were required (1610). In the COM1 run the average available water content increased from 0.15 mm/mm to 0.21 mm/mm, the rainfall adjustment on average was -2% during the calibration months and the groundwater revap coefficient equalled 1.1.

There are several ways to evaluate the reliability of any optimisation of a distributed hydrological model across time and space. Figure 7 shows the scatter plots for run COM1 between SEBAL $ET_{act}$ and SWAT $ET_{act}$ on catchment, sub-basin and HRU level respectively. It also shows the individual monthly data and the eight month sum of $ET_{act.}$ The figure shows that the goodness of fit decreases with spatial and temporal detail. The $r^2$ of monthly catchment $ET_{act}$ for example is as high as 0.90, while at HRU level the $r^2$ is only 0.35. In time we see similar patterns. The $r^2$ at monthly sub basin level is 0.81 while if the eight month sum is analyzed the $r^2$ increase to 0.92.

Figure 8 maps the eight month $ET_{act}$ sum for SWAT and SEBAL at sub-basin and at HRU level. At sub-basin level, the spatial patterns between SWAT and SEBAL were highly consistent. At HRU level there were considerable differences. The general spatial patterns were well depicted. However, some HRUs within a sub-basin evaporated more than measured with SEBAL and some evaporated less, however aggregated over the entire sub basin these differences were levelled out. For example most sub basins with a significant area of AGR3 also contained a large area of RNGE. $ET_{act}$ of AGR3 seems to be overestimated and $ET_{act}$ of RNGE seems to be underestimated. On subbasin scale these differences level out and the results are good, however the variation in SWAT $ET_{act}$ at HRU level was larger. This was a result of the fact that PEST optimises monthly $ET_{act}$ at sub basin level and not at HRU level.

Discharge data of the simulation period are unavailable and even if measured discharge would be available, their use in calibration would be questionable, given the fact that stream flow is completely human controlled in the catchment. A qualitative control on measured discharge was however performed using historical data from 1970 to 1996. The discharges of the entire catchment were used for comparison with the model simulations. Table 4 shows the observed and simulated discharges. The simulated discharges in 2004-2005 were well within one standard deviation of the average measured discharges between 1970 and 1996. December was an exception and modelled discharges were slightly higher. It should be noted though, that the coefficient of variation in the observed discharges were large and range from 66% in August to 160% in May.

## 5 Discussion and conclusions

This study showed that the spatially distributed hydrological model SWAT can be successfully calibrated using the GML algorithm and remotely sensed derived evapotranspiration from a time series of MODIS images in a data scarce area. The best results were obtained by optimising a combination of soil, meteorological, and groundwater related parameters for an eight month time series of sub-basin actual evapotranspiration. Optimising a total of 53 variables using 920 monthly observations increased the $r^2$, significantly, from 0.40 to 0.81. A validation with historical measured discharges revealed that the modelled discharges are well within one standard deviation of the observed data. Separate optimisation runs revealed that $ET_{act}$ is more sensitive to the groundwater and meteorological parameters than to soil and land use parameters. On sub-basin level the $ET_{act}$ showed least response to the land cover dependent maximum leaf area index. Furthermore, it can be concluded that at the HRU level more work is required to fine-tune the calibration procedure. The calibration was only reliable at the spatial and temporal scale on which the observations, used in the optimisation, were based. Future work should focus on calibration strategy that incorporates HRU level $ET_{act}$ observations and discharges at a high temporal resolution in the objective function.

In this study, the gradient search GML algorithm was used in the optimisation although this method is sometimes sensitive to local minima, especially when non-linear processes are modelled. However, a time series of spatially distributed $ET_{act}$ exhibits more linear behaviour than discharge at a limited number of locations. Moreover, it has been shown that global search algorithms require much more function calls to identify the global

minimum. SWAT was recently used in the evaluation of a number of optimisation algoritms; Shuffled Complex Evolution, real-valued simple Genetic Algorithm, multi-start Simplex and Monte Carlo Sampling and a new algorithm called the Global Greedy Search algorithm (Tolson and Schoemaker, 2006). For two case studies a maximum of 2500 (6 parameters) respectively 6000 (14 parameters) SWAT model calls were required. The GML algorithm is much more efficient in this respect (Skahill and Doherty, 2006) and for the best performing optimisation (53 parameters) in this study 2987 model calls were required. We therefore conclude that PEST and the GML algorithm served our objectives best.

Traditional calibration on a limited number of discharge stations lumps all hydrological processes together and chances on the occurrence of the equifinality problem are much larger. In this study we showed that using spatially distributed $ET_{act}$ observations with a monthly temporal resolution provide a promising alternative. The success of the approach lays in the spatial and temporal isolation of the calibration problem at hand. Information content of a time series of discharges at the outlet of a catchment is simply insufficient to attribute deviations between observation and simulation to specific processes at a specific location at a specific point in time. Using spatial data constrains the spatial distribution of fluxes, but the equifinality problem may still occur at the scale of a HRU given the large number of parameters in the SWAT model. Franks and Beven (1997, 1999) utilised the function similarity concept and use representative parameter combinations at the unit scale, which are not necessarily correct, but produce the correct output. Although it is important to consider this issue of equifinality at the HRU scale we believe that using function similarity concept compromises the understanding of hydrological processes.

The approach of this study offers a basically unlimited number of observations in time and space and adding information on for example stream flows or groundwater heads to the objective function may further reduce equifinality issues without compromising parameterisation of essential hydrological processes. Although we have found very good results at the sub basin level on a monthly time step, further study is required to increase the reliability of the results in space (at HRU level) and time (weekly or daily).

One of the variables used in the optimisation is a monthly rainfall increment. It is generally not common practice to vary model excitations in a calibration procedure; however we believe that in this case it was legitimate. Precipitation data used in this study was based on TRMM for two important reasons: (i) station data for the simulation period are unavailable and (ii) there is a large spatial variation in precipitation that is not captured by using a limited number of meteorological stations. However using raw TRMM data would result in unreliable absolute precipitation amounts and the TRMM precipitation is scaled with data from 13 meteorological stations within the catchment using linear regression and data between 1998 and 2004. The $r^2$ values between monthly TRMM and observed rainfall for these stations range from 0.29 tot 0.81 with an average of 0.59. Both TRMM as well as the observed station data are subject to error, which cannot be isolated. Considering this it was justifiable to use monthly RFINC as calibration parameter. No changes occur in the spatial distribution of rainfall and average adjustment in precipitation is only -13 mm/month with an maximum in December (21 mm) and a minimum in April (-29 mm) for the best performing optimisation.

The calibration period covers only eight months and a longer time scale would be preferable. Presently longer time series of Remotely Sensed $ET_{act}$ are unavailable, but this might changes in the future with the advent of a standard MODIS ET product (Running *et al.,* 1995).

Realistic simulations during the dry period from October to May are also more important than the monsoon period. Runoff is not a critical issue, but ET management, water shortage and irrigation are the dominant hydrological issues relevant to water managers. The monsoon period is not covered in the calibration, because of the absence cloud free imagery. SEBAL depends on the visible, NIR en thermal IR part of the spectrum which is hampered by clouds. A viable alternative could be to incorporate radar based soil moisture in a combined objective function during the monsoon months in order to appropriately calibrate the model in the monsoon season.

Differences in space and time in $ET_{ref}$ between SEBAL and SWAT were caused by spatial altitude dependent operations, which SEBAL performs on important parameters. The DEM was used to correct air pressure and density and thus the psychometric constant. The DEM was further used to correct the absorbed solar radiation values for slope and aspect. Southern facing terrain, due to the angle of incidence, absorbs more solar radiation per unit land than the northern facing slope. Another cause of the difference in $ET_{ref}$ is the fact that SEBAL uses grass as a reference crop and SWAT uses alfalfa. We showed that a near perfect match between observed and measured $ET_{ref}$ after inferring a small adjustment (average = 3.5%) of monthly radiation.

Additional validation with discharge data could only be based on historical data, because of lack of data. Another compromising factor is that stream flow in the catchment is mainly human controlled through a cascade of reservoirs and local water storage facilities and are therefore less suitable for validation. The key objective of this study was to introduce an innovative calibration procedure based on Remotely Sensed $ET_{act}$ , especially targeted for these kinds of data scarce human controlled catchments.

In developing countries, where lack of data is an issue and the planning process needs to be supported by scientific sound measures, the innovative use of Remote Sensing in hydrological model calibration as presented in this study will contribute to the prevention of disasters and improve sustainable management in the long term. Recently, interest in using simulation models in ungauged or sparsely gauged basins has increased leading to some concerted actions. The most relevant is the Prediction in Ungauged Basin (PUB) initiative; an International Association for Hydrological Sciences (IAHS) initiative for the decade of 2003-2012, aimed at uncertainty reduction in hydrological practice (Sivapalani *et al.*, 2003). PUB focuses the development of new predictive approaches that are based on "understanding" of hydrological functioning at multiple space-time scales. This study provided an ET based innovative approach at different temporal and spatial scale that fits well into the PUB science program.

## 6 Acknowledgements

This study was financially supported by the The National User Support Programme 2001-2005 (NUSP) was executed by the Netherlands Agency for Aerospace Programmes (NIVR) and the Space Research Organization of the Netherlands (SRON). The authors are grateful to WaterWatch for providing the SEBAL evapotranspiration data and to Dr. Anju Gaur of the International Water Management Institute for providing the baseline data of the Upper Bhima catchment. We would also like to thank three reviewers for providing useful comments.

## 7 References

Anderton S, Latron J, Gallart F. 2002. Sensitivity analysis and multi-response, multi-criteria evaluation of a physical based distributed model. *Hydrological Processes* **16**: 333-353.

Arnold JG, Srinivasan P, Muttiah RS, Williams JR. 1998. Large area hydrologic modeling and assessment. Part I. Model development. *Journal of the American Water Resources Association* **34**: 73–89.

Bastiaanssen WGM, Menenti M, Feddes RA, Holtslag AAM. 1998. The Surface Energy Balance Algorithm for Land (SEBAL): Part 1 formulation, *Journal of Hydrology*: **212-213**: 198-212.

Bastiaanssen WGM, Pelgrum H, Wang J, Ma Y, Moreno J, Roerink GJ, van der Wal T. 1998[b]. The Surface Energy Balance Algorithm for Land (SEBAL): Part 2 validation. Journal of Hydrology **212-213**: 213-229.

Bastiaanssen, WGM, Bandara KMPS. 2001. Evaporative depletion assessments for irrigated watersheds in Sri Lanka. *Irrigation Science* **21**: 1-15

Beven K. 1979. A sensitivity analysis of the Penman-Monteith actual evapotranspiration estimates. *Journal of Hydrology* **44**: 169-190.

Beven KJ. 1993. Prophecy, reality and uncertainty in distributed hydrological modeling. *Advances in Water Resources* **16**: 41–51.

Beven KJ. 2000. Uniqueness of place and process representations in hydrological modelling. *Hydrology and Earth System Sciences* **4:** 203–213

Beven KJ. 2001. How far can we go in distributed hydrological modelling? *Hydrology and Earth System Science* **5**: 1-12.

Beven KJ, Freer J. 2001. Equifinality, data assimilation, and uncertainty estimation in mechanistic modelling of complexenvironmental systems. Journal of Hydrology **249:** 11–29

Beven K. 2006. A manifesto for the equifinality thesis. *Journal of Hydrology* **320**: 18-36

Boegh E, Thorsen M, Butts MB, Hansen S, Christiansen JS, Abrahamsen P, Hasager CB, Jensen N, Van der Keur P, Refsgaard JC, Schelde K, Soegaard H. Thomsen A. 2004. Incorporating remote sensing data in physically based distributed agro-hydrological modeling. *Journal of Hydrology* **287**: 279-299

Brutsaert W, Sugita M. 1992. Application of self-preservation in the diurnal evolution of the surface energy balance budget to determine daily evaporation, J. Geophys. Res. **97(D17):** 18377–18382.

Campo L, Caparrini F, Castelli F. 2006. Use of multi-platform, multi-temporal remote-sensing data for calibration of a distributed hydrological model: an application in the Arno basin, Italy. *Hydrological Processes* **20**: 2693:2712.

Crago RD. 1996. Comparison of the evaporative fraction and the Priestley–Taylor a for parameterizing daytime evaporation. *Water Resources Research* **32**: 1403– 1409.

Duan Q , Sorooshian S , Gupta HV , Rousseau A , Turcotte R (eds). 2003. Advances in Calibration of Watershed Models. AGU Monograph Series. Water Science and Application 6. American Geophysical Union: Washington DC.

Doherty J. 2005. PEST: Model Independent Parameter Estimation. fifth edition of user manual. Watermark Numerical Computing: Brisbane.

FAO. 1995. FAO-Unesco digital Soil Map of the World and derived soil properties, 1:5.000.000. Unesco: Paris.

Franks SW, Beven KJ. 1997. Estimation of evapotranspiration at the landscape scale: A fuzzy disaggregation approach. *Water Resources Research* **33**: 2929– 2938.

Franks SW, Beven KJ, Quinn PF, Wright IR. 1997. On the sensitivity of soil-vegetation-atmosphere transfer (SVAT) schemes: equifinality and the problem of robust calibration. *Agriculture and Forest Meteorology* **86**: 63-75.

Franks, SW, Beven KJ. 1999. Conditioning a multiple-patch SVAT model using uncertain time-space estimates of latent heat fluxes as inferred from remotely sensed data, *Water Resources Research.* **35**: 2751-2762.

Gunnel Y. 1997. Relief and climate in South Asia: the influence of the Western Ghats on the current climate pattern of Peninsular India. *International Journal of Climatology* **17**: 1169-1182.

Gupta VK, Sorooshian S, Yapo PO. 1998. Towards improved calibration of hydrologic model: multiple and noncommensurable measures of information. *Water Resources Research* **34**: 751-763.

Hall FG, Huemmrich KF, Goetz SJ, Sellers PJ, Nickelson JE. 1992. Satellite remote sensing of surface energy balance: Success, failures, and unresolved issues in FIFE. *Journal of Geophysical Research* **97(D17)**: 19061-19089.

Houser PR., Shuttleworth WJ, Famiglietti JS, Gupta HV, Syed KH, Goodrich DC. 1998. Integration of soil moisture remote sensing and hydrological modeling using data assimilation. *Water Resources Research* **34**: 3405-3420

Kite GW, Droogers P. 2000. Comparing evapotranspiration estimates from satellites, hydrological models and field data. *Journal of Hydrology* **229**: 3-18.

Kite GW, Pietroniro A, 1996. Remote sensing applications in hydrology. *Hydrological Sciences* **41**: 563-592.

Kuczera G. 1997. Efficient subspace probabilistic parameter optimization for catchment models. *Water Resources Research* **33**: 177–185.

Kummerow C, Barnes W, Kozu T, Shiue J, Simpson J. 1998. The tropical rainfall measuring mission (TRMM) sensor package. *J. Atmos. and Ocean Tech.* **15**: 808-816

Kustas WP, Perry PE, Doraiswamy PC, Moran MS. 1994. Using satellite remote sensing to extrapolate evapotranspiration estimates in time and space over a semiarid rangeland basin. *Remote Sensing of Environment* **49**: 275– 286.

Levenberg K. 1944. A method for the solution of certain non-linear problems in least squares. *Q. Appl. Math.* **2**: 164-168.

Marquardt DW. 1963. An algorithm for least-squares estimation of nonlinear parameters. *Journal of the Society of Industrial and Applied Mathematics* **11**: 431-441.

Monteith JL. 1965. Evaporation and environment. *Sym. Soc. Exp. Biol.* **19**: 205-234.

Nash JE, Sutcliffe JV. 1970. River flow forecasting through conceptual models, part I—a discussion of principles. *Journal of Hydrology* **10**: 282–290.

Neena D. 1998. Inter-state variation in cropping pattern in India. *Indian Journal of Regional Science* **30:** 57-69.

Nelder AJ, Mead R. 1965. A simplex method for function minimization. *Computer Journal* **7**: 308–313.

Nicols WE., Cuenca. 1993. Evaluation of the evaporative fraction for parameterization of the surface energy balance, *Water Resources Research* **29:** 3681–3690.

Running SW, Justice CO, Salomonson V, Hall D, Barker J., Kaufman YJ, Strahler AH, Huete AR, Muller JP, Vanderbilt V, Wan ZM, Teillet P., Carneggie D. 1995. Terrestrial remote sensing science and algorithms planned for EOS/MODIS. *International Journal of Remote Sensing* **15**: 3587-3620.

Shuttleworth WJ, Gurney RJ, Hsu AY, Ormsby JP. 1989. FIFE: The variation in energy partitioning at surface flux sites, remote sensing and large scale global processes. In Proc. Baltimore Symp.. Red Book. Int. Assoc. of Hydrol. Sci. (IAHS): Oxfordshire. **186:** 67–74,

Shuttleworth J. 1998. Combining remotely sensed data using aggregation algorithms. *Hydrology and Earth System Sciences* **2**, 149-158.

Singh VP, Woolhiser DA. 2002. Mathematical Modeling of Watershed Hydrology. *Journal of Hydrological Engineering* **7**:270-292.

Sivapalani M, Takeuchi K, Frank SW, Gupta VK, Karambiris H, Lakshmi V, Liang X, McDonell JJ, Mendiondo, EM, O'Conell PE, Oki T, Pomeroy JW, Schertzer D, Uhlenbrook S, Zehe E. 2003. IAHS Decade on Predictions in Ungauged Basins (PUB), 2003–2012: Shaping an exciting future for the hydrological sciences. *Hydrological Sciences* **48**: 857-880

Skahill BE, Doherty J. 2006. Efficient accommodation of local minima in watershed model calibration. *Journal of Hydrology (in press)*.

Sorooshian S, Gupta VK. 1995. Model calibration. In *Computer Models of Watershed Hydrology*, Singh VP (eds.). WaterResources Publications, Colorado; 23–68

Srinivasan R, Ramanarayanan TS, Arnold JG, Bednarz ST. 1998. *Large area hydrologic modeling and assessment part II: model application. Journal of American Water Resource Association* **34**: 91–101.

Su Z. 2000. Remote sensing of land use and vegetation for mesoscale hydrological studies. *International Journal of Remote Sensing Volume* **21:** 213 - 233

Tolson BA., Schoemaker CA. 2005. Comparison of optimization algorithms for the automatic calibration of SWAT2000. In: 3rd International SWAT Conference July 11-15 2005, Abbaspour K, Srinivasan R (eds.), Zürich.

Wang QJ. 1991. The genetic algorithm and its application to calibrating conceptual rainfall-runoff models. *Water Resources Research* **27**:2467–2471.

Wood EF. 1995. Scaling behaviour of hydrological fluxes and variables: empirical studies using a hydrological model and remote sensing data. *Hydrological Processes* **9**: 331-346.

Zhong Q, Li YH. 1988. Satellite observation of surface albedo over the Qinghai-Xizang plateau region. *Adv. ATmos. Sci,* **5**: 57-65.

## Tables

**Table 1: Date and local acquisition time (+5:30 GMT) of Aqua-MODIS images.**

| Date | Time |
|---|---|
| 16/10/2004 | 1:40 PM |
| 21/10/2004 | 2:00 PM |
| 04/11/2004 | 2:10 PM |
| 22/11/2004 | 2:00 PM |
| 03/12/2004 | 1:40 PM |
| 17/12/2004 | 1:50 PM |
| 07/01/2005 | 2:10 PM |
| 18/01/2005 | 1:50 PM |
| 12/02/2005 | 1:45 PM |
| 19/02/2005 | 1:50 PM |
| 14/03/2005 | 2:00 PM |
| 23/03/2005 | 1:50 PM |
| 10/04/2005 | 1:40 PM |
| 19/04/2005 | 1:35 PM |
| 14/05/2005 | 1:25 PM |
| 17/05/2005 | 1:55 PM |

**Table 2: Acreages of different land use and land cover in the catchment**

| Class name | Code | Area ($10^3$ ha) | Area (% ) |
|---|---|---|---|
| Water surfaces | WATR | 4111 | 1 |
| Rangelands | RNGB | 122417 | 27 |
| Rain fed agriculture | AGR1 | 153477 | 34 |
| Supplemental irrigated agriculture | AGR2 | 61208 | 13 |
| Irrigated sugarcane | AGR3 | 90899 | 20 |
| Evergreen forest | FRSE | 14160 | 3 |
| Mixed forest | FRST | 10506 | 2 |

**Table 3: Results of different optimisations runs. #var and #obs are the number of variables and observations used in the optimisations. The Φ (Eq. 8) is the sum of the squared deviations between monthly SEBAL and SWAT $ET_{act}$ summed over all sub basins (objective function), RMSE is the Root Mean Square Error (Eq. 9), ε is the average of the residuals and # model calls is the number of model calls required to reach the optimisation results.**

| PEST run | Variable | # var | # obs | Φ | RMSE (mm/month) | $r^2$ | ε (mm/month) | # model calls |
|---|---|---|---|---|---|---|---|---|
| BASE | - | 0 | 920 | 5.29E+05 | 24.0 | 0.40 | 5.9 | - |
| AWC | Available water content | 20 | 920 | 4.49E+05 | 22.1 | 0.49 | 5.2 | 664 |
| BLAI | Maximum plant leaf area index | 6 | 920 | 5.19E+05 | 23.8 | 0.41 | 5.5 | 68 |
| RFINC | Monthly rainfall increment | 12 | 920 | 2.54E+05 | 16.6 | 0.70 | 0.8 | 324 |
| GWREVAP | Groundwater revap coefficient | 6 | 920 | 2.78E+05 | 17.4 | 0.68 | 1.6 | 55 |
| GWREVAP2 | Groundwater revap coefficient | 21 | 920 | 2.66E+05 | 17.0 | 0.70 | 1.7 | 792 |
| COM1 | Available water content, monthly rainfall increment, groundwater revap coefficient | 53 | 920 | 1.63E+05 | 13.3 | 0.81 | 0.5 | 2987 |
| COM2 | Available water content, monthly rainfall increment, groundwater revap coefficient | 38 | 920 | 1.77E+05 | 13.9 | 0.79 | -0.5 | 1610 |

**Table 4: Observed historical and modelled discharges catchment. $Q_{swat}$ is the modelled discharge from June 2004 to May 2005. $Q_{avg}$ is the average historical discharge, $Q_{avg-1SD}$ is the maximum of zero and the average discharge minus one standard deviation, $Q_{avg+1SD}$ is the average discharge plus one standard deviation. Historical dataset is based on 1970-1996 time series.**

| **Month** | $Q_{avg-1SD}$ ($m^3s^{-1}$) | $Q_{avg}$ ($m^3s^{-1}$) | $Q_{avg+1SD}$ ($m^3s^{-1}$) | $Q_{swat}$ ($m^3s^{-1}$) |
|---|---|---|---|---|
| June | 0 | 114 | 274 | 62 |
| July | 39 | 562 | 1085 | 527 |
| August | 266 | 785 | 1303 | 689 |
| September | 110 | 713 | 1316 | 1158 |
| October | 0 | 382 | 795 | 347 |
| November | 0 | 81 | 171 | 129 |
| December | 0 | 33 | 73 | 93 |
| January | 0 | 17 | 34 | 29 |
| February | 0 | 9 | 19 | 13 |
| March | 0 | 6 | 16 | 2 |
| April | 0 | 4 | 9 | 0 |
| May | 0 | 9 | 23 | 0 |

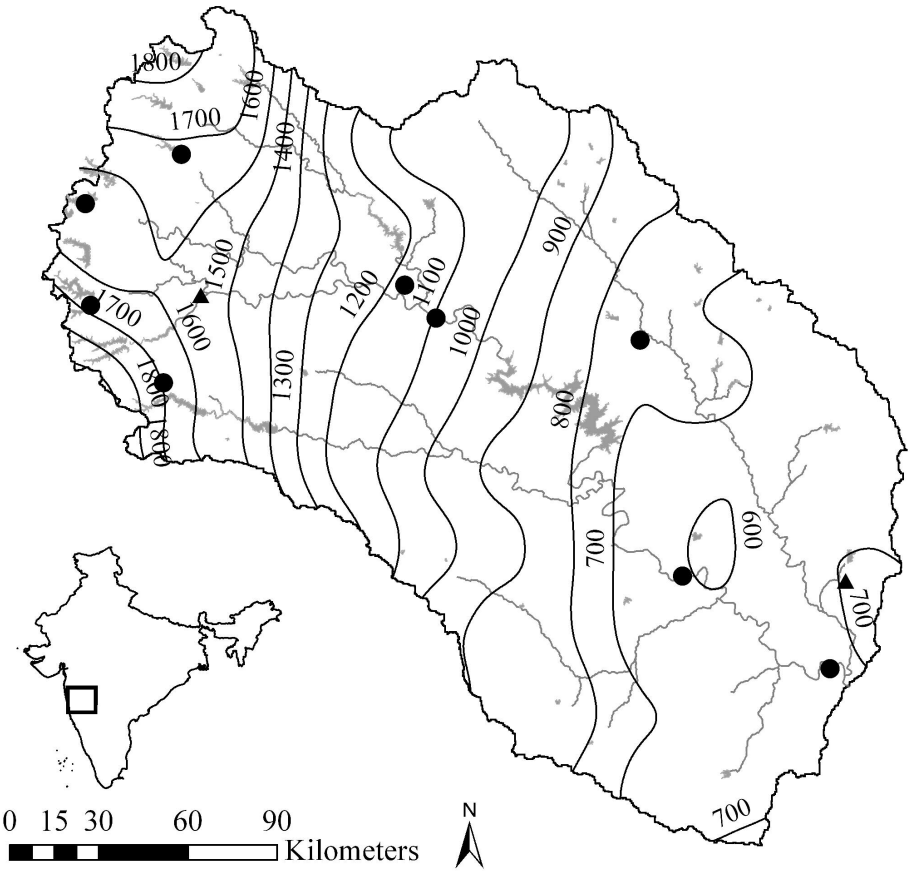


**Figure 1: Upper Bhima catchment boundary, contours of the precipitation sum from June 2004 to May 2005, river network, major reservoirs, and meteorological station (circles represent precipitation stations; triangles represent precipitation, temperature, wind speed, relative humidity and radiation stations)**

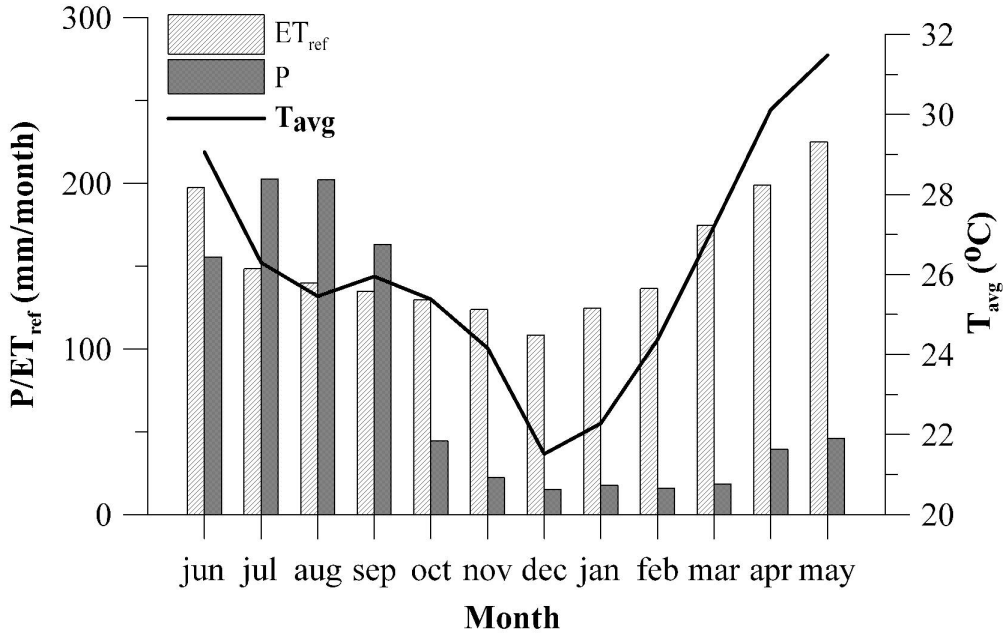


**Figure 2: Monthly precipitation (P), reference evapotranspiration (ETref) and temperature from June 2004 to May 2005.**

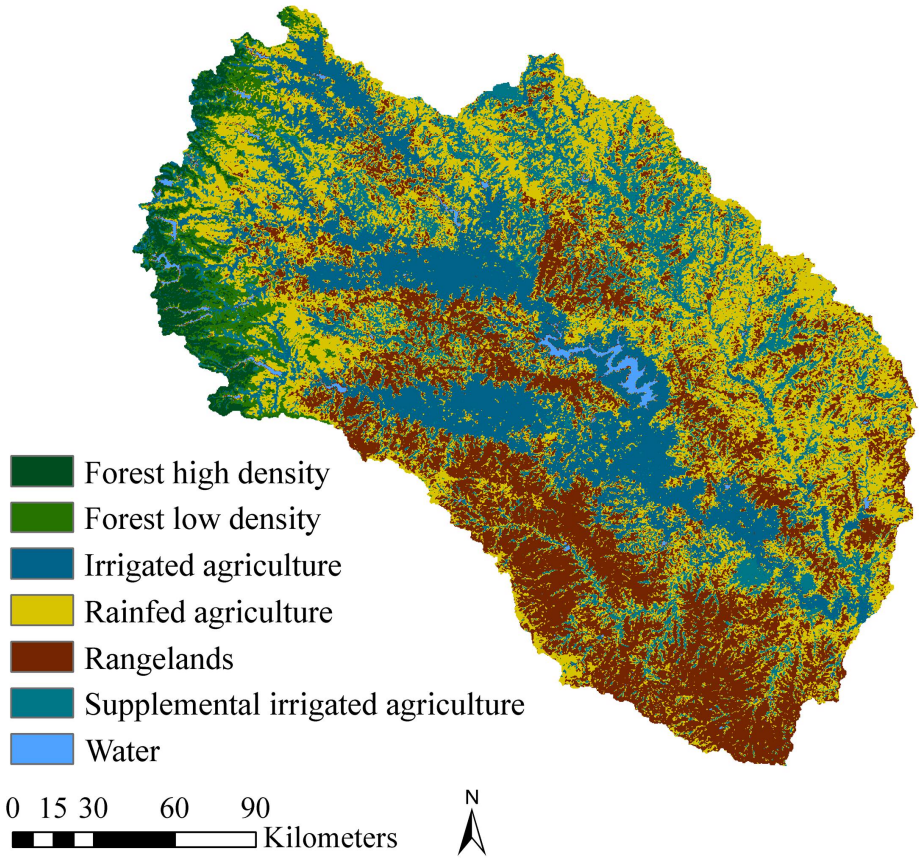


**Figure 3: Land use based on unsupervised classification of MODIS time series of NDVI imagery.**

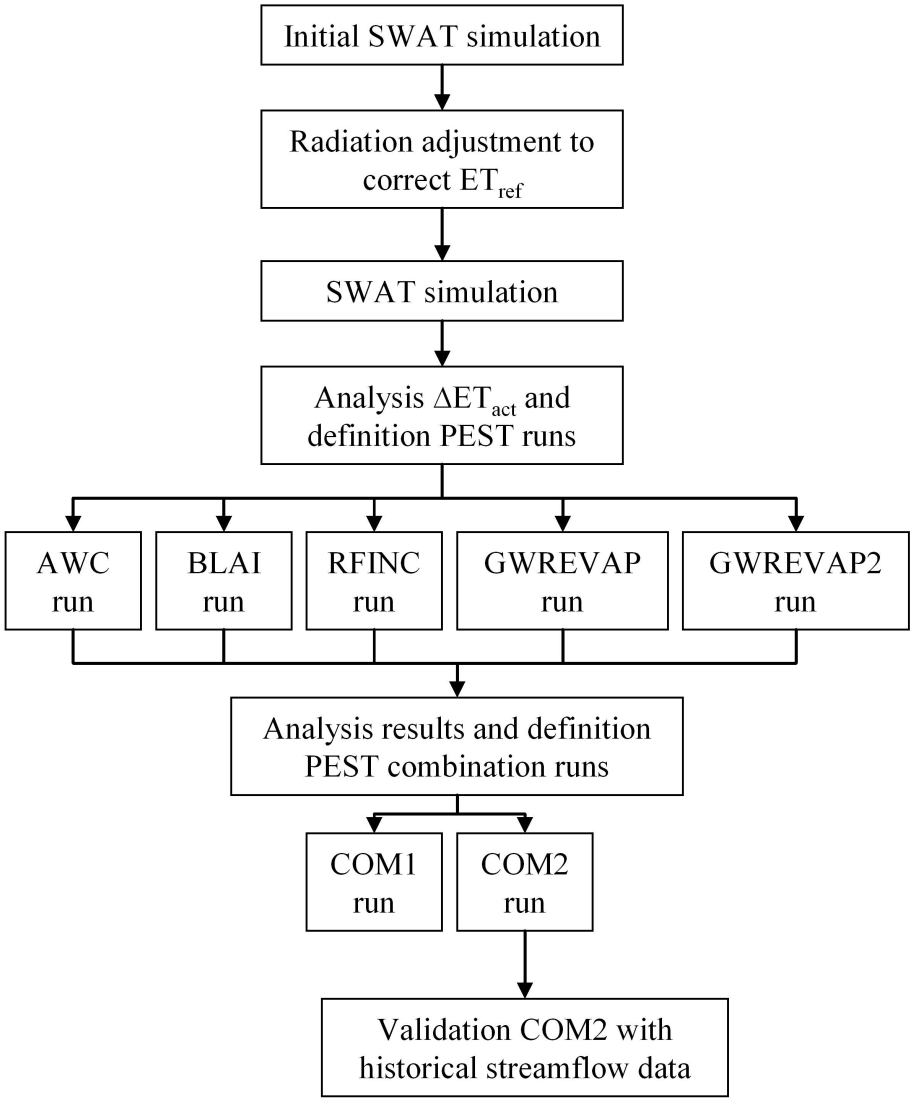


**Figure 4: Flowchart of calibration strategy.**

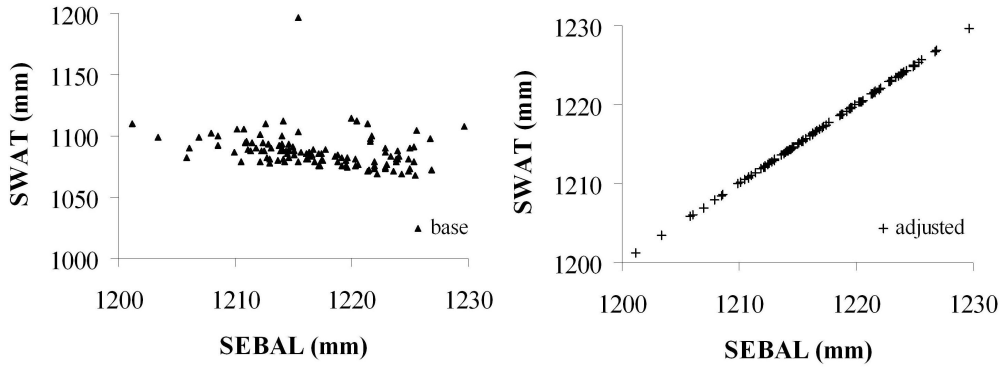


**Figure 5: Scatter plot of SEBAL vs. SWAT of the sum of ETref from October 2004 to May 2005 per sub basin.**

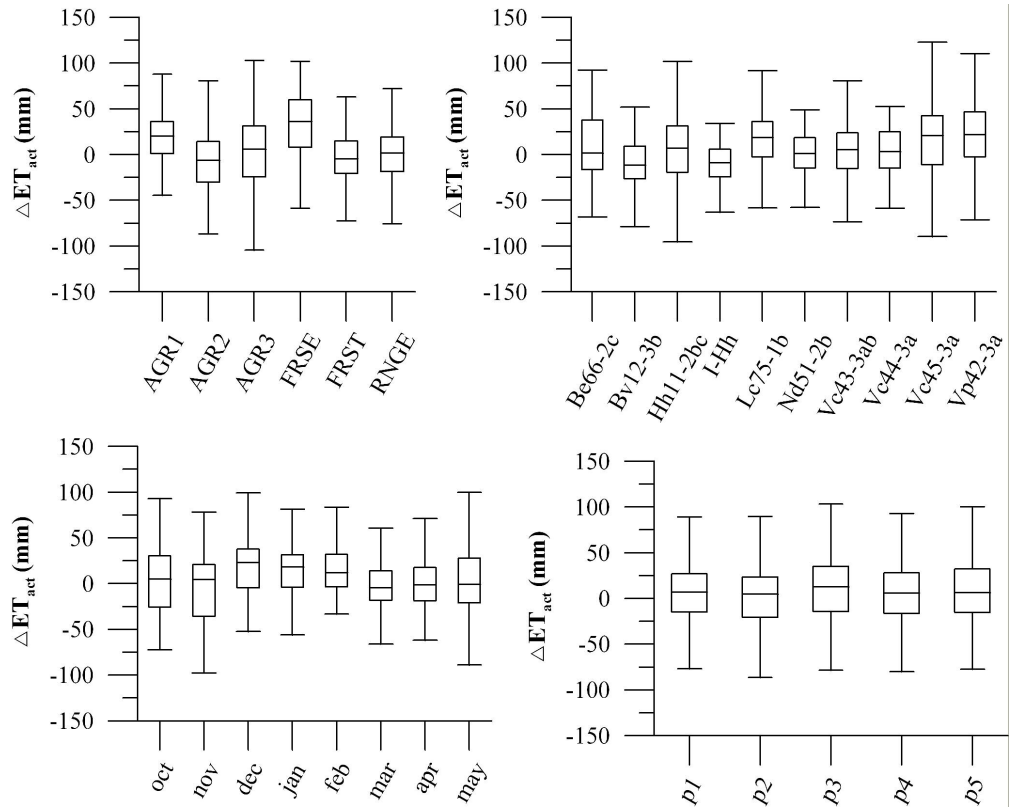


**Figure 6: Box whisker plots of monthly ΔETact (SEBAL Â□ SWAT) per land use class (top left), soil class (top right), month (bottom left) and precipitation class (bottom right; p1 = 0-800 mm yr-1, p2 = 800-1100 mm yr-1, p3= 1100-1400 mm yr-1, p4=1400-1700 mm yr-1, p5=1700-2000 mm yr-1 ). The box-whisker plots show the median, first and third quartiles. The caps at the end of the boxes show the extreme values.**

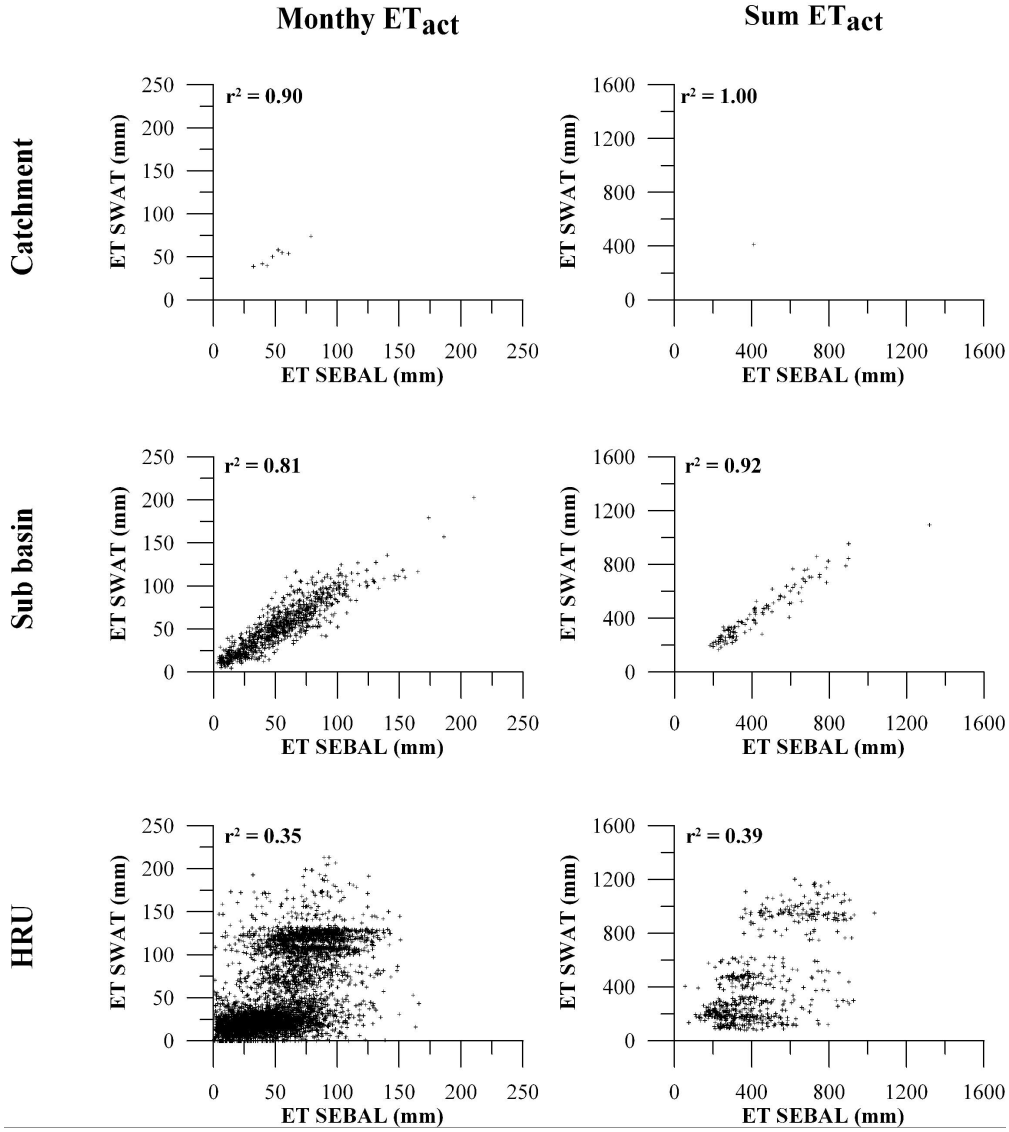


**Figure 7: Scatter plots of SEBAL and SWAT ETact. Monthly data are shown on the left side graphs and the eight month sum is on the right side of the graphs. Spatial detail increases from top to bottom and ranges from catchment, sub basin to HRU level respectively. SWAT results relate to COM1 optimisation.**

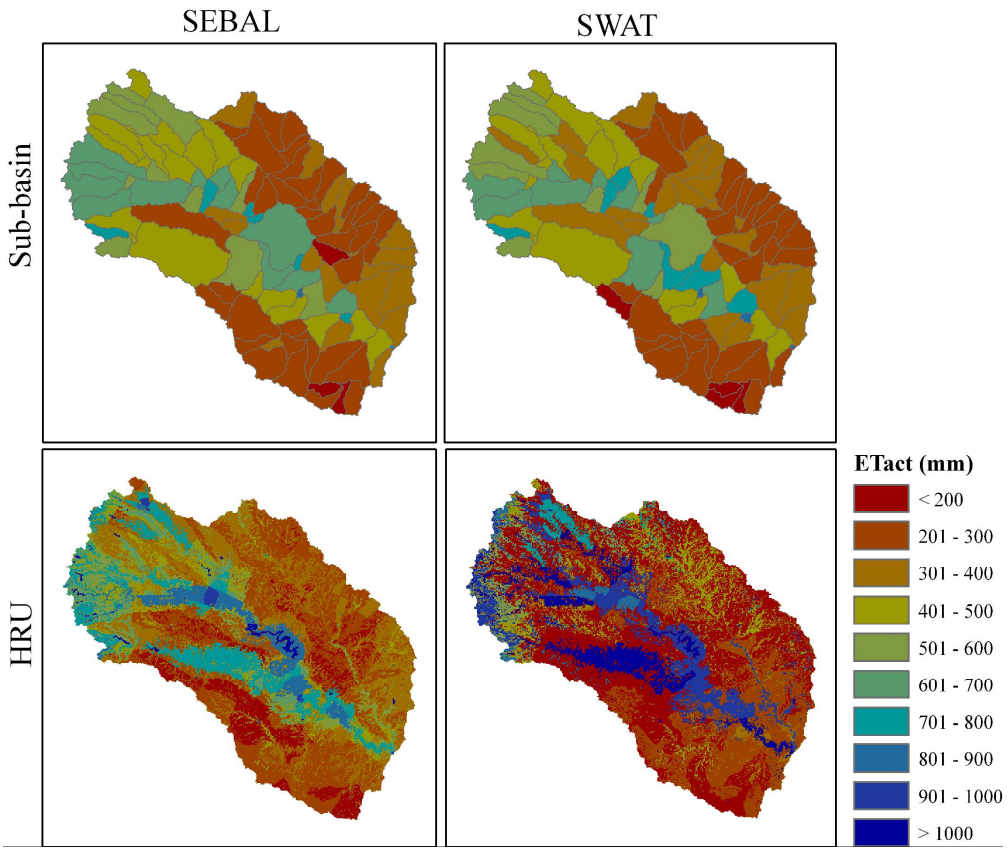


**Figure 8: Eight month sum of ETact for SWAT and SEBAL on sub basin and HRU level respectively. SWAT results relate to COM2 optimisation.**

# Annex 2: Paper Agricultural Water management

Elsevier Editorial System(tm) for Agricultural Water Management

Manuscript Draft

Manuscript Number:

Title: Evaluating water use and productivity in the upper Bhima catchment, India, by integrating remote sensing and a process based hydrological model

Article Type: Research Paper

Section/Category: Crop water use

Keywords: SWAT; SEBAL; calibration; water productivity; evapotranspiration

Corresponding Author: MSc. Walter Immerzeel, MSc.

Corresponding Author's Institution: FutureWater

First Author: Walter Immerzeel, MSc.

Order of Authors: Walter Immerzeel, MSc.; Anju Gaur, Dr.; Sander J Zwart, MSc.

Manuscript Region of Origin: NETHERLANDS

FutureWater

Science for Solutions

*Date:* *March 2006*
*Subject:* *Submission of research manuscript*

Dear Editor

With great pleasure we are submitting our research paper "Evaluating water use and productivity in the upper Bhima catchment, India, by integrating remote sensing and a process based hydrological model" for consideration for publication in Agricultural Water Management.

We believe that the integration of Remote Sensing in the calibration of hydrological models is innovative way to assess water use and crop water productivity in drought prone water scarce catchments with great further potential. We hope the demonstrated approach is of interest to the readers of agricultural water management and we are looking forward to your reaction.

Sincerely,

Walter Immerzeel

Costerweg 1G ● 6702 AA Wageningen ● Tel: 0317 460050
E-mail: w.immerzeel@futurewater.nl ● Website: www.futurewater.nl

# Evaluating water use and productivity in the upper Bhima catchment, India, by integrating remote sensing and a process based hydrological model

***W.W. Immerzeel[a*], A. Gaur[b], S.J. Zwart[c]***

*Submitted to Agricultural Water Management*

[a]FutureWater; Costerweg 1G; 6702 AA Wageningen; The Netherlands.

[b]International Water Management Institute; Patancheru, AP 502324 India.

[c]WaterWatch; Generaal Foulkesweg 28; 6703 BS Wageningen; The Netherlands.

[*] Corresponding author. Tel.: +31 317 460050
Email address: w.immerzeel@futurewater.nl (Walter Immerzeel)

**Abstract**

Water use and crop water productivity were assessed in the Upper Bhima catchment in southern India using an innovative integration of remotely sensed evapotranspiration (ET) and a process based hydrological model. The remote sensing based surface energy balance (SEBAL) algorithm was used to derive an eight month time series of actual evapotranspiration from October 2004 to May 2005 and used in the calibration of the soil and water assessment tool (SWAT). A total of 36 parameters were optimized using non-linear optimisation at the level of hydrological response unit (HRU). The final monthly average evapotranspiration residual was 1 mm, while the monthly standard error equalled 26 mm. The calibrated model was then used to derive a monthly basin water balance for the irrigation year 2004-2005 and to quantify water use. It is concluded that evapotranspiration is the largest water consumer in the catchment and total evaporative depletion was 38,172 million $m^3$ (835 mm). Of the total evaporative depletion 42% can be considered as non-beneficial and diversions to other water uses are to be considered. Simulated crop water productivities (CWP) for sugarcane, sorghum and winter wheat are relatively high at 2.9 $kg/m^3$, 1.3 $kg/m^3$ and 1.3 $kg/m^3$ respectively. The frequency distributions are characterised by low coefficient of variation, yielding limited scope for improvement in the agricultural areas under the current cropping systems. Further improvements in water productivity may however be achieved by transferring from sugarcane to a dual crop and introducing a fallow period from February to May and by converting idle rangelands to rain fed agricultural or bio fuel production area . The combined use of remote sensing and a distributed hydrological model have demonstrated the improved understanding of the entire water balance in a data scarce area.

*Key words: SWAT, SEBAL, calibration, water productivity, evapotranspiration*

## 1 Introduction

The Krishna River Basin (258,948 $km^2$) in semi-arid southern India is the fourth largest in India in terms of annual discharge, and the fifth in terms of surface area. The basin covers parts of three south-Indian states: Maharashtra (27%), Karnataka (44%), and Andhra Pradesh (29%). After independence (1947), a major national objective was the rapid harnessing of the countries water resources potential, which resulted in a surge of developments from 1960 onwards and a drastic reduction in river discharge. The massive proposed irrigation schemes promoted interstate water conflicts. The Krishna basin as a whole is now nearly a closed basin (Gaur *at al.*, 2007).

The Upper Bhima catchment is one of the twelve major catchments of the Krishna river basin and is located upstream in the state of Maharashtra. The catchment is relatively rich in water resources since a major part of the basin precipitation falls in the Western Ghat mountains in the west of the catchment. The catchment has an important role in the supply of water to downstream areas and it is an important catchment in the context of serving inter-sectoral water demands including urban, agriculture and drinking water supply. The water released to the main stem of the Krishna from the Upper Bhima catchment has however declined by 59% from an average of 8,816 $Mm^3$ in 1970-80 to 3,615 $Mm^3$ during 1994-2004, and is mainly concentrated in the monsoon months June to September (Government of Maharashtra, 2005).

During the last 20 years, a shift in agricultural practices towards more water consuming crops, such as sugarcane, took place. The sugarcane area, for example, has almost tripled during this period. An increased competition for water resources between agriculture and the industrial and domestic sectors may lead to a decrease in food production and to environmental degradation. The agricultural sector, being the largest consumer of water, should therefore focus on an increase of the productivity of water by obtaining more production per unit of water consumed, or by maintaining the same production at less water use (Kijne et al., 2003; Rijsberman, 2006). Better knowledge on fresh water depletion and crop production patterns throughout a basin is essential

for water managers and policy makers to improve water management in areas where water productivity is low. Traditional water management techniques often focus on saving water at field level by reducing irrigation water allocation to fields. However, a saving in one field may not necessarily lead to 'real' water savings at basin scale, as excess water can be reused downstream (Keller and Keller, 1995). Water management should therefore focus on a reduction of water depletion by evapotranspiration and increasing water productivity, as this water is not available for reuse. Water productivity in this study is defined as the marketable crop yield (Y) over the seasonal water use by actual evapotranspiration ($ET_{act}$).

Remote Sensing and distributed hydrological models are indispensable tools in objectively quantifying water depletion, water balance components, agricultural yields and water productivity in data scarce areas. This paper first shows how the hydrological model SWAT (Arnold et al., 1998; Srinivasan et al., 1998) can be calibrated using Remotely Sensed $ET_{act}$ based on the SEBAL algorithm (Bastiaanssen *et al.*, 1998, Bastiaanssen *et al.*, 2005) using a recently developed methodology (Immerzeel and Droogers, 2007). The calibrated model is then used to quantify the water balance of the catchment and water depletion per land use. Simulated crop yields are subsequently used to quantify the water productivity for each agricultural system and indicate scope for improvement. This approach is unique in the sense that Remote Sensing is completely integrated in the calibration of a hydrological model. Traditionally hydrological models are calibrated using measures hydrographs. Lack of data, equifinality issues, and absence of natural flows generally compromise the calibration of such models (Immerzeel and Droogers, 2007). The approach demonstrated in this paper provides an innovative methodology to assess water resources in data scarce and drought prone catchments.

## 2 Study area

The Upper Bhima catchment (45,678 km2) is located on the Bhima river, which is one of the main tributaries of Krishna river in the upstream part of the basin. It originates in the Western Ghat mountains and covers part of the Maharasthra state (Figure 1). The catchment is located between 16.5°-19.5° N and 73.0° -76.5° E and comprises of the catchment area of the river Bhima from its source to its confluence with the Sina River, which drains the north eastern part of the catchment. The elevation ranges from 414 meter in the east to 1458 meter in the Western Ghat mountains, while 95% of the catchment is below 800 meter and relatively flat.

The catchment has a highly diverse climate mainly caused by the interaction between the monsoon and the Western Ghat mountain range (Gunnel, 1997). The precipitation ranges from less than 500 mm in the eastern part of the basin to over 5000 mm in the mountains in the west with an average of 842 mm during the averagely wet irrigation year 2004-2005 (Figure 1). A total of 61% of the area receives less than 750 mm and 25% more than 1000 mm.

Figure 2 shows the monthly precipitation (P) and reference eveapotranspiration ($ET_{ref}$) in the basin. $ET_{ref}$ is calculated using Penman-Monteith (Monteith, 1969) with alfalfa as reference crop. The catchment has a high annual $ET_{ref}$ (1814 mm) ranging from 224 mm/month in May to 108 mm/month in December. Over 90% of the annual precipitation occurs during the monsoon months June to September. Between October and May large precipitation deficits occur with the peak in May (211mm) just before the onset of the monsoon.

The catchment is an important source of water for the entire Krishna basin since a major part of the precipitation falls in the Western Ghat range in the east of the catchment and is retained and released to downstream areas through an intricate set of reservoirs, especially along the Bhima tributary. The reservoirs accumulate water during the monsoon season (June to September), and this is gradually released throughout the irrigation season (October to May). Flows in the rivers

are therefore mainly human controlled and respond less directly to variations in the climate excitations and biophysical conditions.

Agriculture in the upper Bhima catchment is characterised by a diverse cropping pattern of sugarcane, sorghum, wheat, corn, millet, groundnut, grass fodder and a variety of horticultural crops (Neena, 1998). Three main types of agricultural systems can be identified in the catchment: (i) rain fed agriculture with a single crop (e.g. sorghum) cultivated during the monsoon, (ii) supplemental irrigated agriculture with one rain fed crop during the monsoon (e.g. sorghum) and a (groundwater) irrigated crop planted in October and harvested in February (e.g. winter wheat) and (iii) irrigated sugarcane. Sugarcane is grown throughout the year and irrigated from water released by the reservoir system. The normalized difference vegetation index (NDVI) patterns of these land use classes are shown in Figure 2. The natural NDVI peak was just after the monsoon early October and the NDVI of the irrigated agriculture classes remained relatively high also after the wet period. The sugarcane NDVI was still as high as 0.35 at the end of May. Other natural land covers in the catchment include rangelands, mixed forests, evergreen forests and water surfaces.

## 3 Methods

*Land use mapping*

A land use map was derived from remote sensing and was based on a 15 class unsupervised land use classification using a time series of 16 MODIS derived Normalized Difference Vegetation Index (NDVI) images with a spatial resolution of 250 meter from October 2004 to May 2005. The time series was similar to the SEBAL data set. Based on existing land use maps and field surveys the 15 classes were verified and clustered into the land use classes defined in Table 1.

*SWAT*

A SWAT model was built and simulations were run on a daily basis from June 2004 to May 2005. SWAT is a distributed hydrological model providing spatial coverage of the entire hydrological cycle including atmosphere, plants, unsaturated zone, groundwater and surface water. The model is comprehensively described in literature (Arnold *et al.*, 1998; Srinivasan *et al.*, 1998).

The catchment was subdivided into sub-basins and a river network based on a digital elevation model (DEM). Based on unique combinations of soil and land use the sub-basins were further detailed into hydrological response units (HRUs), which are the fundamental units of calculation. A total of 115 sub basins and 768 HRUs were delineated in the Upper Bhima catchment.

The Penman-Monteith method (Monteith, 1965) was used in SWAT to calculate daily reference evapotranspiration for alfalfa ($ET_{ref}$) and potential plant transpiration ($ET_p$). Daily data on radiation, wind speed, relative humidity, and air temperature for two different meteorological stations were used. Potential daily plant transpiration ($ET_p$) deviates from $ET_{ref}$, because actual daily crop height and leaf area index (LAI) are used to determine the aerodynamic resistances and canopy resistances respectively. Potential soil evaporation is an exponential function of $ET_{ref}$ and the soil cover and is further reduced during periods with high plant water use. Actual soil

evaporation is limited by the soil water content (θ) and is reduced exponentially when θ drops below field capacity.

To calculate actual plant transpiration the potential plant water uptake is defined by

$$w_{p,z} = \frac{ET_p}{\left[1 - e^{\beta_w}\right]} \cdot \left[1 - e^{\left(-\beta_w \cdot \frac{z}{z_{root}}\right)}\right] \quad (1.)$$

Where $w_{p,z}$ (mm $H_2O$) is the potential plant water uptake from the soil surface to a specified depth from the soil surface on a given day, $ET_p$ (mm $H_2O$) is the maximum plant transpiration on a given day taken from a lookup table, $\beta_w$ (-) is the water use distribution parameter, z is the depth from the soil surface (mm), and $z_{root}$ is the depth of root development in the soil (mm). Actual plant water uptake equals actual plant transpiration and similarly to soil evaporation, it reduces exponentially when θ drops below field capacity. Actual evapotranspiration ($ET_{act}$) is the sum of interception, actual soil evaporation and actual plant transpiration.

For each day of simulation, potential plant growth, i.e. plant growth under ideal growing conditions was calculated. Ideal growing conditions consist of adequate water and nutrient supply and a favourable climate as depicted in the $ET_p$. First the Absorbed Photosynthetical Radiation (APAR) was computed from intercepted solar radiation as a function of LAI, followed by a Light Use Efficiency (LUE) that is in SWAT essentially a function of carbon dioxide concentrations and vapor pressure deficits. Actual growth was calculated from optimal growth by inferring stress factors for extreme temperatures and water and nutrient deficiencies. The crop yield was computed as the harvestable fraction of the accumulated biomass production across the growing season.

Precipitation data in SWAT were parameterized on sub-basin level. For 52 municipalities monthly precipitation from June 2004 to May 2005 was available. The precipitation was attributed to the centre point of the municipality and spatially interpolated to monthly grids with a resolution of 250 meter. These grids were then used to determine monthly precipitation per sub-

basin, which was used as input in the SWAT model. Figure 1 shows the precipitation sum from June 2004 to May 2005.

The major reservoirs are mainly located along the Bhima branch. In the model the reservoirs were clustered into two reservoirs. The reservoirs inflow is largest during the monsoon season and throughout the remainder of the season the water is used for irrigation. The unused excess water is released using a monthly distribution derived from historical measurements.

The FAO digital soil map of the world (FAO, 1995) was used to derive soil properties for SWAT. Eight different soil units are identified in the catchment. The alluvial plains are predominantly characterized by vertisols and the Western Ghats and steeper slopes by luvisols.

*Evapotranspiration mapping*

The Surface Energy Balance Algorithm for Land (SEBAL) (Bastiaanssen et al., 1998; Bastiaanssen et al., 2005) was applied to spatially estimate total actual evapotranspiration ($ET_{act}$) between October 2004 and May 2005. During the monsoon period June to September cloudy conditions prevented the application of SEBAL. SEBAL uses satellite imagery from sensors measuring the visible, near-infrared and thermal radiation. The latent heat flux (LE) was computed on a pixel-by-pixel basis as a residual of the energy balance:

$$LE = R_n - G - H \quad (2.)$$

Where $R_n$ is the net radiation ($Wm^{-2}$), G is the soil heat flux ($Wm^{-2}$), and H is the sensible heat flux ($Wm^{-2}$). The net radiation ($R_n$) is the actual radiation that is available at the earth surface, which is equal to the sum of the net shortwave and longwave radiation. The former was computed as a function of the surface albedo, while the latter was computed from the difference between incoming and outgoing longwave radiation. Incoming longwave radiation was calculated using a modified Stefan-Boltzmann equation that uses an apparent emissivity, which is coupled to an atmospheric transmissivity and a measured air temperature. The outgoing longwave radiation was calculated using the Stefan-Boltzmann equation with a calculated surface emissivity and a surface

temperature measured by the satellite sensor. The soil heat flux (G) was estimated as a fraction from $R_n$, surface temperature and NDVI. The sensible heat flux (H) was estimated from surface temperature, surface roughness and measured windspeed. An essential step in the application of SEBAL is the solution of extreme values for H, prior to the pixel-by-pixel computations. In desert surroundings H is considered equal to $R_n$-G, while for water surfaces H is equal to 0.
SEBAL was applied on 16 cloud free satellite images with 1 kilometer resolution that were recorded by the Aqua sensor onboard the Moderate Resolution Imaging Spectrometer (MODIS). Initially SEBAL solved the instantaneous surface energy balance at the moment of overpass from the satellite sensor. ET sums for 2-week periods were obtained by re-applying the SEBAL models with average meteorological measurements for the 2-week periods and by assuming certain bio-physical parameters constant throughout the period. These parameters include surface albedo, NDVI, emissivity, evaporative fraction, surface roughness and bulk surface resistance.

*Calibration*

In this study PEST (PEST 2005 version) was used to calibrate the SWAT model using $ET_{act}$ acquired with SEBAL. PEST is a non-linear parameter estimation package that can be used to estimate parameters for simulation models (Doherty, 2005). The used calibration approach is described in detail by Immerzeel and Droogers (2007). PEST was setup at HRU level for all non-water surfaces for monthly $ET_{act}$ from October 2004 to May 2005. The objective function was based on 5344 measurements (668 non-open water HRUs * 8 months) and the following parameters were used in the calibration:

- Available water capacity (AWC). The AWC is defined as the difference between the field capacity of the soil and the permanent wilting point. It is defined per soil layer per soil type and determines, to a large extent, the water holding capacity of the soil. Ten

different soil types resulted in 10 different parameters to be optimized. AWC was bound by the range 0.05 mm/mm and 0.30 mm/mm.

- Groundwater revap coefficient (REVAP). Water may conceptually move from the shallow aquifer into the overlying unsaturated zone. The process of water being evaporated from the capillary fringe in dry periods is referred to as groundwater revap and in SWAT quantified by the revap coefficient (βr) multiplied by ETref. One βr for each land use, except water, was defined (6 parameters) and bound by the range 1.0-1.5.
- Maximum canopy storage (CAN). CAN determines for a large part the interception of precipitation. Actual interception is a function of actual Leaf Area Index (LAI) and maximum LAI, at which CAN is defined. One CAN was defined for each non-water land use resulting in 6 parameters bound by the range 0-10 mm for non-forested land uses and 0-20 mm for forests.
- Soil evaporation compensation factor (ESCO). ESCO determines to what soil depth evaporation of the soil is permissible to sustain evaporative demand. As the value for ESCO is reduced, the model is able to extract more of the evaporative demand from lower levels. For each non-water land use one ESCO parameter was optimised and bound by the range 0.01-1.00.
- Plant uptake compensation factor (EPCO). EPCO is similar to ESCO, but for plant water uptake. As EPCO approaches 1.0, the model allows more of the water uptake demand by plants to be met by lower layers in the soil. For each land use class one EPCO parameter was optimised and bound by the range 0.01-1.00.

This definition resulted in 34 parameters to be optimised.

*Water productivity analysis*

Based on the results of the calibrated SWAT model a water productivity analysis was performed for the agricultural land uses (RFA, SIA, ISUG). Crop water productivity (CWP) ($kg/m^3$) was based on SWAT output and defined as the simulated crop yield (kg/ha) divided by the simulated actual evapotranspiration ($m^3/ha$). The analysis was performed for each crop cycle within a land use class and the frequency distributions of CWPs were analyzed. Land use class SIA has a dual cropping pattern, while the other two only have a single crop. In total the analysis was therefore performed for four crops. The CWP analysis was validated with the SEBAL based water productivities. This could only be done for winter wheat, which grows from October 15 to February 10 (Table 1), because SEBAL could not be run during the monsoon due to clouds.

## 4 Results

*Land use mapping*

Figure 3 shows the land use map of the catchment and Table 1 shows the acreages of each land use class as well as the crop cycles within the agricultural land uses. In total 67% of the area is under agriculture, 5% is forested, 27% are non-productive rangelands and 1% is covered by open water. The forested areas are located in the western part of catchments where slopes are steep and rainfall is high. The irrigated sugarcane is mainly situated along the major irrigation canal systems along the Bhima River branch, while the supplemental irrigated agricultural is more abundant along the Sina River. Rain fed agricultural exhibits a more capricious spatial pattern. The rangelands are predominantly found in the south western part of the catchment.

*Calibration*

PEST optimises the sum of the squared residuals ($\Phi$) between observation (SEBAL $ET_{act}$) and simulations (SWAT $ET_{act}$). The calibration resulted in a reduction of $\Phi$ from $7.6 \cdot 10^6$ to $3.5 \cdot 10^6$. The final regression coefficient equalled 0.58. The SWAT calibration results are shown in Figure 4 and Table 2. Figure 4 shows the spatial patterns of the sum of $ET_{act}$ during the calibration period. The SWAT spatial patterns were generally in good agreement with the SEBAL results. There were however local differences and the SEBAL results show a larger within land use class variation, specifically the rangelands and irrigated sugarcane.

Table 2 provides more insight in the temporal results of the calibration per land use class. The calibration resulted in a considerable improvement. For all land uses, both the average monthly residual as well as the standard error, have decreased significantly. The decrease in average monthly residual between the base and calibrated model is largest for the evergreen forests in the Western Ghat Mountains (53 mm/month). The largest decrease in standard error is found for the

supplemental irrigated agriculture HRUs (12 mm/month). On a catchment scale the average residual is 1 mm/month and the standard error equals 26 mm/month.

*Water balance*

While remote sensing provides only information of the ET, the SWAT model is able to analyze all components of the water balance as well as biomass and crop growth processes. The monthly water balance was derived from the results of the calibrated model. Figure 5 shows the monthly water balance for the catchment. Balance closure refers to the net change in groundwater and soil storage. This storage generally decreased during the dry months and increased during the monsoon. Over the entire year there was 142 mm decrease in storage. Since the simulation year was averagely wet this could be explained by an underestimation of precipitation in the Western Ghats, an underestimation of irrigation from ground water, regional groundwater fluxes or water supplies from outside the catchment. The annual runoff coefficient (R/P) was 36% and only a slight evapotranspiration deficit was observed at catchment scale (17 mm). Between months there was considerable variation in all water balance components. The catchment was under water stress from November to May and nearly all $ET_{act}$ was supplied by irrigation water and storage decreases.

Discharge measurements indicate that a total of 2167 $Mm^3$ (47 mm) of water was released to the main stem of the Krishna River in the irrigation year 2004-2005. This is only 5.6% of the total precipitation and the water is released during the monsoon months only. There was no flow of water out of the catchment during the dry season. It is not possible to relate this to the simulated water balance, since there are no data on reservoir storage change available. However the dry year 2003-2004 depleted most reservoirs to dead storage levels and it is likely to assume that a considerable part of the runoff was used for increasing reservoir storage.

Volumetric cumulative annual precipitation was 38,912 $Mm^3$, while annual evaporative depletion equalled 38,172 $Mm^3$ and ET was by far the largest water consumer in the catchment, which is

nearly closed. Cumulative precipitation increased mainly during the monsoon month and ET was relatively constant throughout the year (Figure 6). High ET rates in the dry season were enabled by the spatial and temporal redistribution of water through the reservoir system, groundwater irrigation and depletion of soil and groundwater storage.

The distribution of evaporative depletion across different land uses is important in determining where possible savings or reallocation can be achieved (Figure 7). ET resulting in growth of agricultural crops during their growing season or growth of biomass of valuable ecosystems such as forests can be considered beneficial. ET from idle rangelands, from agricultural lands beyond the growing season and from reservoirs can be considered non-beneficial. It is interesting to conclude that a total of 42% of total evaporative depletion was non-beneficial and idle rangelands were the largest contributor (20%). There is thus scope for diversion of non beneficial ET to other more beneficial water uses. Of the beneficial ET, sugarcane depleted most in absolute terms ($10{,}205 \cdot 10^6$ $m^3$). Forests depleted a relative small amount, due to the limited area.

*Water productivity analysis*

To assess whether there is also scope for improvement within the agricultural land uses the distributions of CWP were analyzed (Table 3). Sugarcane had the highest CWP (2.9 kg/$m^3$). For winter wheat an average CWP of 1.3 kg/$m^3$ was found, which is rather high compared to the global mean of 1.1 kg/$m^3$ given by Zwart and Bastiaanssen (2004). A high CV and a strongly negatively skewed distribution generally indicate large potential for improvement (Zwart and Bastiaanssen, 2007). The largest CV in CWP is reported for WWHT (18.5%), whilst SGHY under RFA has a slightly negatively skewed distribution. It should be noted that it is likely to assume that in reality the variation in CWP will most likely be larger, because not all variation in climate, soil, and water and land management has been captured in the SWAT model. This is partly affirmed by comparing the SWAT WWHT CWPs to the SEBAL derived values. The average SEBAL WWHT CWP is 1.1 kg/$m^3$ and the CV is 4.6%, which are both smaller than the

SWAT based data. However the SEBAL CWP distribution is more negatively skewed. It should be noted though that the spatial basis for the distributions are different. The SEBAL distribution is based on the pixels in the MODIS imagery, while the SWAT distribution is based on HRUs. Sugarcane has a unique position in the Upper Bhima system. It is the largest consumer of water, but crop water productivity is high and its distribution very narrow (CV = 1.4%), leaving limited scope for further improvement. Water consumption is high (up to 1300 mm/year), because of the 12 month growing period; yields are however also extremely high (up to 37 ton/ha, harvest index = 0.22). The large sugarcane areas are all relatively flat and homogeneous and are generally not under water stress, since they are irrigated from the large reservoir based irrigation schemes. This is further clarified by Figure 8. Yields are shown as contours as a function of actual evaporative depletion and the sum of precipitation and irrigation. The figure shows that yields are nearly linearly related to ET, but indifferent to the annual sum of precipitation and irrigation. Only in the lower left corner of the figure water stress is a constraint to the yield. Once $ET_a$ is higher than 900 mm/year, $ET_a$ is not depending on precipitation or irrigation, but a function of other environmental variables (e.g. soil, nutrients, slope, pests and diseases).

## 5 Discussion and conclusions

Although the year 2004-2005 was averagely wet, an annual decrease of 142 mm in storage was calculated. It was not possible to isolate whether this storage change originated from reservoirs, groundwater or soil resources, or whether there are other sources of water left unaccounted for such as underestimated precipitation in the Western Ghat mountains, regional ground water fluxes, or water transfers from outside the catchment. A dynamic link with a regional groundwater model and the incorporation of reservoirs storage data could further detail the water balance and is recommendable. This would also enable accurate simulation of stream flow to the downstream areas.

The total simulated evaporative depletion and precipitation indicated that the upper Bhima catchment was nearly closed in 2004-2005. This was confirmed by independent discharge measurements, which show that only 5.6% of the total precipitation was released to the main stem of the Krishna River. If even a water supplying catchment, such as the Upper Bhima, is nearly closed the future for the entire Krishna basin looks grim and a structural rethinking of the planned expansion of irrigated agriculture is warranted. The water productivities are already relatively high and there seems limited scope for further improvement. Based on the analysis we conclude that there are however a number of ways to use or allocate water more effectively in the catchment. First of all a diversion from sugarcane to a dual cropping season (similar to SIA) and the introduction of a fallow period during the march-may period when precipitation is absent and $ET_{ref}$ is extremely high. Secondly a transition from the non-beneficial ET from rangelands to more beneficial water use. There are two possible ways to achieve this (i) In recent years there has been an increase in bio fuel production. A viable alternative could be the cultivation of jatropha curcas, which seeds are widely used in India for making biodiesel. The plant can be grown in wastelands and yields more than four times as much fuel as soybean and more than 10 times that of corn. One hectare of jatropha produces on average around 1900 liters of biofuel. (ii)

The transition of rangelands to rain fed agriculture (RFA). This would not require additional water; however there are other environmental constraints that are to be considered in assessing the suitability.

The integration of Remote Sensing in the calibration of a distributed hydrological model is highly innovative and enhances our insight in the hydrological pathways in data scarce and drought prone areas. Catchments, such as the Upper Bhima, are difficult to model given the large number anthropogenic disturbances (e.g. reservoirs, dams, irrigation canals) that render stream flow unusable for calibration. By using remotely sensed ET this problem is overcome and a detailed calibration of a hydrological model is enabled. The use of such a model has clear advantages over using remote sensing alone. A model provides insight in the entire hydrological cycle, fluxes between the different water balance components and the crop growth cycle, while remote sensing provides only insight in one component of the water balance at high spatial detail. A calibrated model also offers opportunities to analyse future scenarios, e.g. land use change and climate change. It is the combination of the strength of both approaches that provides a wealth of possible future applications.

## 6 Acknowledgements

This study was financially supported by the The National User Support Programme 2001-2005 (NUSP) is executed by the Netherlands Agency for Aerospace Programmes (NIVR) and the Space Research Organization of the Netherlands (SRON).

## 7 References


Arnold, J.G., Srinivasan, P., Muttiah, R.S., Williams, J.R., 1998. Large area hydrologic modeling and assessment. Part I. Model development. Journal of the American Water Resources Association 34, 73–89.

Bastiaanssen, W.G.M., Menenti, M., Feddes, R.A., Holtslag, A.A.M., 1998. The Surface Energy Balance Algorithm for Land (SEBAL): Part 1 formulation. Journal of Hydrology 212-213, 198-212.

Bastiaanssen, W.G.M., Noordman, E.J.M., Pelgrum, H., Davids, G., Allen, R.G., 2005. SEBAL for spatially distributed ET under actual management and growing conditions. J. Irr. Drain. Eng. 131, 85-93.

Doherty, J., 2005. PEST: Model Independent Parameter Estimation. Fifth edition of user manual. Watermark Numerical Computing, Brisbane.

FAO, 1995. FAO-Unesco digital Soil Map of the World and derived soil properties, 1:5.000.000. Unesco, Paris.

Gaur, A., McCornick, P.G., Turral, H., Acharya, S., 2007, Squeezed Dry: Implications of Drought and Water Regulation in the Krishna basin, India (submitted to Water Policy).

Government of Maharashtra, 2005. Report on water audit of irrigation projects in Maharashtra 2004-05. Water Resources Department, Mumbai.

Gunnel, Y., 1997. Relief and climate in South Asia: the influence of the Western Ghats on the current climate pattern of Peninsular India. International Journal of Climatology 17, 1169-1182.

Immerzeel, W.W., Droogers, P., 2007. Spatial calibration of a distributed hydrological model using Remote Sensing derived evapotranspiration in the Upper Bhima catchment, India. (submitted to Hydrological Processes).

Keller, A., Keller, J., 1995. Effective efficiency: a water use concept for allocating freshwater resources. Resources and Irrigation Division Discussion paper 22. Winrock International, Arlington.

Kijne, J.W., Barker, R., Molden, D., 2003. Water productivity in agriculture: limits and opportunities for improvement. CAB International, Wallingford.

Krishna Water Disputes Tribunal, 1976. Further report of the Krishna water disputes tribunal. Government of India, New Delhi.

Monteith, J.L., 1965. Evaporation and environment. Sym. Soc. Exp. Biol. 19, 205-234.

Neena, D., 1998. Inter-state variation in cropping pattern in India. Indian Journal of Regional Science 30, 57-69.

Rijsberman, F.R., 2006. Water scarcity: fact or fiction? Agric. Water Manage. 80, 5-22.

Srinivasan, R., Ramanarayanan, T.S., Arnold, J.G., Bednarz, S.T., 1998. Large area hydrologic modeling and assessment part II: model application. Journal of American Water Resource Association 34, 91–101.

Zwart, S.J., Bastiaanssen, W.G.M., 2004. Review of measured crop water productivity values for irrigated wheat, rice, cotton and maize. Agric. Water Manage. 69, 115-133.

Zwart, S.J., Bastiaanssen, W.G.M., 2007. SEBAL for detecting spatial variation of water productivity and scope for improvement in eight irrigated wheat systems. Agric. Water Manage. (in press).

## Tables

**Table 1: Acreages of different land uses in the catchment**

| Land use class | Crops | Growing season | Area ($10^3$ ha) | Area (% ) |
|---|---|---|---|---|
| Water surfaces (WATR) | - | - | 4111 | 1 |
| Rangelands (RNGE) | - | - | 122417 | 27 |
| Rain fed agriculture (RFA) | Sorghum (SGHY) | 10/6 - 30/9 | 153477 | 34 |
| Supplemental irrigated agriculture (SIA) | Sorghum (SGHY)<br>Winter wheat (WWHT) | 10/6 - 30/10<br>15/10 - 10/2 | 61208 | 13 |
| Irrigated sugarcane (ISUG) | Sugarcane (SUGC) | 1/6 - 31/5 | 90899 | 20 |
| Evergreen forest (FRSE) | - | - | 14160 | 3 |
| Mixed forest (FRST) | - | - | 10506 | 2 |

**Table 2: SWAT calibration results per land use and per month; μ denotes the average $\Delta ET_{act}$ and σ is the standard error, defined as the standard deviation of $\Delta ET_{act}$.**

| | | AGR1 | | AGR2 | | AGR3 | | FRSE | | FRST | | RNGE | | Catchment | |
|---|---|---|---|---|---|---|---|---|---|---|---|---|---|---|---|
| | | μ (mm) | σ (mm) | μ (mm) | σ (mm) | μ (mm) | σ (mm) | μ (mm) | σ (mm) | μ (mm) | σ (mm) | μ (mm) | σ (mm) | μ (mm) | σ (mm) |
| **Oct-04** | base | 27 | 23 | 1 | 30 | -33 | 19 | 1 | 25 | -7 | 29 | 17 | 21 | 5 | 32 |
| | calibrated | 1 | 22 | 0 | 30 | -15 | 21 | 10 | 24 | 5 | 30 | 12 | 19 | 0 | 25 |
| **Nov-04** | base | 21 | 18 | -55 | 19 | -13 | 33 | 58 | 45 | -2 | 38 | 4 | 18 | -6 | 37 |
| | calibrated | -1 | 18 | -20 | 18 | -2 | 21 | 10 | 25 | 5 | 32 | -7 | 17 | -6 | 21 |
| **Dec-04** | base | 43 | 14 | -19 | 17 | 34 | 20 | 80 | 35 | 42 | 35 | 28 | 17 | 25 | 30 |
| | calibrated | 26 | 13 | 12 | 12 | 30 | 15 | 41 | 22 | 33 | 26 | 19 | 15 | 23 | 16 |
| **Jan-05** | base | 38 | 17 | 37 | 15 | 38 | 15 | 66 | 22 | 27 | 23 | -32 | 22 | 22 | 35 |
| | calibrated | 17 | 16 | -4 | 13 | 31 | 13 | 17 | 20 | 10 | 19 | 1 | 15 | 11 | 20 |
| **Feb-05** | base | 28 | 22 | 25 | 22 | 31 | 21 | 68 | 21 | 26 | 18 | 0 | 27 | 22 | 27 |
| | calibrated | 7 | 21 | 13 | 22 | 22 | 20 | 16 | 20 | 8 | 18 | 3 | 18 | 11 | 21 |
| **Mar-05** | base | 15 | 22 | 11 | 24 | -27 | 29 | 54 | 19 | 14 | 12 | 9 | 20 | 5 | 29 |
| | calibrated | -12 | 19 | -4 | 23 | -16 | 25 | -15 | 19 | -11 | 12 | -8 | 19 | -10 | 22 |
| **Apr-05** | base | 23 | 23 | 20 | 25 | -7 | 32 | 50 | 22 | 11 | 15 | 20 | 21 | 16 | 28 |
| | calibrated | -9 | 21 | -2 | 24 | -22 | 29 | -30 | 22 | -19 | 15 | -2 | 21 | -9 | 25 |
| **May-05** | base | 24 | 28 | 26 | 34 | 1 | 39 | 78 | 24 | 28 | 19 | 15 | 28 | 19 | 34 |
| | calibrated | -13 | 28 | -1 | 32 | -9 | 35 | -13 | 24 | -6 | 19 | -8 | 28 | -8 | 31 |
| **Total** | base | 27 | 23 | 6 | 37 | 3 | 38 | 57 | 36 | 17 | 29 | 8 | 28 | 14 | 33 |
| | calibrated | 2 | 24 | -1 | 25 | 2 | 31 | 5 | 30 | 3 | 26 | 1 | 22 | 1 | 26 |

**Table 3: Statistical parameters of SWAT simulated water productivity per agricultural land use (RFA, SIA, ISUG) and per crop (sorghum (SGHY), winter wheat (WWHT), sugarcane (SUGC). The * suffix indicates results based on SEBAL.**

| | | RFA | SIA | | | ISUG |
|---|---|---|---|---|---|---|
| | | SGHY | SGHY | WWHT | WWHT* | SUGC |
| minimum | ($kg/m^3$) | 0.7 | 0.8 | 1.0 | 0.2 | 2.8 |
| maximum | ($kg/m^3$) | 1.6 | 1.8 | 2.1 | 1.3 | 3.0 |
| average | ($kg/m^3$) | 1.3 | 1.3 | 1.3 | 1.1 | 2.9 |
| standard deviation | ($kg/m^3$) | 0.1 | 0.2 | 0.2 | 0.1 | 0.0 |
| CV | (%) | 11.4 | 15.8 | 18.5 | 4.6 | 1.4 |
| Skewness | (-) | -1.2 | -0.3 | 1.1 | -5.1 | -0.1 |

**Figure Captions**

**Figure 1: Upper Bhima catchment boundary and contours of the precipitation sum from June 2004 to May 2005**

**Figure 2: Monthly precipitation (P) and reference evapotranspiration ($ET_{ref}$) and SPOT-VGT based average NDVI patterns for the agricultural land uses from June 2004 to May 2005**

**Figure 3: Land use based on unsupervised classification of MODIS time series of NDVI imagery**

**Figure 4: $ET_{act}$ sum (October 2004-May 2005) for SEBAL (left figure) and SWAT (right figure).**

**Figure 5: Monthly basin water balance; P = precipitation, I = Irrigation, ET = Evaporation, R = Runoff, B = Balance closure**

**Figure 6: Cumulative volumetric precipitation, actual evapotranspiration and from June 2004 to May 2005.**

**Figure 7: Evaporative depletion per land use for the year June 2004 – May 2005;**

**Figure 8: Yield (kg/ha) as a function of actual evapotranspiration (ET) and the sum of precipitation and irrigation (P+I) for ISUG – SUGC**

**Figure 1**

**Click here to download high resolution image**

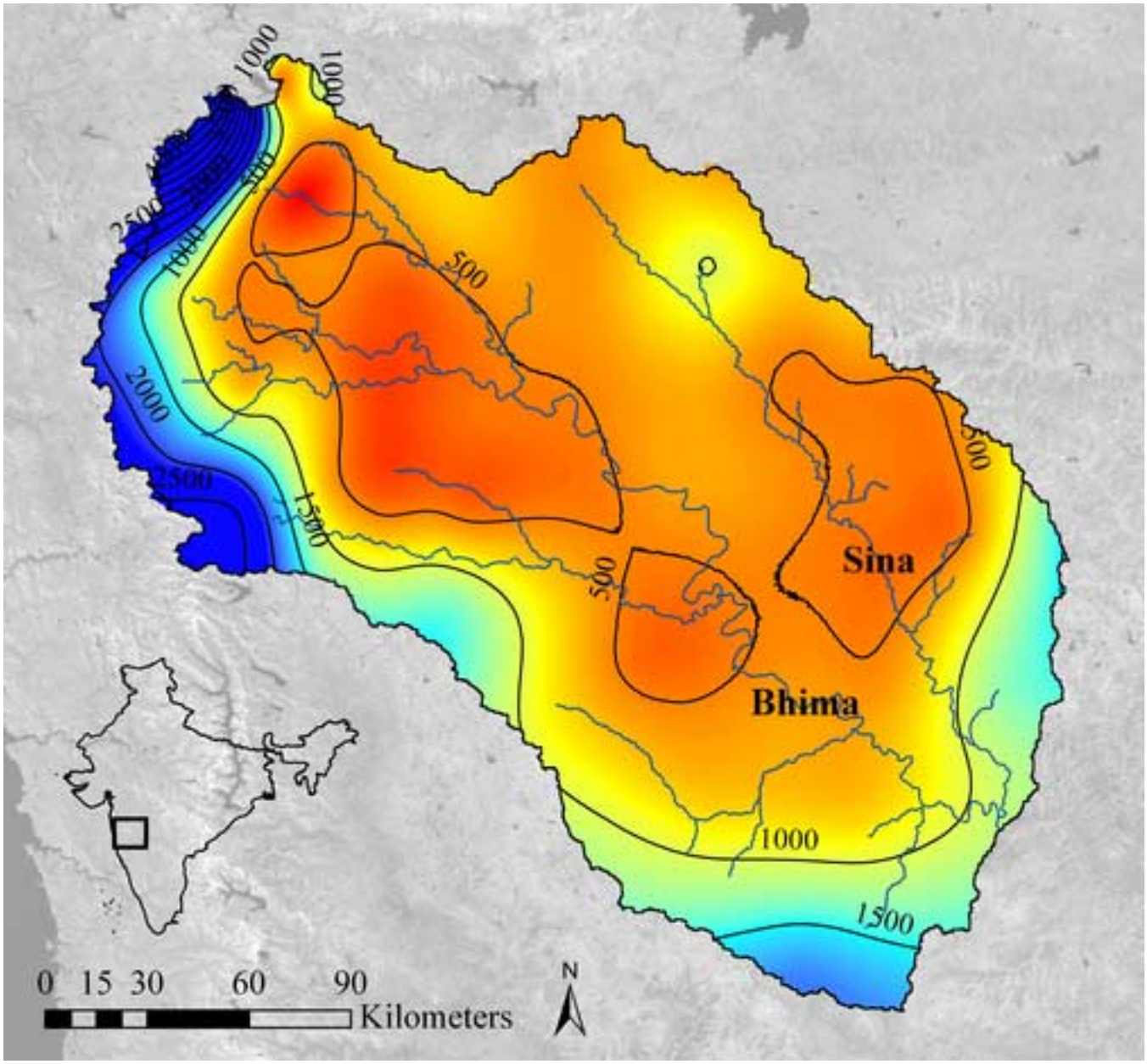

**Figure 2**

**Click here to download high resolution image**

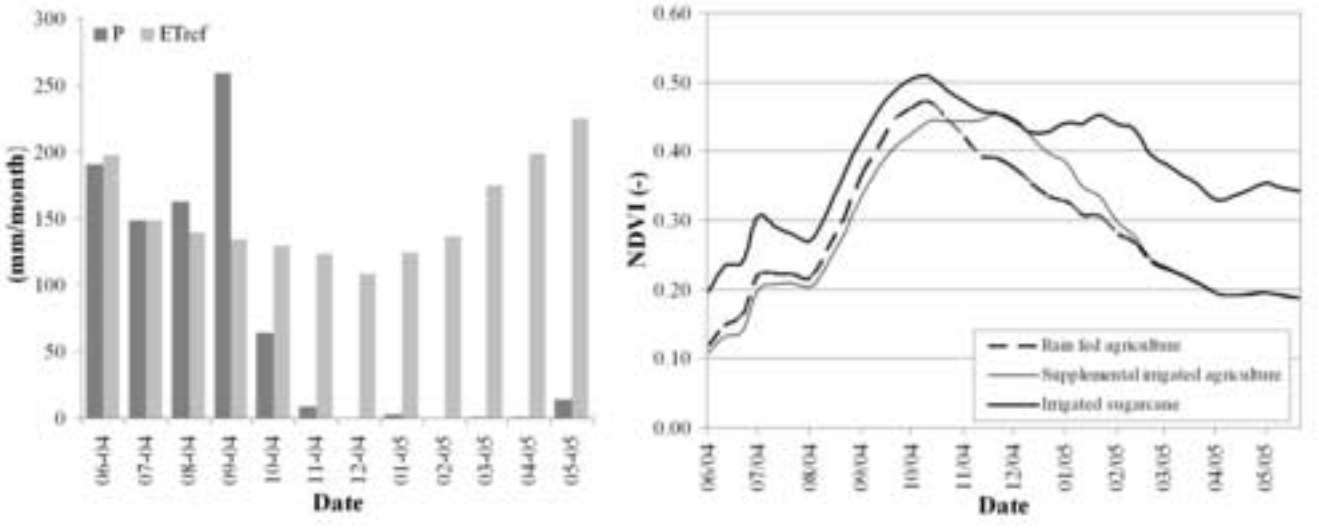

**Figure 3**

**Click here to download high resolution image**

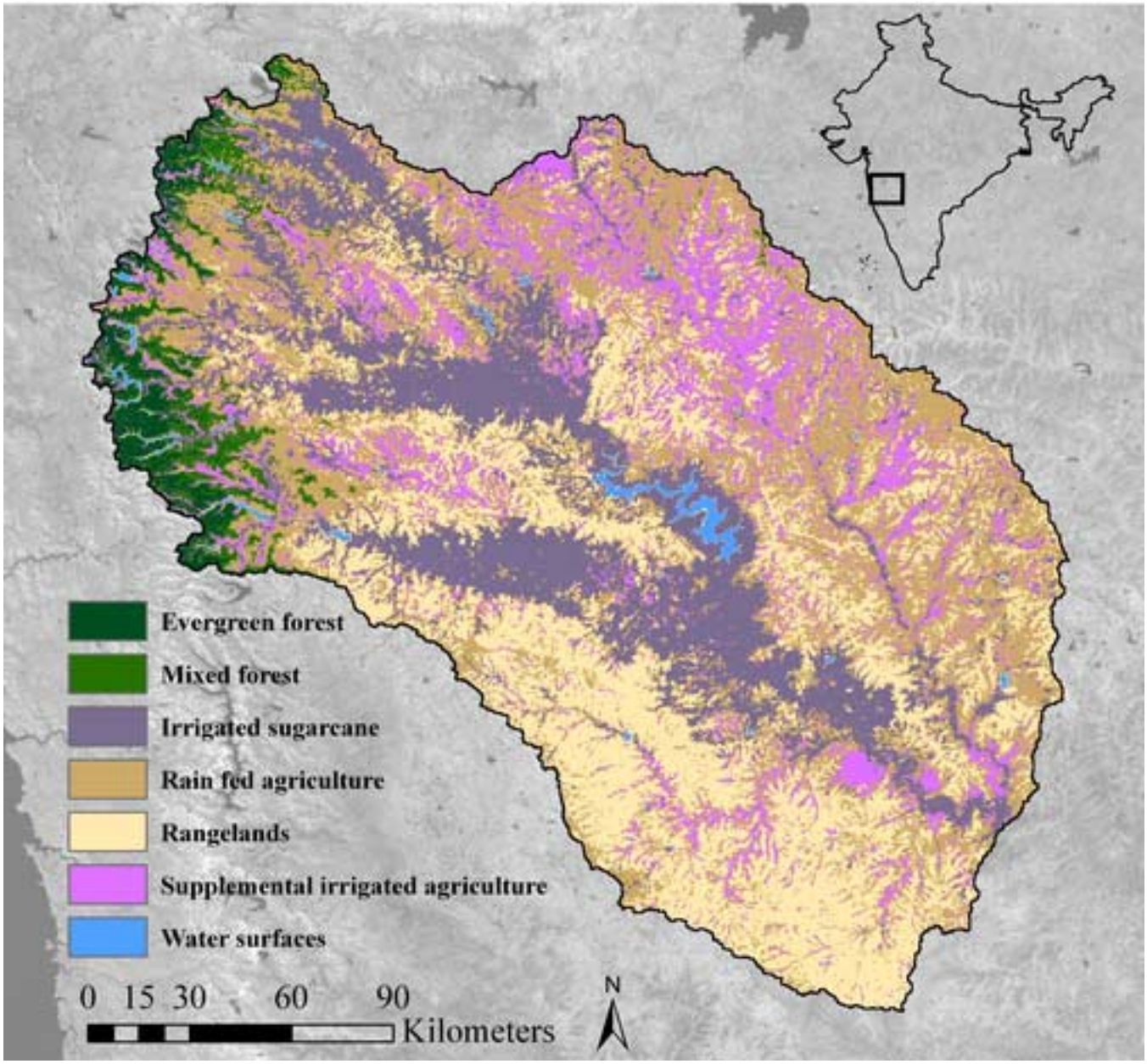

**Figure 4**

**Click here to download high resolution image**

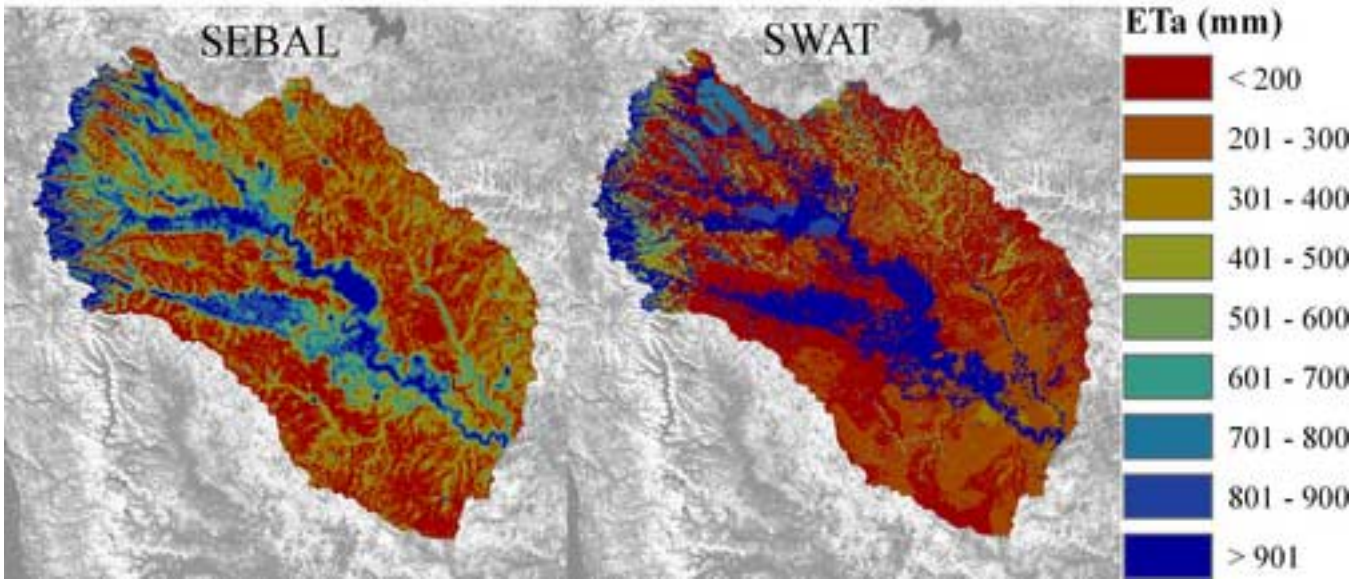

**Figure 5**

Click here to download high resolution image

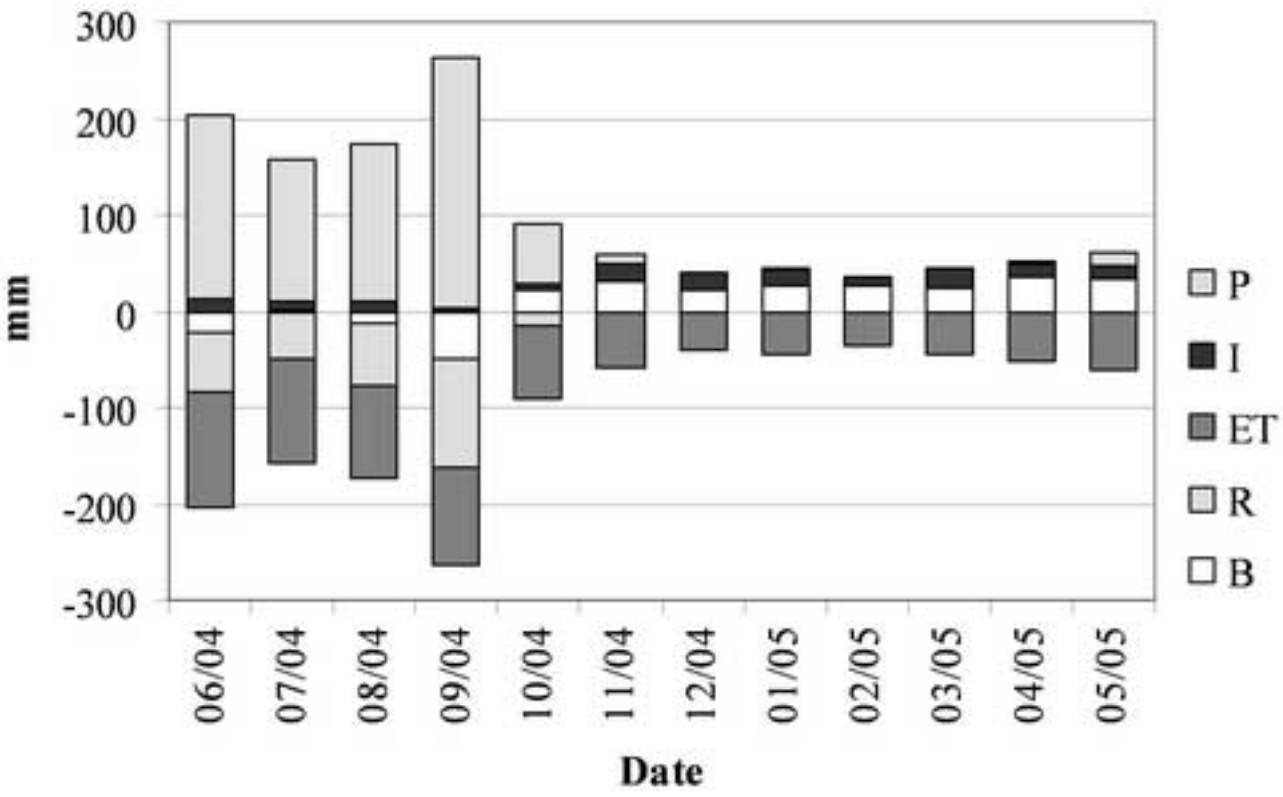

**Figure 6**

**Click here to download high resolution image**

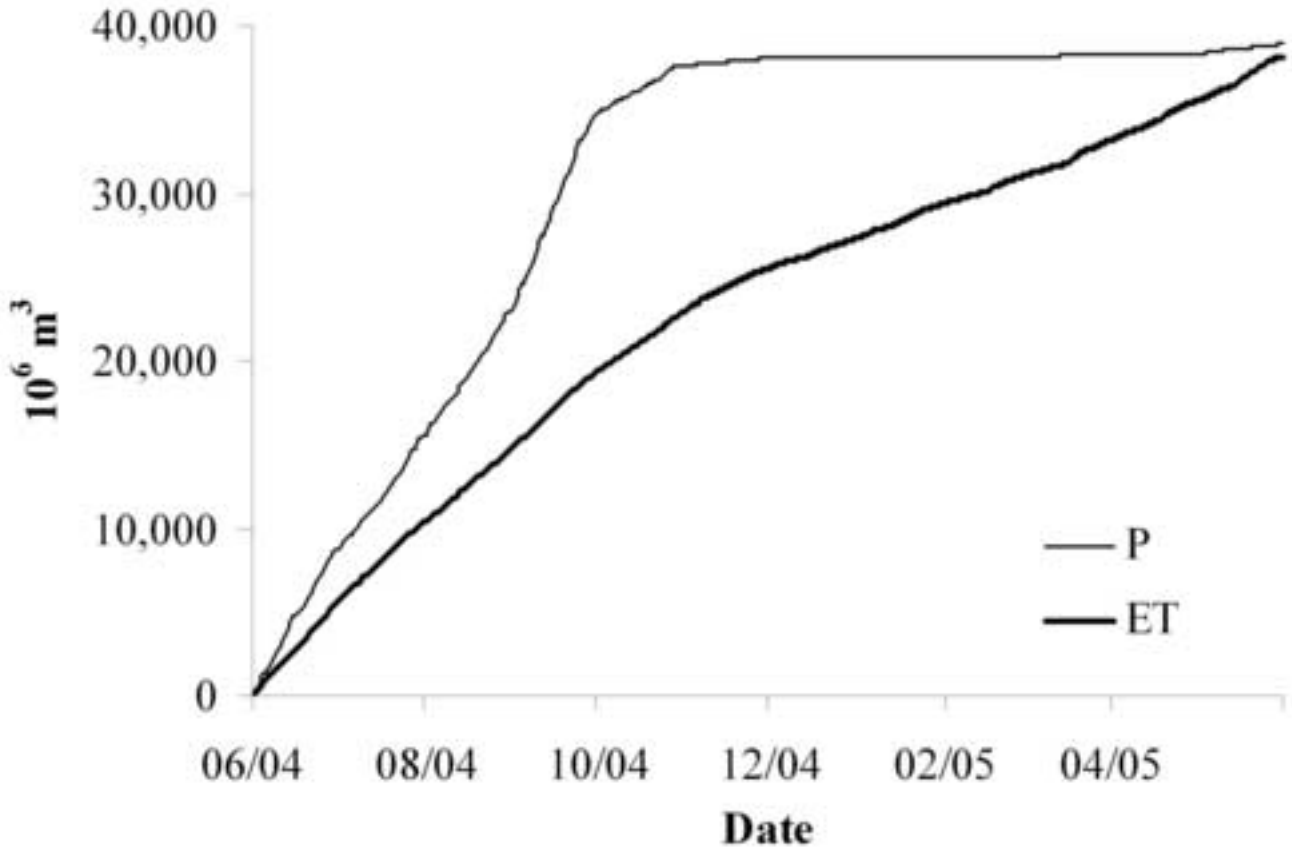

Figure 7
Click here to download high resolution image

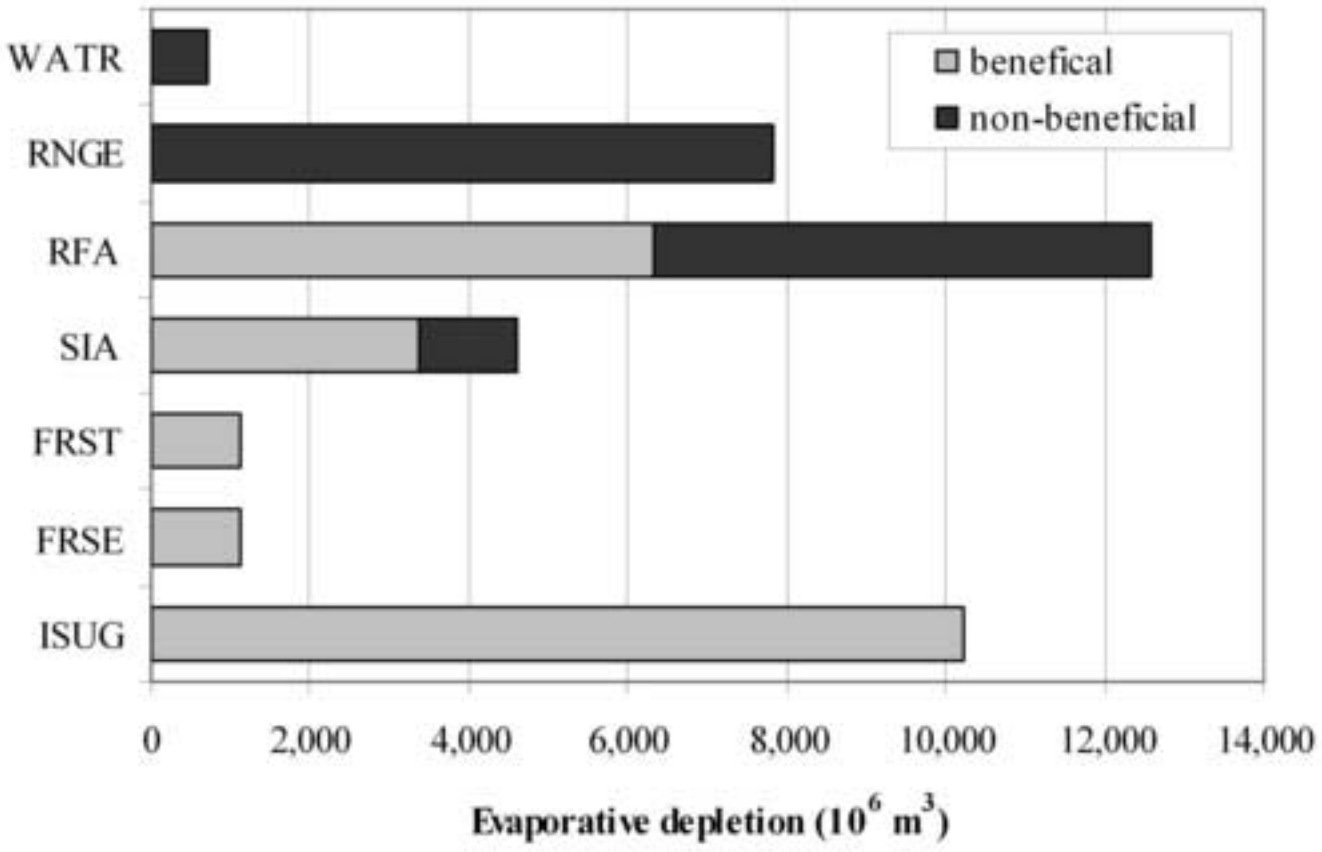

**Figure 8**

**Click here to download high resolution image**